

See discussions, stats, and author profiles for this publication at: <https://www.researchgate.net/publication/226870591>

Cosmic microwave background and first molecules in the early universe

Article in The European Physical Journal C · January 2009

DOI: 10.1140/epjc/s10052-008-0807-z

CITATIONS

7

READS

1,478

2 authors:



Monique Signore

Paris Observatory

111 PUBLICATIONS 707 CITATIONS

[SEE PROFILE](#)



Denis Puy

Université de Montpellier

64 PUBLICATIONS 509 CITATIONS

[SEE PROFILE](#)

Cosmic microwave background and first molecules in the early universe

Monique Signore^{1,a}, Denis Puy^{2,b}

¹Observatoire de Paris, LERMA, 75014 Paris, France

²University of Montpellier II, CNRS UMR 5024, GRAAL CC72, 34000 Montpellier, France

Received: 18 September 2008 / Published online: 12 December 2008

© Springer-Verlag / Società Italiana di Fisica 2008

Abstract Besides the Hubble expansion of the universe, the main evidence in favor of the big-bang theory was the discovery, by Penzias and Wilson, of the cosmic microwave background (hereafter CMB) radiation. In 1990, the COBE satellite (Cosmic Background Explorer) revealed an accurate black-body behavior with a temperature around 2.7 K. Although the microwave background is very smooth, the COBE satellite did detect small variations—at the level of one part in 100 000—in the temperature of the CMB from place to place in the sky. These ripples are caused by acoustic oscillations in the primordial plasma. While COBE was only sensitive to long-wavelength waves, the Wilkinson Microwave Anisotropy Probe (WMAP)—with its much higher resolution—reveals that the CMB temperature variations follow the distinctive pattern predicted by cosmological theory. Moreover, the existence of the microwave background allows cosmologists to deduce the conditions present in the early stages of the big bang and, in particular, helps to account for the chemistry of the universe. This report summarizes the latest measurements and studies of the CMB with the new calculations about the formation of primordial molecules. The PLANCK mission—planned to be launched in 2009—is also presented.

Contents

1 Elements of cosmology	118
1.1 Space-time geometry of cosmological models	120
1.2 Dynamics of cosmological models	120
1.3 Some Friedmann models	121
1.4 Inflation: a solution to the problems of the standard big-bang model	122

2 Decoupling particles in the early universe	124
2.1 Thermal equilibrium in the early universe	125
2.2 Thermal relics	127
3 Primordial nucleosynthesis	129
3.1 Standard big-bang nucleosynthesis	129
3.2 Observations of primordial abundances	132
3.3 On non-standard BBN models	135
3.4 Conclusions	135
4 The cosmic microwave background spectrum	135
4.1 On the thermal nature of the CMB spectrum	135
4.2 On observations of the CMB spectrum	137
4.3 Thermalization	139
4.4 Spectral distortions of CMB radiation	140
5 Cosmological recombination	141
5.1 Recombination of hydrogen and deuterium	141
5.2 Recombination of helium	142
5.3 Recombination of lithium	142
6 Standard chemistry	142
6.1 Helium chemistry	142
6.2 Hydrogen chemistry	143
6.3 Deuterium chemistry	143
6.4 Lithium chemistry	143
6.5 Equations of evolution	143
6.6 Results of thermochemistry	144
7 The CMB dipole anisotropy	148
7.1 The prediction of the dipole anisotropy	148
7.2 The observation of the dipole anisotropy	149
7.3 The physical origin of the dipole anisotropy	150
7.4 Conclusions	150
8 Cosmic microwave background anisotropies (CMBA)	151
8.1 CMB observables	151
8.2 Thomson scattering	152
8.3 Acoustic oscillations in the photon–baryon fluid	153
8.4 Polarization anisotropies	156
8.5 Secondary anisotropies	157

^a e-mail: monique.signore@obspm.fr

^b e-mail: denis.puy@graal.univ-montp2.fr

9	Cosmic microwave background anisotropies and primordial molecules	159
9.1	Imprint from primordial chemistry on CMB	159
9.2	On the primordial molecular clouds	161
9.3	Observational situation	162
10	Past and future observations: COBE, WMAP, PLANCK	162
10.1	The Cosmic Background Explorer COBE .	162
10.2	The balloon observations of millimetric extragalactic radiation and geophysics BOOMERANG	163
10.3	The Wilkinson Microwave Anisotropy Probe WMAP	165
10.4	The future: the PLANCK satellite	166
10.5	The HERSCHEL and ODIN satellite	167
11	Summary	168
	Acknowledgements	169
	References	169

1 Elements of cosmology

Modern cosmology began in the early years of the twentieth century: first, Einstein introduced the principle of relativity in 1905 against Newton's conception of space and time [1]; next his general theory of relativity supplanted Newton's law of universal gravitation [2]. The basic theoretical structure of modern cosmology consists of a family of mathematical models derived from Einstein's gravitational theory of relativity in the 1920s by Friedmann [3], Lemaître [4] and De Sitter [5]. Essentially, these models contain

- a description of space-time;
- a set of equations describing the action of gravity;
- a description of the bulk properties of matter.

The adoption of the “cosmological principle”—which supposes that, on large scales, the universe is homogeneous and isotropic—makes the description of space-time geometry and the form of the matter contents of the universe extremely simple. Here, let us only note that “isotropy” means that the universe looks the same in all directions and “homogeneity” means that the universe looks the same at every point.

While theoretical physicists, from Einstein's theory, started to develop the model which is nowadays called the “big-bang” model, the major steps toward the modern era were taken by observational astronomers. Hubble, as early as 1929, published his observations leading to recognition of the expansion of the universe [6]. Later, in 1965, Penzias and Wilson [7] providing a safe calibration of Bell Labs receiver and after eliminating sources of possible systematic errors, found an excess noise power equivalent to thermal radiation with a temperature of a few kelvin: this was the discovery of

the CMB radiation. Its existence is strong evidence for the big-bang theory, which states that the early universe was a hot plasma of elementary particles governed by a Planckian distribution with just the temperature as a simple parameter.

First, let us emphasize that, in cosmology, quantum phenomena control the small scales of structures; gravity dominates the large scales of the structures. But let us briefly present the sequence of events that make up cosmic history in the framework of the “standard model”. In the following description of the evolution of the universe, the time t refers to the total elapsed time or age of the universe, and the temperature T refers to the temperature of the radiation or often to the typical particle energy. Let us note only that there is a relation between t and T , given later in the review. Anyway, as time progresses, the universe expands and the temperature decreases. The following survey anticipates some of the explanations that we shall discuss throughout the review. A summary appears in Table 1.1.

- *The Planck epoch* ($t < 10^{-43}$ s, $T \sim 10^{19}$ GeV).

This epoch can be thought of as the beginning of time.

- *The inflationary epoch* ($t < 10^{-32}$ s, $T \sim 10^{16}$ GeV).

The physical vacuum dominates the energy, developing a repulsive field that drives the universe to enormous size. Inflation may be responsible for the “fluctuations” that led to the formation of structure. If so, one might find relics of this epoch in the fluctuations of the CMB and primordial gravitational waves.

- *The creation of radiation epoch* ($t \sim 10^{-26}$ s, $T \sim 10^{14}$ GeV).

The vacuum energy transforms itself into photons as well as particles and antiparticles of matter in equal numbers. This epoch is also called “reheating”, the conversion of energy into thermal radiation. The background radiation energy we see filling the universe today originates here. It is possible that cosmic dark matter is also produced during this epoch.

- *The creation of baryonic matter epoch* (just before the electroweak transition, $T \sim 100$ GeV).

A small excess of quarks and electrons over antiquarks and positrons is generated in a process called baryogenesis. This process leaves its imprint with the presence of baryonic matter today.

- *The electroweak epoch* ($t \sim 10^{-10}$ s, $T \sim 100$ GeV).

This epoch represents the threshold of currently laboratory-tested physics. There may be cosmic relics of this epoch such as dark matter or cosmic defects.

- *The quark–hadron transition epoch* ($t \sim 10^{-4}$ s, $T \sim 200$ MeV).

The universe is supposed to make a transition from *quark soup* to hadronic matter. This transition may have left relics in the present universe such as various forms of dark matter: axions, black holes etc. This transition may have also left the matter in a clumpy state that would affect the creation of light nuclei later on.

Table 1.1 Orders of magnitude of important epochs in the history of the universe, according to the Λ CDM model

Epoch	Time	Temperature	Redshift	Physics
Planck epoch	10^{-43} s	10^{19} GeV	10^{32}	limit of spacetime
Cosmic inflation	10^{-32} s	10^{16} GeV	10^{29}	unstable vacuum
Creation of light	10^{-26} s	10^{14} GeV	10^{27}	conversion of vacuum to radiation energy
Electroweak epoch	10^{-10} s	100 GeV	10^{15}	electroweak unification
The strong epoch	10^{-4} s	200 MeV	2×10^{12}	quark–hadron transition
Weak decoupling	1 s	1 MeV	10^{12}	neutrinos decouple
$e^+ - e^-$ annihilation	5 s	0.5 MeV	5×10^9	electron heat dumped into photons
Nucleosynthesis	100 s	100 keV	10^9	nuclei formation
Spectral decoupling	1 month	500 eV	10^6	end of efficient photon production
Matter/radiation equality	10 000 years	10 000 K	3 300	matter dominates mass density
Last scattering epoch	0.3 My	3 000 K	1 000	universe transparent to light
Molecular epoch	15 My	1 500 K	500	formation of molecules
Dark ages	1 Gy	20 K	65	first small objects coalesce
Bright ages	2–13 Gy	3–10 K	10–30	large-scale gravitational instability
Present epoch	13 Gy	2.725 K	0	new astrophysics and physics

- *The decoupling of the weak interactions* ($t \sim 1$ s, $T \sim 1$ MeV).

It follows that the neutron-to-proton ratio is fixed and that the present universe is dominated by hydrogen. The cosmic neutrinos decoupled—as well as several other possible forms of dark matter—and have their density fixed at this time.

- *The epoch of creation of light elements* ($t \sim 100$ s, $T \sim 100$ keV).

The present abundances of helium, deuterium and lithium can provide a precise test of our understanding of this epoch.

- *The spectral decoupling epoch* ($t \sim 1$ month, $T \sim 500$ eV).

This epoch starts with the end of the efficiency of photon production. It results in the final conversion of primordial energy into the black-body spectrum of the CMB.

- *The radiation–matter transition*. The transition from the domination of radiation to that of matter appeared at about $t \sim 10 000$ years, $T \sim 30 000$ K or 3 eV.

- *Last scattering* ($t \sim 300 000$ years, $T \sim 3 000$ K).

The radiation cools enough for electrons to attach to protons—the hydrogen recombination—and the electrons almost stop interacting with the radiation. The universe becomes transparent to light. The baryonic matter decoupled from the radiation.

- At $T \sim 3 000$ K, when helium, the first neutral atom, appeared followed by those from hydrogen, deuterium and lithium, chemistry acts up and leads to the formation of the first molecules such as HeH^+ , H_2 , HD and LiH.

In this work—and this is an original point of view—we focus on events that take place near $T \sim 3 000$ K and which lead to CMB fluctuations and primordial chemistry as relics and observables.

This review summarizes the present knowledge of the CMB radiation, and some of the details of the generation of its possible distortions and anisotropies. The existence of other fossils—such as light nuclei—is also discussed with particular attention to the arrival of the first molecules in the universe. Earlier general reviews on CMB can be found in [8–10], and on primordial chemistry in [11].

Since the discovery of the CMB [7], measurements of CMB made in the last years have moved cosmology into a new era of precise parameter determination and the ability to probe the conditions during the early universe. The most important features were strongly indicated by the data from COBE [12], WMAP [13, 14] and many ongoing ground-based and balloon-borne observing campaigns.

Let us only note that the PLANCK satellite [15]—due to be launched in 2009—will be the first mission to map the entire CMB sky with mJy sensitivity and an angular resolution better than $10'$. Past, present and future observations of the CMB radiations are summarized at the end of this article. This article is organized as follows.

- In the remainder of Sect. 1, a brief summary of the basics of the standard cosmological models is given. More details can be found in several excellent textbooks or reviews [16–18, 28, 29].
- Section 2 focuses on the various decouplings of particles in the early universe.
- Section 3 summarizes studies of the primordial nucleosynthesis and confronts the predicted primordial abundances to the observed primordial abundances.
- Section 4 reviews thermalization and processes which may generate spectral distortions of the CMB radiation.
- Section 5 describes the cosmological recombination.

- Section 6 studies primordial chemistry.
- Section 7 recalls the discovery, the main measurements of the CMB dipole and the resulting estimates of the velocity of the solar system.
- Section 8 presents the power spectrum of CMB fluctuations: temperature and polarization anisotropies.
- Section 9 discusses some of the details of the influence of primordial chemistry on CMB anisotropies (hereafter CMBA).
- In Section 10, the main results obtained by NASA satellites: COBE (Cosmic Background Explorer), WMAP (Wilkinson Microwave Anisotropy Probe) as well as the expected investigations from the future ESA PLANCK spacecraft are given.
- Section 11 gives a summary.

1.1 Space-time geometry of cosmological models

Einstein's theory involves the use of a metric tensor $g_{\mu\nu}$ that relates four-dimensional space-time intervals to a set of coordinates. Our metric signature is (+−−−). The “cosmological principle”—which supposes that, on large scales, the universe is homogeneous and isotropic—imposes a strict symmetry on the universe and therefore a preferred time coordinate. Cosmological space-times must have the same local geometry at each point on a surface of constant time. The space-time may be expanding or contracting and different time slices differing by a scale factor $a(t)$. Then one can show that the most general space-time metric is the Robertson–Walker metric:

$$ds^2 = c^2 dt^2 - a(t)^2 \left[\frac{dr^2}{1 - kr^2} + r^2(d\theta^2 + \sin^2\theta d\phi^2) \right], \quad (1.1)$$

where t is the time coordinate, c is the speed of light, (r, θ, ϕ) are spherical polar coordinates for the spatial part of the metric and the scale factor $a(t)$ is defined so that physical lengths scale proportional to a ; k is the curvature parameter with three options: $k = 0$ represents a flat universe with a Euclidean geometry on each surface of constant time; $k > 0$ signifies a closed universe, with positively curved spatial surfaces like three-dimensional versions of the surface of a sphere; $k < 0$ indicates negatively curved space sections of hyperbolic form.

From the Robertson–Walker metric, the global expansion of the spatial slices can be seen, as a function of the cosmic time, through the Hubble parameter:

$$H(t) = \frac{\dot{a}(t)}{a(t)}, \quad (1.2)$$

where the dot means the time derivative. This model accounts naturally for Hubble's law which relates the apparent

recession velocity v of a galaxy at a distance d :

$$v(t) = H_0 d, \quad (1.3)$$

where the zero subscript refers to the present day and H_0 , the so-called Hubble constant, is the Hubble parameter $H(t)$, evaluated at the present epoch t_0 .

Let us note that the Hubble constant is usually quoted as

$$H_0 = 100 \text{ h km s}^{-1} \text{ Mpc}^{-1}. \quad (1.4)$$

Present observations suggest $h \sim 0.7$ [34, 35].

From the scale factor, we can define the redshift z of a source which emitted its radiation at any time:

$$\frac{\lambda_0}{\lambda} = 1 + z = \frac{a_0}{a}. \quad (1.5)$$

The observed wavelength λ_0 and the emitted wavelength λ are in the same ratio as the scale factor of the universe at the moment of observation a_0 and the moment of emission a . Let us only emphasize that this *effect* arises as a consequence of the light having traveled along a path through the expanding space-time.

Indeed, this wavelength shift (usually called “redshift”, because the wavelengths are shifted towards large values) is not a Doppler shift. It is due to the expansion of space that stretches all wavelengths.

1.2 Dynamics of cosmological models

Einstein's field equations can be written in the following form:

$$G_{\mu\nu} = \frac{8\pi G}{c^4} T_{\mu\nu}, \quad (1.6)$$

where the constant G is the gravitational constant of Newton; $G_{\mu\nu}$ is the Einstein tensor, which describes the action of gravity through the curvature of space-time, $T_{\mu\nu}$ is the energy-momentum tensor, which describes the bulk properties of matter. For simplicity, and because it is consistent with the cosmological principle, it is often useful to adopt the perfect fluid form for the energy tensor of cosmological matter which can be written

$$T_{\mu\nu} = \left(\rho + \frac{p}{c^2} \right) u_\mu u_\nu - \frac{p}{c^2} g_{\mu\nu}, \quad (1.7)$$

where u_μ is the four-velocity of the fluid, ρc^2 is the energy density in the rest frame of the fluid and p is the isotropic pressure in that frame. Then the Einstein equations (1.6) simplify to the so-called Friedmann equation:

$$3 \left(\frac{\dot{a}}{a} \right)^2 = 8\pi G\rho - \frac{3kc^2}{a^2} + \Lambda c^2, \quad (1.8)$$

to the *acceleration equation*:

$$\frac{\ddot{a}}{a} = -\frac{4\pi G\rho}{3}\left(\rho + 3\frac{p}{c^2}\right) + \frac{\Lambda c^2}{3}, \quad (1.9)$$

and to energy conservation:

$$\dot{\rho} = -3\frac{\dot{a}}{a}\left(\rho + \frac{p}{c^2}\right), \quad (1.10)$$

where Λ is called the *cosmological constant* and where the dots denote derivatives with respect to cosmic time t . These equations—which are not independent—determine the time evolution of the cosmic scale factor $a(t)$ describing the expansion or the contraction of the universe. We may note that the energy-momentum tensor $T_{\mu\nu}$ is covariantly conserved,

$$\Delta_\mu T^{\mu\nu} = 0, \quad (1.11)$$

and yields (1.10), which can be also written

$$\dot{\rho} = -3H\left(\rho + \frac{p}{c^2}\right). \quad (1.12)$$

To solve the system of equations (1.8), (1.9) and (1.10), we need to specify the equation of state, which characterizes the material contents of the universe.

Within the fluid approximation used here, we may assume that the pressure p is a single-valued function of the energy density: $p = p(\rho)$; one may define the equation-of-state parameter, ω , by

$$p = \omega\rho c^2. \quad (1.13)$$

If the universe is filled with non-relativistic matter (or cold matter), it can be described by the *dust* equation of state, with $p = 0$ and $\omega = 0$. If the universe is filled with relativistic matter (a photon gas, for instance), the equation of state of this radiation is of the form $p = \rho c^2/3$ and $\omega = 1/3$.

In the standard big-bang theory, the early universe is radiation dominated ($\omega = 1/3$); as it expands and cools, the matter becomes non-relativistic and the equation of state changes smoothly to that of dust ($\omega = 0$). For the equation of state (1.13), with a constant value of ω , (1.12) gives

$$\rho = \kappa a^{-3(1+\omega)}, \quad (1.14)$$

where κ is a constant and with the corresponding relation for energy conservation (1.12) given by

$$\dot{\rho} = -3(1+\omega)H\rho. \quad (1.15)$$

Thus, for a radiation-dominated universe (which was the case for the first several thousand years after the big bang),

$$\rho \propto a^{-4} \quad (\text{radiation domination}), \quad (1.16)$$

and for a matter-dominated universe

$$\rho \propto a^{-3} \quad (\text{matter domination}). \quad (1.17)$$

From the Friedmann equation (see (1.8)), we may define, at any time, the critical energy density

$$\rho_c = \frac{3H^2}{8\pi G}, \quad (1.18)$$

for which the spatial sections must be precisely flat ($k = 0$). Let us note that the critical density ρ_c is defined in terms of the expansion rate. In particular, its value today is given through the Hubble constant:

$$\rho_{c0} = \rho_c(z=0) = \frac{3H_0^2}{8\pi G} = 1.8788 \times 10^{-29} h^2 \text{ g cm}^{-3}. \quad (1.19)$$

We then define the density parameter by

$$\Omega = \frac{\rho}{\rho_c}. \quad (1.20)$$

Therefore the energy density of the universe is related to its local geometry:

- for $\Omega > 1$, $k > 0$, the universe is spatially closed,
- for $\Omega < 1$, $k < 0$, the universe is spatially open.

Other reduced quantities may also be used:

$$\Omega_k = -\frac{kc^2}{H^2 a^2} \quad \text{the curvature parameter}, \quad (1.21)$$

$$\Omega_\Lambda = \frac{\Lambda c^2}{3H^2} \quad \text{the cosmological constant parameter}. \quad (1.22)$$

Then the Friedmann (1.8) can be written

$$\Omega + \Omega_k + \Omega_\Lambda = 1. \quad (1.23)$$

Present-day densities in any given particle species X are quoted in units of the critical density, thus:

$$\rho_X(a_0) = \rho_{X0} = (\Omega_X \rho_c)_{a=a_0}. \quad (1.24)$$

Moreover, besides the Hubble parameter given by the relation (1.2), one may also introduce the deceleration parameter,

$$q = -\frac{\ddot{a}}{a}. \quad (1.25)$$

1.3 Some Friedmann models

Here, we do not want to discuss all the possible solutions of the Friedmann equations with a view to obtaining and

classifying all universes that are homogeneous and isotropic. Let us only note that in *modern cosmology*, it is customary to specify three *observable* parameters, namely, the Hubble parameter H , the density parameter Ω and the deceleration parameter q . Usually, these *observable* parameters are estimated today and referred to by H_0 , Ω_0 and q_0 ; in principle, they can be determined by observation. Moreover, only *dust* universes ($p = 0$ or $\omega = 0$) are considered. In this section, Sect. 1.3, we shall adopt for these particular models, instead of $a = a(t)$, the scale factor $R = R(t)$.

In general, the following cases are considered:

- static models (those which have $\dot{R} = 0$);
- empty models (with $\rho = 0$);
- the three non-empty models (with $\Lambda = 0$);
- the non-empty models (with $\Lambda \neq 0$).

Here, we shall only and briefly focus on the two last generic cases.

1.3.1 On the three non-empty models with $\Lambda = 0$

For many cosmologists and for many years, the three following models were the only models ever considered seriously:

- when the density is above the critical density:

$$\rho > \rho_c, \quad (1.26)$$

the function $R(t)$ grows from zero to a maximum value, then a collapse phase follows to zero;

- when the density is equal to the critical density, $R(t)$ is simply given by

$$R(t) = R_0(3/2H_0t)^{2/3} = R_0(t/t_0)^{2/3} \quad \text{with} \quad t_0 = 2/3H_0^{-1} = 1/\sqrt{6\pi G\rho_c}; \quad (1.27)$$

- when the density is below the critical density, the function $R(t)$ grows from zero to infinity (it is easy to check from the Friedman equations that the function $R(t)$ is proportional to t when R is large);

similarly the behavior of $R(t)$ can be found when $t \rightarrow 0$ independently of the model:

$$R(t) \sim t^{2/3}. \quad (1.28)$$

1.3.2 On the non-empty models with $\Lambda \neq 0$

To specify a cosmological model, it is customary to determine with precision two *observables*: Ω_0 and q_0 for instance. The modern cosmological view of the Friedman models is summarized in Fig. 1.1. One must note that a strong motivation for the existence of a non-zero cosmological constant comes from observations.

- Recent results from the CMBA observations (Boomerang [30], Archeops [31], WMAP [32]) show that the universe is nearly flat. Once combined with HST (Hubble Space Telescope) measurements, these results require a non-zero cosmological constant [33].
- In 1998, two independent groups—the Supernova Cosmology Project (SCP) [34] and the High-z Supernova Search (HzS) [35]—announced a spectacular result based on observations of distant type-Ia supernovae: the expansion of the universe is accelerating! Taking into account these CMBA and SNIa results and their conclusions allow us to put the sign “We are here” on Fig. 1.1.

Let us recall that the classic discussion of the physics of the cosmological constant can be found in Weinberg [36, 37]—more recent views are presented, for instance, by Straumann [38], Carroll [39], Weinberg [40].

Let us also remark that we have introduced the equation of state (1.13): $p = \omega\rho c^2$, with $\omega = 1/3$ for radiation, $\omega = 0$ for cold matter. If one considers the vacuum energy density ρ_v (or the cosmological constant Λ) such that

$$p_v = -\rho_v c^2 = -\frac{\Lambda c^2}{8\pi G}, \quad (1.29)$$

then $\omega_v = -1$.

Most cosmologists consider also for *dark energy* quintessence, a time-evolving, spatially inhomogeneous energy component. The equation of state, for quintessence, is a function of redshift: $\omega = \omega(z)$. Now, whether the dark energy is really constant as in Einstein’s original version or whether it is in the form of quintessence, the question may be answered by observational plans such as the spatial mission SNAP (SuperNova Acceleration Probe); the question whether the dark energy can be understood within a fundamental theory may be *only* answered from a particle-physics viewpoint.

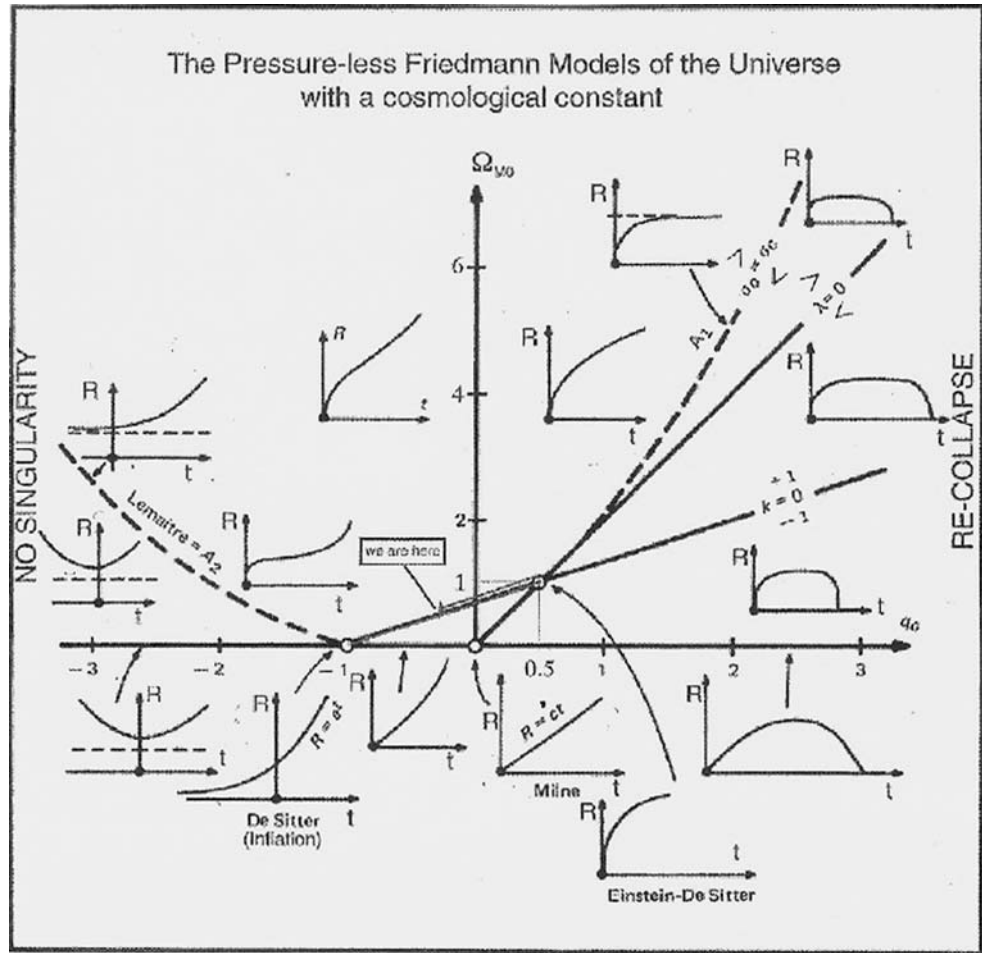
1.4 Inflation: a solution to the problems of the standard big-bang model

Although the Friedman model described above seems to give a successful description of the universe, there are some fundamental problems about the initial conditions required. Three of these problems are: the “horizon problem”, the “flatness problem” and the “monopole problem”.

- *The horizon problem.*

The universe is uniform and isotropic on large scales. In particular, if one observes the cosmic microwave background in two regions in the sky located in directions that are widely different and which could never have been in thermal contact—see Fig. 1.2—their temperature is the same within 1 part in 10^4 . How can their temperatures be so closely equal?

Fig. 1.1 Evolution of the scale factor R with the time, as predicted by Friedmann equations (from Melchiorri et al. [19])



- *The flatness problem.*

Another major cosmological problem is to understand why the universe is so flat, now, at $t \sim 10^{17}$ s, i.e. so close to the border between “open” or “closed”. Moreover, at Planck time, where \hbar_P is the reduced Planck constant,

$$t_{\text{Planck}} = \sqrt{G\hbar_P/c^5} \sim 10^{-43} \text{ s}, \quad (1.30)$$

or $T_{\text{Planck}} \sim 10^{19}$ GeV—the Planck temperature—, one can show that $\Delta\rho/\rho$ would have been $10^{-43}/10^{17} \sim 10^{-60}$. *How could Ω have been so finely tuned to unity?* Or in other words, *how could the universe have been so flat? How has the universe survived for $10^{60}t_{\text{Planck}}$, without recontracting or exhibiting noticeable negative curvature?* One needs a mechanism to reduce the curvature by a factor $10^{50}\text{--}10^{60}$.

- *The monopole problem.*

The existence of the grand unification of forces in nature implies that superheavy magnetic monopoles have been produced when $kT \sim 10^{15}$ GeV. Calculating their relic abundance, one finds that they would have overclosed the universe unless there is some mechanism to dilute their numerical density.

Inflation [20–24] can solve the horizon, flatness and monopole problems [25] and also other problems [20]. Consider the Friedman models of the universe with $\Lambda = 0$ (see Fig. 1.1) in a situation where Λ dominated the expansion in the Friedman equation such that

$$H = \frac{1}{a} \frac{da}{dt} = \sqrt{\frac{\Lambda}{3}} = \text{constant}, \quad (1.31)$$

with the solution

$$a \sim \exp(Ht). \quad (1.32)$$

This De Sitter solution, or inflation solution, is shown in the lower left corner of the plot of Fig. 1.1.

In typical models for inflation, the phase transition of a scalar field—sometimes called the inflaton field—took place when $T \sim T_{\text{GUT}} \sim 10^{16}$ GeV at $t_{\text{GUT}} \sim 10^{-32}$ s. Inflation causes the expansion to accelerate by a factor of more than 10^{26} . This is schematically shown in Fig. 1.3. After inflation stopped, the vacuum energy of the inflaton field was transferred to ordinary particles, so a reheating of the universe took place with an enormous entropy generation.

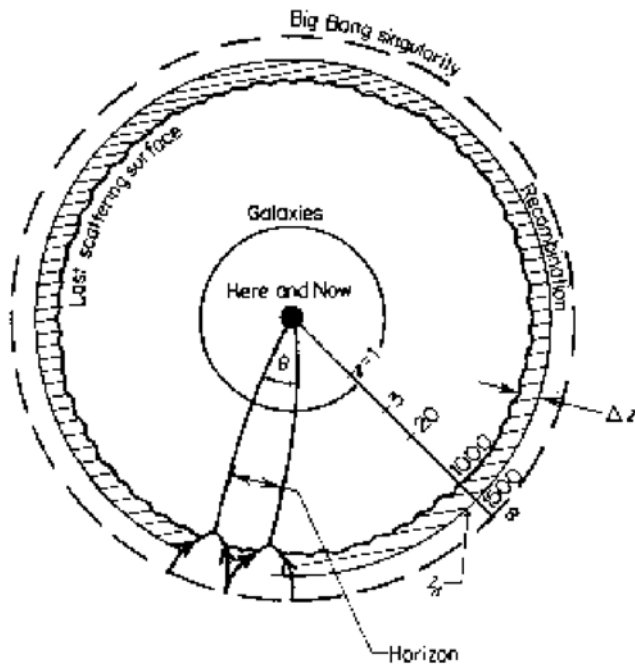


Fig. 1.2 In the cosmological model, the observer (here and now) can “understand” that the two regions—which were in causal contact—have the same temperature, within 1 part in 10^4 , but not for regions which were widely separated

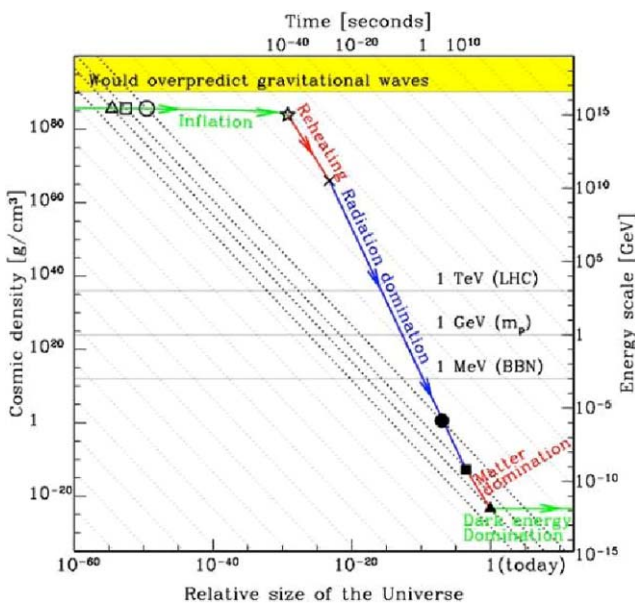


Fig. 1.3 Cosmic density versus relative size of the universe: (1) for the standard model (dotted diagonals), (2) for models with inflation; curves from Bock et al. [25]

The period of inflation and reheating is strongly non-adiabatic, since there is an enormous generation of entropy at reheating. After the end of inflation, the universe “restarts” in an adiabatic phase with the standard conservation of aT , and it is because the universe automatically

restarts from very special initial conditions that the horizon, flatness and monopole problems are avoided (see Fig. 1.3).

Inflation is an active subject of research for theoreticians. The most solid prediction from inflation is that the observable universe is flat:

$$\Omega = 1, \quad (1.33)$$

to high accuracy, and that fluctuations on large scales in the cosmic microwave background radiation should be nearly scale invariant. Moreover, primordial fluctuations should be adiabatic and nearly Gaussian. Finally, most of the scenarios predict a significant amount of gravitational waves, which could give rise to CMB anisotropy and influence polarization.

2 Decoupling particles in the early universe

The thermal history of the early universe is very simple. It just assumes a global isotropic and uniform universe (see Sect. 1.1). In its reduced version—no structure of any kind on scales larger than individual elementary particles—the contents of the universe are determined by *just physics*.

- A global expansion governed by general relativity.
- Particle interactions governed by the standard model of particle physics.
- Distributions of particles governed by the laws of statistical physics.

In effect, at early times ($T > 10^{12}$ K, $t < 10^{-4}$ s), the universe is filled up with an extremely dense and hot gas: the matter is completely dissociated and is in equilibrium with radiation.

A given species remains in thermal equilibrium as long as its interaction rate Γ is larger than the expansion rate H of the universe:

$$\Gamma \gg H, \quad (2.1)$$

where the Hubble parameter H sets the cosmological time scale and where the interaction rate Γ for a particle with cross section σ is typically of the form

$$\Gamma = n\sigma\langle v \rangle. \quad (2.2)$$

n is the numerical density and $\langle v \rangle$ the mean typical particle velocity. In the following, we briefly review the generic behavior of elementary particles in the early universe; we shall consider first particles which were in equilibrium with the surrounding thermal bath, then thermal relics, and finally possible relics which were never in thermal equilibrium.

2.1 Thermal equilibrium in the early universe

Let us focus on a generic population of particles ι and their antiparticles $\tilde{\iota}$, in thermal equilibrium (same temperature: $T_\iota = T_{\tilde{\iota}}$), with a neglected asymmetry between matter and antimatter ($n_\iota = n_{\tilde{\iota}}$), with fast annihilation and creation reactions ($\iota + \tilde{\iota} \rightleftharpoons a + \tilde{a}$), and with negligible chemical potentials.

For a gas of particles, we can describe the state in terms of a distribution function $f(\mathbf{p})$, where the energy E is related to the three-momentum \mathbf{p} and the mass m of the species ι by

$$E^2(\mathbf{p}) = m^2 c^4 + |\mathbf{p}^2| c^2. \quad (2.3)$$

In thermal equilibrium, at a temperature T , the particles obey either Fermi–Dirac or Bose–Einstein distributions:

$$f(\mathbf{p}) = \frac{1}{\exp(E(\mathbf{p})/k_B T) \pm 1}, \quad (2.4)$$

where k_B is the Boltzmann constant, and where the plus sign is for fermions and the minus sign for bosons. The numerical density, energy density and pressure of species labeled ι are respectively given by

$$n_\iota = \frac{g_\iota}{(2\pi\hbar_P)^3} \int f(\mathbf{p}) d^3\mathbf{p}, \quad (2.5)$$

$$\rho_\iota = \frac{g_\iota}{(2\pi\hbar_P)^3} \int E(\mathbf{p}) f(\mathbf{p}) d^3\mathbf{p}, \quad (2.6)$$

$$p_\iota = \frac{g_\iota}{(2\pi\hbar_P)^3} \int \frac{|\mathbf{p}^2| c^2}{3} E(\mathbf{p}) f(\mathbf{p}) d^3\mathbf{p}, \quad (2.7)$$

where \hbar_P is the reduced Planck constant ($\hbar_P = h_P/2\pi$), and where g_ι is the number of spin states of the particle ι —for photons $g_\gamma = 2$; for positrons or for electrons $g_e = 2$; for a massive boson Z $g_Z = 3$.

We can carry out the integrals over the distribution functions in two opposite limits: particles which are highly relativistic ($kT \gg mc^2$) or highly non-relativistic ($kT \ll mc^2$).

2.1.1 Numerical density

Assuming a system of units where the reduced Planck constant \hbar_P , the Boltzmann constant k_B and the speed of light c are all equal to unity, the numerical density is given by

$$n_\iota = \frac{g_\iota}{2\pi^2} T^3 \int x^2 \frac{dx}{\exp(y) \pm 1}, \quad (2.8)$$

where $x = p/T$ and $y = E/T$ (the plus sign is relative to fermions when the minus sign is for bosons).

In the ultra-relativistic limit, $m_\iota \gg T$, the numerical density can be written

$$n_\iota = \frac{\zeta(3)}{\pi^2} g_\iota T^3 \quad \text{for bosons}, \quad (2.9)$$

$$n_\iota = \frac{3}{4} \frac{\zeta(3)}{\pi^2} g_\iota T^3 \quad \text{for fermions}, \quad (2.10)$$

where $\zeta(x)$ is the Riemann zeta-function.¹ To get back to the usual system of units (CGS or MKSA), the multiplicative factor $(k/\hbar pc)^3$ must be introduced (see for instance [41]). In the non-relativistic limit, $m_\iota \gg T$, the numerical density—both for bosons and fermions—is given by

$$n_\iota = g_\iota \left(\frac{m_\iota T}{2\pi} \right)^{3/2} \exp(-m_\iota/T). \quad (2.11)$$

2.1.2 Energy density

Now let us focus on the energy density ρ_ι and on the pressure p_ι . In a system of units where $\hbar_P = k_B = c = 1$, the energy density reduces to the integral

$$\rho_\iota = \frac{g_\iota}{2\pi^2} T^4 \int \frac{x^2 y dx}{\exp(y) \pm 1}. \quad (2.12)$$

This expression needs to be multiplied by the quantity $(k_B^4/\hbar_P^3 c^3)$ in order to restore proper units [28].

In the ultra-relativistic regime, the energy density is given by the Stefan–Boltzmann law:

$$\rho_\iota = g_\iota \frac{\pi}{30} T^4 \quad \text{for bosons}, \quad (2.13)$$

$$\rho_\iota = \frac{7}{8} g_\iota \frac{\pi^2}{30} T^4 \quad \text{for fermions}, \quad (2.14)$$

and the pressure is

$$p_\iota = \frac{\rho_\iota}{3} c^2 \quad \text{for bosons and fermions}. \quad (2.15)$$

In the non-relativistic regime—for bosons and fermions—the energy density and the pressure are respectively given by

$$\rho_\iota = m_\iota n_\iota \quad \text{and} \quad p_\iota = k_B T n_\iota \ll \rho_\iota c^2. \quad (2.16)$$

From the above expressions, several pieces of information can be extracted: relativistic particles, whether bosons or fermions, remain in approximately equal abundances in equilibrium. Once they become non-relativistic, however, their abundance plummets and becomes exponentially suppressed with respect to the relativistic species. This is simply because it becomes progressively harder for massive particle–antiparticle pairs to be produced in a plasma with $T \ll m$.

Let us note that, because the energy densities of matter and radiation scale differently, the universe was radiation

¹ $\zeta(3) = 1.20206$.

dominated at early epochs, while the universe is matter dominated today.

We can write the ratio of the density parameters in matter and in radiation as

$$\frac{\Omega_m}{\Omega_r} = \frac{\Omega_{m0}}{\Omega_{r0}} \frac{a}{a_0} = \frac{\Omega_{m0}}{\Omega_{r0}} (1+z)^{-1}, \quad (2.17)$$

where the z redshift of the matter–radiation equality is thus

$$1 + z_{eq} = \frac{\Omega_{m0}}{\Omega_{r0}} \sim 3300. \quad (2.18)$$

This expression assumes that the particles that are non-relativistic today were also non-relativistic at z_{eq} ; this should be an assumption, with the possible exception of massive neutrinos, which make a minor contribution to the total density.

As we already mentioned and as we shall see later—for instance for neutrinos, for photons—even decoupled, these relativistic particles will maintain a thermal distribution. This is not because they are in equilibrium, but due to cosmic expansion. In effect, during the expansion, the distribution function is transformed into a similar function but with a lower temperature, proportional to $1+z$. We can therefore speak of the *effective temperature* of a relativistic species T_ℓ^R that freezes out at a temperature T_f and redshift z_f :

$$T_\ell^R(z) = T_f \frac{1+z}{1+z_f}. \quad (2.19)$$

A similar effect occurs for particles which are non-relativistic at decoupling, with one important difference. For non-relativistic particles, i.e. NR, the temperature is proportional to the kinetic energy, which scales as $(1+z)^2$. We therefore have

$$T_\ell^{NR}(z) = T_f \left(\frac{1+z}{1+z_f} \right)^2. \quad (2.20)$$

In either case we are imagining that the species freezes out, whether relativistic or non-relativistic, and stays that way afterward; if it freezes out while relativistic and subsequently becomes non-relativistic, the distribution function will be distorted away from a thermal spectrum.

The notion of an effective temperature allows us to define a corresponding notion of an effective number of relativistic degrees of freedom, which in turn permits one to give a compact expression for the total relativistic energy density in the early universe. The effective number of relativistic degrees of freedom, g_{eff} (as far as energy is concerned), can be defined by

$$g_{eff}(T) = \sum_{\ell=\text{bosons}} g_\ell \left(\frac{T_\ell}{T} \right)^4 + \frac{7}{8} \sum_{\ell=\text{fermions}} g_\ell \left(\frac{T_\ell}{T} \right)^4, \quad (2.21)$$

where T is the temperature of the background plasma, assumed to be in equilibrium. Then, the total energy density in all relativistic species can be written

$$\rho_r = \frac{\pi^2}{30} g_{eff}(T) T^4. \quad (2.22)$$

2.1.3 Some important formulae of the physics of the early universe

In the framework of the Friedmann–Robertson–Walker model, (that is, for small a) the curvature term was much less important than energy-density term. Except for a possible period of inflation, the contribution due to the cosmological constant was also negligible. Therefore, the Friedmann equation, for the early universe, can be written:

$$H^2 = \frac{8\pi G}{3} \rho_r \\ = \frac{8\pi G}{3} \frac{\pi^2}{30} g_{eff}(T) T^4 \sim 2.76 g_{eff} \frac{T^4}{m_{Pl}}, \quad (2.23)$$

where m_{Pl} is the Planck mass defined by

$$m_{Pl} = \sqrt{\frac{\hbar c}{G}} \sim 1.22110^{19} \text{ GeV}/c^2. \quad (2.24)$$

Therefore, one of the most important formulae of the physics of the early universe is the expansion rate:

$$H = 1.66 \sqrt{g_{eff}} \frac{T^2}{m_{Pl}}. \quad (2.25)$$

Moreover, one can add that for radiation domination:

$$H = \frac{\dot{a}}{a} = \frac{1}{2t}, \quad (2.26)$$

and the time–temperature relation becomes

$$t = 0.30 \frac{m_{Pl}}{\sqrt{g_{eff}} T^2} \sim (1 \text{ MeV}/T)^2 \text{ s}. \quad (2.27)$$

This is a convenient formula, valid during the important temperatures around 1 MeV when most of nucleosynthesis and neutrino decoupling occurred: when the temperature decreased from 1 MeV down to 0.1 MeV (from 10 to 1 billion kelvin); the age of the universe was in the range between one second and three minutes.

2.1.4 On the entropy of the early universe

Finally, we can also focus on the entropy of the primordial plasma. The first law of thermodynamics leads to the relation

$$Ts_\ell = \rho_\ell + p_\ell, \quad (2.28)$$

where s_ι is the rest-frame entropy density of the gas of particles ι . In the system of units $\hbar_P = k_B = c = 1$ [28], the entropy density may be expressed by

$$s_\iota = \frac{g_\iota}{2\pi^2} T^3 \int \frac{x^2(y + x^2/3y) dx}{\exp(y) \pm 1}, \quad (2.29)$$

where $x = p/T$ and $y = E/T$. In the ultra-relativistic regime, we find

$$s_\iota = \frac{4}{3} \frac{\rho_\iota}{T}. \quad (2.30)$$

Therefore, the entropy density for the relativistic species is given by

$$s(T) = \frac{2\pi^2}{45} g_{\text{eff}}^S(T) T^3, \quad (2.31)$$

with

$$g_{\text{eff}}^S(T) = \sum_{\iota=\text{bosons}} g_\iota \left(\frac{T_\iota}{T} \right)^3 + \frac{7}{8} \sum_{\iota=\text{fermions}} g_\iota \left(\frac{T_\iota}{T} \right)^3. \quad (2.32)$$

Numerically, $g_{\text{eff}}(T)$ and $g_{\text{eff}}^S(T)$ are very close to each other. In the standard model, they are both of the order of 100 for $T > 300$ MeV, 10 for $1 < T < 300$ MeV and 3 for $T < 1$ MeV.

The processes that change the effective number of relativistic degrees of freedom are the QCD phase transition at $T \sim 200$ MeV, and the annihilation of electron/positron pairs at 0.5 MeV. The entropy of the gas contained in a co-volume may be expressed as

$$\mathcal{S} = s(T)a^3 = \frac{2\pi^2}{45} g_{\text{eff}}^S(T) T^3 a^3. \quad (2.33)$$

Since entropy was only produced at a process like a first-order phase transition or an out-of-equilibrium decay, and since we suppose that the entropy production for such processes is very small compared to the total entropy, one can say that adiabatic evolution is an excellent approximation for almost the entire universe. The conservation of the comoving entropy of the primordial gas implies the following expression for the evolution of the temperature:

$$T \sim \left(\frac{1}{g_{\text{eff}}^S a^3} \right)^{1/3}. \quad (2.34)$$

Whenever g_{eff}^S is constant, one obtains the familiar result, $T \sim a^{-1}$.

2.2 Thermal relics

In general, particles did not stay in equilibrium forever; as we have already mentioned, eventually the density became

so low that interactions became infrequent, and particles froze out. Since most of the particles in our present universe belong to this category, it is important to study the features of that quenching and to compute the relic abundances of the remnant species. The decoupling has occurred either when the species ι was relativistic ($T_{\text{dec}} \gg M_\iota$) or when it was non-relativistic ($T_{\text{dec}} \ll M_\iota$). These two extreme cases are briefly reviewed in the following subsections.

2.2.1 Decoupling of relativistic particles or thermal decoupling

Let us focus on relativistic, or hot, particles ι . Their coupling to the *primordial plasma*—which was in thermal equilibrium—was achieved as long as the collision rate $\Gamma_\iota(T)$ of the ι with the other species was greater than the expansion rate $H(T)$ of the universe. As a consequence of the expansion, their temperature and their density decreased. Then, their collisions were more and more rare and less and less energetic. Finally, the relativistic particles ι could easily decouple from the thermal equilibrium, could behave as free particles, and could become a fossil radiation as soon as

$$\Gamma_\iota(T) = H(T). \quad (2.35)$$

As an example, we present the thermal decoupling of the neutrinos. Neutrino equilibrium was essentially maintained by weak interactions:



where all neutrino flavors are involved. The rate of their collisions with electrons and positrons can be written

$$\begin{aligned} \Gamma_\iota(T) &\sim \frac{\zeta(3) T^3}{\pi^2} \frac{G_F^2}{T^2} \\ &\sim 4.9 \times 10^{-23} \text{ MeV} \left(\frac{T}{1 \text{ MeV}} \right)^5, \end{aligned} \quad (2.37)$$

where the Fermi constant is $G_F = 1.16 \times 10^{-11} \text{ MeV}^{-2}$. The Hubble parameter is given by

$$H(T) = 1.66 \sqrt{g_{\text{eff}}} \frac{T^2}{m_{\text{Pl}}}. \quad (2.38)$$

Comparing the collision rate with the expansion rate, we can infer a freeze-out temperature close to 1–2 MeV, below which collisions were so rare that neutrinos became a fossil radiation.

After decoupling, neutrinos moved as free particles following the general expansion. They remained in a thermal Fermi–Dirac distribution with an effective temperature which satisfied the conservation of entropy:

$$g_{\text{eff}}^S(Ta)^3 = \text{constant}. \quad (2.39)$$

After the neutrino freeze-out, electrons and positrons annihilated, dumping their entropy into the photons. Calculating before and after (e^+ , e^-) decoupling, we have

$$(g_{\text{eff}}^S)_{\text{before}} = 2 + \frac{7}{8}(2+2) = \frac{11}{2}, \quad (2.40)$$

and

$$(g_{\text{eff}}^S)_{\text{after}} = 2, \quad (2.41)$$

and we find the well-known temperature difference between relic neutrinos ν and relic photons γ :

$$T_\nu = \left(\frac{4}{11}\right)^{1/3} T_\gamma. \quad (2.42)$$

It is thus easy to calculate the numerical and energy densities of the relic neutrinos. In particular, the numerical density is given from the value of the temperature:

$$n_\nu = \left(\frac{3}{4}\right)\left(\frac{4}{11}\right)n_\gamma = 112 \text{ cm}^{-3}. \quad (2.43)$$

The energy density is a function of the mass, which should be calculated numerically, but with analytical limits given from (2.13) and (2.16) for respectively $m_\nu \ll T_\nu$ and $m_\gamma \gg T_\gamma$; the latter is

$$\rho_\nu(m_\nu \gg T_\nu) = \sum_\nu m_\nu n_\nu \quad (2.44)$$

and leads to

$$\Omega_\nu h^2 = \frac{m_\nu}{93.2 \text{ eV}}. \quad (2.45)$$

Thus, a neutrino with $m_\nu \sim 10^{-2}$ eV would contribute to $\Omega_\nu \sim 2 \times 10^{-4}$. This is large enough to be interesting, without being large enough to make neutrinos dark matter! However, cosmology can provide information on the scale of the neutrino masses, complementary to the results of tritium β decay, double β decay experiments and also LEP.

For instance, analysis of the data from the anisotropies of the cosmic microwave background radiation combined with other observational and experimental results may provide upper bounds on the sum of neutrino masses. Anyway, the problem with neutrinos is that they decouple, while relativistic and hence have a comparable numerical density to that of photons. To ensure a reasonable energy density, their mass must be small.

Now we shall consider instead a species X which is non-relativistic, or cold, at the time of decoupling. It is much harder to accurately calculate the relic abundance of a cold relic than a hot one, simply because the equilibrium abundance of a non-relativistic species is changing rapidly with respect to the background plasma, and we have to be quite precise following the freeze-out process to obtain a reliable answer.

2.2.2 Decoupling of non-relativistic particles or chemical freeze-out

Let us consider some kind of particle J with antiparticle \bar{J} , which can annihilate each other and be pair created through the processes



where A stands for any type of particle to which the J can annihilate. Moreover, we suppose that, in the early universe, the A had zero chemical potential and were in thermal equilibrium with the other light particles. The accurate calculation typically involves numerical integration of the Boltzmann equation for a network of interacting particles species; here, we cut to the chase and simply provide a reasonable approximate equation.

At $T \gg M_J$, in exact thermal equilibrium, the numerical density of J particles is $n_J^{\text{eq}}(T)$ and the rate of the above process (2.46) is the same in both directions.

When $T \ll M_J$, the creation of particles is impossible, while the annihilation is again possible. Without expansion, the particles J would disappear. With the dilution due to the expansion, annihilations will be inhibited, the collisions with the other particles will rapidly stop, and the J particles become fossils: they are the *cold relics* of the universe which pervade the intergalactic medium.

If σ_{an} is the annihilation cross section of species J at the temperature $T = M_J$, the numerical density n_J of the J evolves according to

$$\frac{dn_J}{dt} = -Hn_J - \langle \sigma_{\text{an}} v \rangle [n_J^2 - (n_J^{\text{eq}})^2], \quad (2.47)$$

where the first term of the right-hand side of this equation expresses the dilution that comes from the Hubble expansion, the second term describes the annihilation and the third term the creation of pairs. From the time–temperature relation (2.27), one can transform the evolution equation (2.47) for n_J as a function of time into an evolution equation for n_J as a function of temperature. Then, one introduces the variable $x = M_J/T$ and normalizes n_J to the entropy density S through

$$Y_J = \frac{n_J}{S}. \quad (2.48)$$

The final equation for the normalized numerical density Y_J can be written:

$$\frac{x}{Y_J^{\text{eq}}} \frac{dY_J}{dx} = -\frac{\Gamma_{\text{an}}}{H} \left[\left(\frac{Y_J}{Y_J^{\text{eq}}} \right)^2 - 1 \right], \quad (2.49)$$

where $\Gamma_{\text{an}} = n_J^{\text{eq}} \langle \sigma - \text{an} |v| \rangle$; for small x , we have $Y_J = Y_J^{\text{eq}}$, since, at high T , the J particles are in thermal equilibrium. We see that the evolution is governed by the factor Γ_{an}/H ,

the interaction rate divided by the expansion rate. The solutions of (2.49) have to be obtained numerically to find, in particular, the temperature T_f and the corresponding value x_f of the freeze-out.

These solutions are represented on Fig. 2.1 for different values of $\langle \sigma_{\text{an}} |\mathbf{v}| \rangle$. In effect, on this figure, one can see that for $x = x_f$, Y leaves its equilibrium curve Y_{eq} and takes its actual value $Y = Y_{\text{real}}$ shown by the dashed lines. As can be seen, the value of x_f is lower for a smaller cross section σ_{an} : the more weakly coupled particles will decouple earlier and will have a higher relic abundance.

Going through the numerical analysis one finds that

- for neutral leptons of mass $M = 1$ GeV, which have essentially weak interactions: $x_f \sim 15$, $T_f \sim 70$ MeV,
- for charged leptons of mass $M = 1$ GeV, which have mainly electromagnetic interactions: $x_f \sim 34$, $T_f \sim 30$ MeV,
- for hadrons of mass $M = 1$ GeV, which have essentially strong interactions: $x_f \sim 40$, $T_f \sim 25$ MeV.

2.2.3 On dark-matter candidates

In Sect. 2.2.1, we have seen that hot relics—through (2.45)—cannot overclose the universe:

$$\Omega_b h^2 < 1. \quad (2.50)$$

In Sect. 2.2.2, we have focused on cold relics—particles that were non-relativistic at time of freeze-out. Through a numerical analysis, one can find that a hypothetical neutrino with a mass close to 2–3 GeV, would have the right mass to close

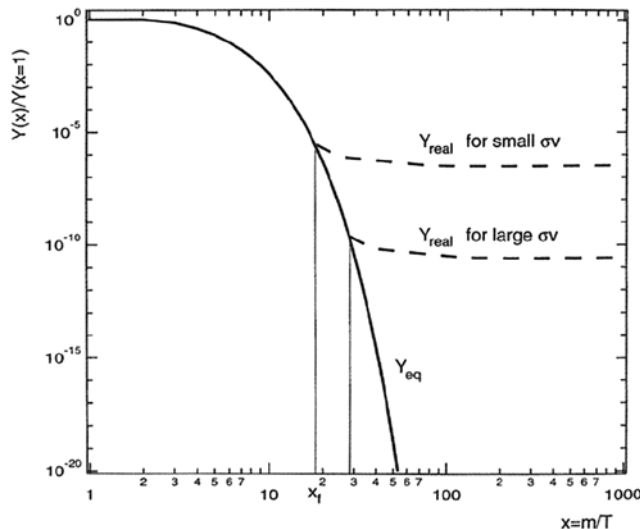


Fig. 2.1 The freeze-out of a massive particle. At a certain value $x_f = m_X/T_f$, the numerical density Y leaves an equilibrium abundance curve Y_{eq} and takes the actual abundance showed by the dashed lines. For weakly interacting massive particles, x_f is of order of 20 (from Bergstrom and Goobar [28])

the universe [28]. But data from the LEP accelerator have excluded neutrinos with a mass in the GeV range.

So, what could the dark matter be?

First, let us remark that the nature of cold dark-matter (hereafter CDM) particles may easily be known if they decay into radiation or some other identifiable particles. Anyway, one candidate for CDM is a weakly interacting particle (hereafter WIMP). One can show that a stable particle with a weak interaction cross section may produce a relic density of order of the critical density today.

The best example may be provided by the lightest supersymmetric partner (LSP), if it is stable and if supersymmetry is broken at the weak scale. Moreover, one could produce such particles in colliders and directly detect an hypothetical WIMP background in cryogenic detectors in underground laboratories [42].

An alternate candidate for the dark matter is provided by the axion which was not created in thermal equilibrium. For a mass range between 10^{-6} and 10^{-3} eV, the axion may produce a sizable relic density [43, 44]. Experimental efforts are currently done, in the interesting mass region, in the USA and Japan.

3 Primordial nucleosynthesis

Big-bang nucleosynthesis provides a probe of the early evolution of the universe and of its particle content. Light elements are important relics of the primordial universe. It is interesting to confront the predictions of the *standard big-bang nucleosynthesis* (SBBN) model for the abundances of deuterium, helium-4 and lithium-7 with the observations of the *primordial abundances* of these light elements.

The SBBN model has only one parameter, the baryon-to-photon ratio η . These abundances, which depend only on η , span some nine orders of magnitude. The synthesis of these elements strongly depends on the physical conditions of the early universe, when T was below 500 keV, when t was below 5 s.

But let us consider in some detail the SBBN model [45–50, 52, 53, 64–66].

3.1 Standard big-bang nucleosynthesis

The universe, after the big bang, was expanding and was filled with radiation. All wavelengths were stretched along with the expansion. At early times, the universe was dense and hot, and all particles were in equilibrium. As seen in Sect. 2, as the early universe expanded and cooled, interaction rates declined and, depending on the strength of their interactions, different particles fell out of equilibrium at different epochs. In particular, for the neutrinos, ν_e , ν_μ and ν_τ , the departure from equilibrium occurred when the universe

was a few tenths of a second old and the temperature of the cosmic background radiation photons, e^+e^- pairs, and the neutrinos was a few MeV. Now, let us focus on the neutron-to-proton ratio.

3.1.1 The neutron-to-proton ratio

As long as $T \gg 1$ MeV, neutrinos, electrons and positrons were in equilibrium through the n–p reactions [45, 46, 48]:



The neutron-to-proton ratio n/p was approximatively given by the Saha equation:

$$n/p = \exp(-\Delta m/T), \quad (3.4)$$

with $\Delta m = m_n - m_p = 1.293$ MeV. The neutrino number was supposed to be $N_\nu = 3$. When the reaction rate $\Gamma(T)$ fell below the expansion rate $H(T)$, the weak interactions were frozen out and neutrons and protons ceased to interconvert. The equilibrium abundance of neutrons at this freeze-out temperature T_f were about 1/6 the abundance of protons: $(n/p)_f \sim 1/6$. The neutrons have a finite lifetime ($\tau = 890$ s) that was somewhat larger than the age of the universe at this epoch, $t(1 \text{ MeV}) \sim 1$ s, but they gradually decayed into protons and leptons. Soon thereafter, however, the universe reached a temperature somewhat below 100 keV, and big-bang nucleosynthesis began. At that point, the n/p ratio had approximately the following value:

$$(n/p)_{\text{nuc}} \sim \frac{1}{7}. \quad (3.5)$$

Fig. 3.1 Network of nuclear reactions that determines the yields in standard big-bang nucleosynthesis (from Nollett and Burles [63])

The universe was about 100 second old.

3.1.2 Helium synthesis

While neutrons and protons were interconverting, they were also colliding among themselves, creating deuterons:

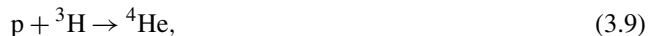


At early times, the deuteron was photodissociated before it could capture a neutron, or a proton, or another deuteron:



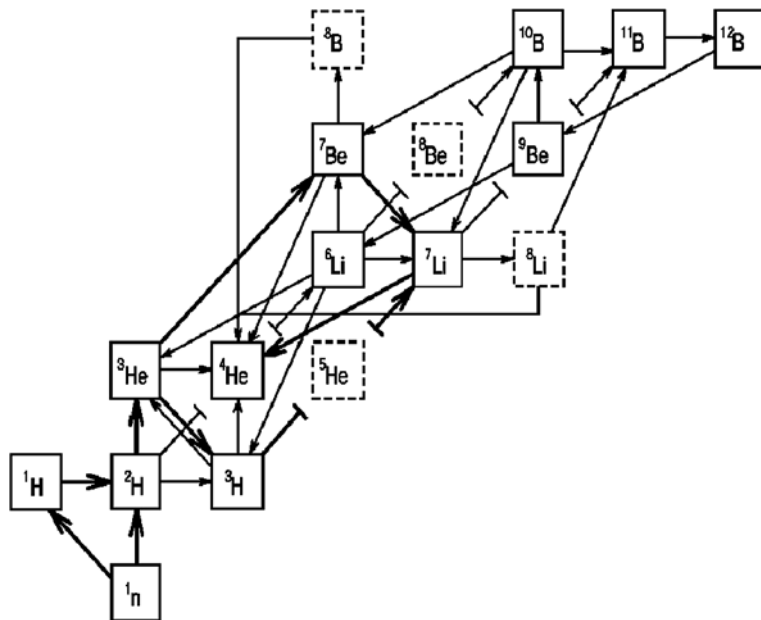
to build the heavier nuclides.

This famous *bottleneck* to big-bang nucleosynthesis persisted until $T \sim 0.1$ MeV. Below this temperature, photodesintegration became inefficient; then, nuclei more complex than deuterium were built through the following reactions (see Fig. 3.1):



Since there are no stable mass-5 nuclides, a *gap* appears at mass-5. The few reactions that bridged the mass-5 gap led mainly to mass-7: ${}^7\text{Li}$ and ${}^7\text{Be}$.

Finally, heavier elements were produced in truly negligible quantities, since there was another gap at mass-8.



In fact, there were only some traces of beryllium-9 and boron-11. The primordial nuclear reactor was short-lived.

In the framework of the SBBN model, as the temperature dropped below $T < 30$ keV, when the universe was close to 20 min old, Coulomb barriers suppressed all nuclear reactions. Afterwards, until the first stars formed, no new nuclides were created.

Before presenting the predictions of the SBBN model, let us note that the dominant product of big-bang nucleosynthesis was ^4He , and its abundance was very sensitive to the $(n/p)_{\text{nuc}}$ ratio. Introducing $n_{\text{tot}} = [n + p]_{\text{nuc}}$, the abundance of helium ^4He that forms is

$$Y(^4\text{He}) = \frac{n_4}{n_{\text{tot}}} = \frac{2(n/p)_{\text{nuc}}}{1 + (n/p)_{\text{nuc}}} \sim 0.25, \quad (3.13)$$

i.e. an abundance of ^4He close to 25% by mass. Lesser amounts of the other light elements were produced: D at the level of about 10^{-5} by number and ^7Li at the level of 10^{-10} by number.

3.1.3 Predicted abundances of light elements

In the SBBN model with $N_v = 3$, the only free parameter is the density of baryons, Ω_b or η , the ratio of the number of baryons n_b to the number of photons n_γ :

$$\eta = \frac{n_b}{n_\gamma}. \quad (3.14)$$

As will be seen from SBBN, and as is confirmed by a variety of astrophysical data, η is very small, so it is convenient to also introduce $\eta_{10} = 10^{10}\eta$ and to use it as one of the parameters for BBN.

Having dealt with the breaking of weak equilibrium between neutrons and protons, one has to consider the onset of nuclear reactions which build up the light nuclei. This has been studied by numerical solution of the complete nuclear reaction network.

The initial Wagoner [45] numerical code—which has been significantly improved and upgraded by Kavano [61]—is again available for public download [62].

Later, Sarkar [49] discussed the elemental abundances with a semi-analytical method estimating reaction rates and uncertainties in primordial nucleosynthesis. In their poster for the APS centennial meeting, Burles et al. [51] showed that after five minutes—see Fig. 3.2—most of the neutrons were in helium-4 nuclei, most protons were free, while much smaller amounts of deuterium, helium-3 and lithium-7 were synthesized. This elemental composition was unchanged until the formation of the first stars.

The yields of primordial nucleosynthesis are shown as a function of baryon density $\Omega_b h^2$ or the baryon-to-photon ratio η in Fig. 3.2 [65].

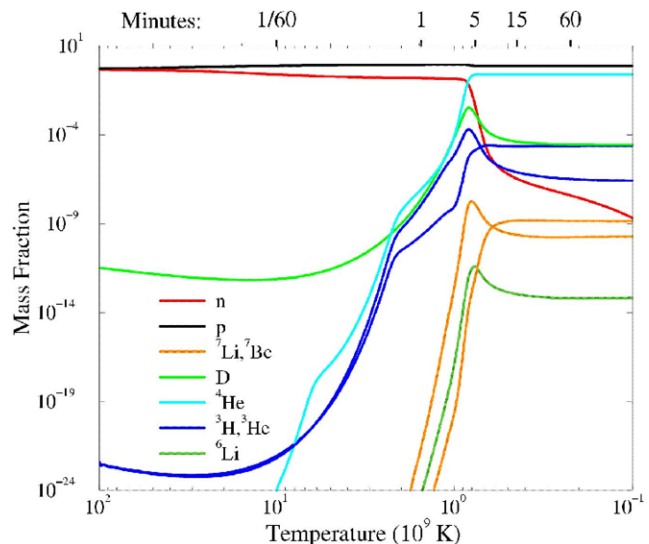


Fig. 3.2 Time–temperature evolution of the primordial nucleus in standard cosmological model (from Burles and Nollett [51]). Let us note that at very high temperatures the number of protons should be equal to the number of neutrons

The four curves of Fig. 3.3 represent the abundance ratio predicted by SBBN: the top curve is the helium-4 mass as a fraction of the mass of all baryons, while the three lower curves are the number fractions of deuterium, helium-3 and lithium-7 with regard to hydrogen.

In the standard model with $N_v = 3$, the only free parameter is the density of baryons, which sets the rates of the strong reactions.

Thus, any abundance measurement determines $\Omega_b h^2$ or η , while additional measurements *overconstrain* the theory and thereby provide a consistency check. SBBN has historically been the prime means of determining the cosmic baryon density.

For instance, in Fig. 3.3, the five boxes represent some of the various measurements of primordial helium-4, deuterium, helium-3 and lithium-7, but deuterium plays the historical role of first-rate *baryometer* since the vertical band that covers the D/H data determines the baryon-to-photon ratio: $\eta_{10} = 5.9 \pm 0.5$. This value corresponds to a cosmological baryon density of

$$\Omega_b h^2 = 0.0214 \pm 0.0020. \quad (3.15)$$

As Kirkman et al. [65] remarked, it is expected that all the data boxes of Fig. 3.3 should overlap the vertical band that covers the D/H data. They do not, probably because of systematic errors. But since 2006, with the new CMB anisotropy measurements—which will be described in Sects. 8 and 10—CMB may be a much better *baryometer* than SBBN.

Recently, the team of the satellite WMAP (Wilkinson Microwave Anisotropy Probe) released their analysis after

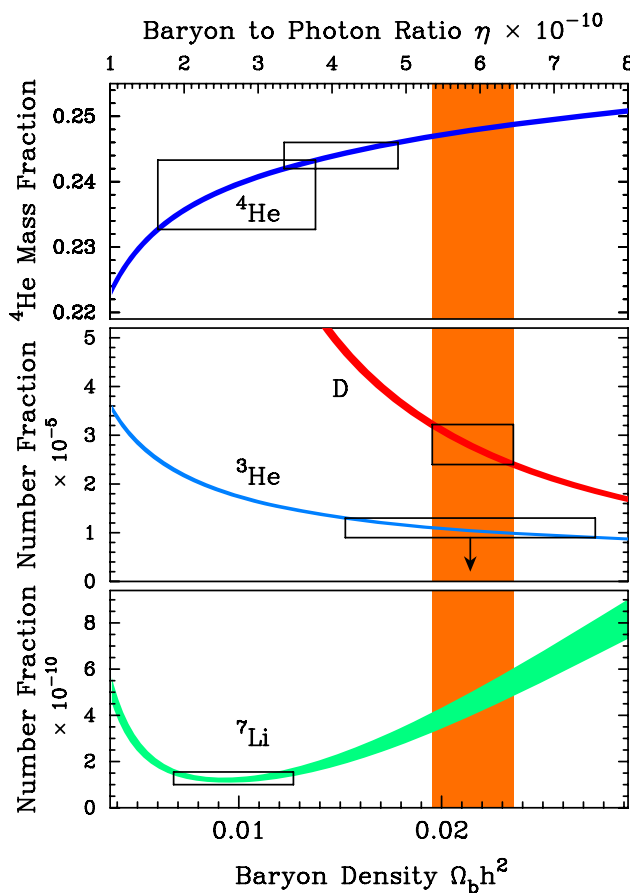


Fig. 3.3 Comparison of predicted and measured abundances of D, ^3He , ^7Li and Y_p as a function of the baryon-density parameter $\Omega_{\text{b}}h^2$ or the baryon-to-photon ratio η . The four curves show the predicted abundance by the SBBN model. The five boxes represent some of the measurements of primordial abundances (the larger ^4He box from Olive et al. [71], the smaller ^4He box from Izotov and Thuan [69], the deuterium box from Kirkman et al. [65], the ^3He box from Bania et al. [83], the ^7Li box from Ryan et al. [79])

three-year data taking of microwave background anisotropy measurements and gave the following value for the baryon density [66]:

$$\Omega_{\text{b}}h^2 = 0.0223 \pm 0.0007, \quad (3.16)$$

which corresponds, for the baryon-to-photon ratio $\eta_{10} = (273.9 \pm 0.3)\Omega_{\text{b}}h^2$, to the approximate value

$$\eta_{10} \sim 6.11 \pm 0.20, \quad (3.17)$$

with $\Omega_{\text{b}}h^2$ fixed by the CMB radiation, and precision comparisons to the most recent observations can now be attempted (see later below, the value given by the five-year WMAP data in Sect. 10).

3.2 Observations of primordial abundances

The primordial abundances of the light elements are not measured easily and simultaneously. The main difficulties come from systematic uncertainties in inferring abundances from observations and in modeling their chemical evolution since the big bang. As a propaedeutic, one describes a generic program which may be done for each of the nuclei.

3.2.1 A generic program for obtaining primordial abundances

- *Observations.* The program begins with observations of, in general, some atomic or molecular spectral line. Moreover, in the case of deuterium, for instance, one may observe one isotope in the presence of another one, which is 10 000 or 100 000 times more abundant. Finally, the various isotopes may be observed in different astrophysical sites, because of their different properties.

- *Conversion of observed lines into abundances.* In general, each isotope is detected by measuring an atomic or a molecular spectral line. It is a non-trivial task to obtain, from this observed line, an abundance of the isotope, which is the ratio of the number density of this isotope to the numerical density of hydrogen.

- *Corrections for chemical evolution.* Except for deuterium, all isotopes have potential sources which could have increased their abundances since the epoch of primordial nucleosynthesis. All, except helium-4, have significant sinks, which could have decreased their abundances since the epoch of primordial nucleosynthesis. Therefore to arrive at a *primordial abundance*, one must have: (1) a theoretical understanding of all the mechanisms of production and destruction of the isotope, and (2) several observations of different objects in order that all the free parameters, introduced in the previous steps, can be determined.

- *The primordial abundance for each isotope.* Finally, one arrives at a value for each abundance with the required precision. This required precision had varied with time, and it is in general just at the level of, or slightly beyond, current capabilities.

3.2.2 Primordial abundance of helium-4

• *Observations.*

Helium-4 can be observed in galactic and extragalactic HII regions—regions of hot and ionized H gas—using either optical or radio recombination lines. However, the best determinations come from observations of (HeII, HeI) recombination lines in metal-poor extragalactic HII regions.

• *Conversion of observed lines into abundances.*

Deriving an abundance from the observed lines should be

straightforward. However, corrections must be applied to compensate for excitation effects.

- *Corrections for chemical evolution.*

In stars, most of the hydrogen is converted into helium-4, which is converted into heavier elements. Then an excess of helium-4 can return into the interstellar medium. Therefore, one must account for a possible helium enrichment.

- *Primordial abundance for helium-4.*

There is a lot of independent recent and less recent observations and analyses leading to some values of Y_p . For illustration, Fig. 3.4 gives a compilation of the first measurements of the helium-4 mass fraction as a function of the oxygen abundance, which is an indicator of stellar processing.

First, there have been two, largely independent, estimates of Y_p , based on analyses of large data sets of low-metallicity, extragalactic HII regions: the Izotov and Thuan estimates [68, 69] and the Olive and Steigman [70–72]. More recently, Izotov and Thuan have expanded their original data set and attempted to account for uncertainties [73, 74]. Note also other work done on estimates of Y_p by Gruenwald et al. [75], Fukugita and Kawasaki [76], and Peimbert et al. [77]. Finally, recently, Steigman [67] has described and analyzed all these observational data and has chosen for the primordial helium-4 abundance

$$Y_p = 0.240 \pm 0.006. \quad (3.18)$$

3.2.3 Primordial abundance of lithium-7

- *Observations.*

Lithium absorption lines can be relatively easily observed and measured in stars. There is a wealth of data on the abundances of lithium-7 in hot population-II halo stars, since the

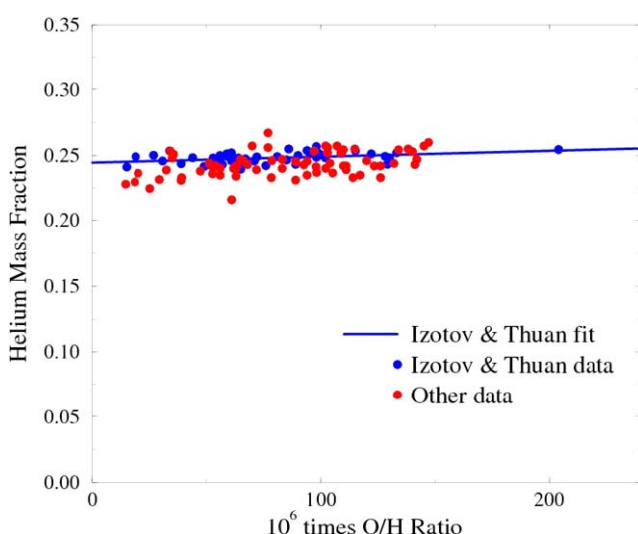


Fig. 3.4 Compilation of measurements of ${}^4\text{He}$ mass fraction versus O/H (indicators of stellar processing) from HII regions (large clouds of ionized hydrogen) (from Burles and Nollett [51])

first measurements of Spite and Spite [78]. The most relevant data come from studies of the very metal-poor stars in the halo of the galaxy or in globular clusters.

- *Conversion of observed lines in abundances.*

The observed line gives the stellar photospheric abundance via a standard stellar atmospheric technique. For stars with a surface temperature $T > 5500$ K and a metallicity less than about 1/20th the solar metallicity, the abundances practically show no dispersion. The famous *lithium plateau* for such stars is shown in Fig. 3.5.

- *Corrections for chemical evolution.*

The problem arises in relating the observed abundance to the cosmic abundance, i.e. the abundance of the star when it formed. There is a possibility that lithium has been depleted in these stars, though the lack of dispersion in the lithium data—at least in the hotter stars as seen in Fig. 3.5—limits the amount of depletion. Moreover, since the big bang, lithium-7 has been also produced through spallation by cosmic rays and also synthesized in type-II supernovae, via the neutrino process. Ryan et al. [79, 80] have undertaken some observations—in particular, studies of possible correlations between Li and Fe—to constrain the evolution of lithium-7.

The primordial abundance of lithium-7.

Ryan et al. [80], from data from studies of halo stars, find

$$\left(\frac{\text{Li}^7}{\text{H}}\right)_p = 1.23_{-0.16}^{+0.340} \times 10^{-10}, \quad (3.19)$$

in conflict with the result derived by Bonifacio et al. [81, 82], from a sample of globular cluster stars:

$$\left(\frac{\text{Li}^7}{\text{H}}\right)_p = 2.19_{-0.38}^{+0.460} \times 10^{-10}. \quad (3.20)$$

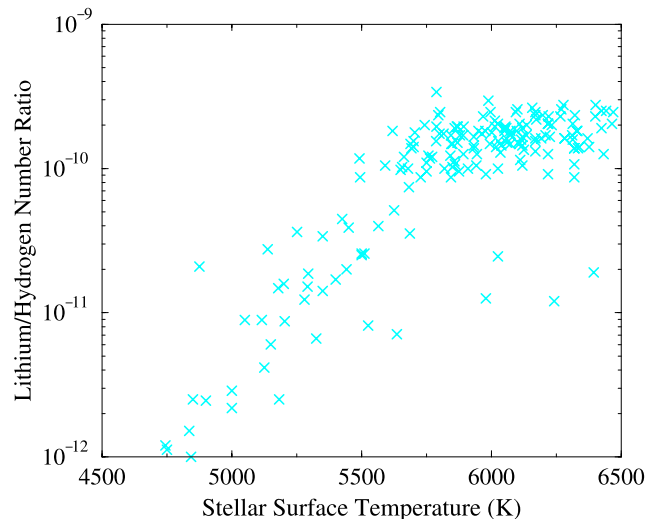


Fig. 3.5 Measurements of the ${}^7\text{Li}/\text{H}$ ratio as a function of stellar surface temperatures from the atmosphere of population-II stars in the halo of our galaxy. The *lithium plateau* for the stars with higher surface temperature is evident (from Burles and Nollett [51])

3.2.4 Primordial abundance of deuterium

The determination of the primordial abundance of deuterium presents certain difficulties: all deuterium is primordial, but some of this deuterium has been destroyed.

There are many measurements of the D/H ratio in the interstellar medium. But we do not know the history of the galaxy well enough to reconstruct the primordial D from galactic observations, while it is possible to detect D in high-redshift low-metallicity quasar absorption line systems. In fact, the primordial deuterium abundance has been measured in high-z hydrogen clouds, which are *seen* by their distinctive Lyman- α features in the spectra of several quasars; see [65] and references therein.

Figure 3.6 shows this feature in the spectrum of the quasar QSO 1937-1009. In his recent review, Steigman [67] describes, analyses and discusses the reasonably firm deuterium detections. Finally, he adopts for the primordial abundance deuterium

$$\left(\frac{D}{H}\right)_p = 2.68^{+0.270}_{-0.25} \times 10^{-5}. \quad (3.21)$$

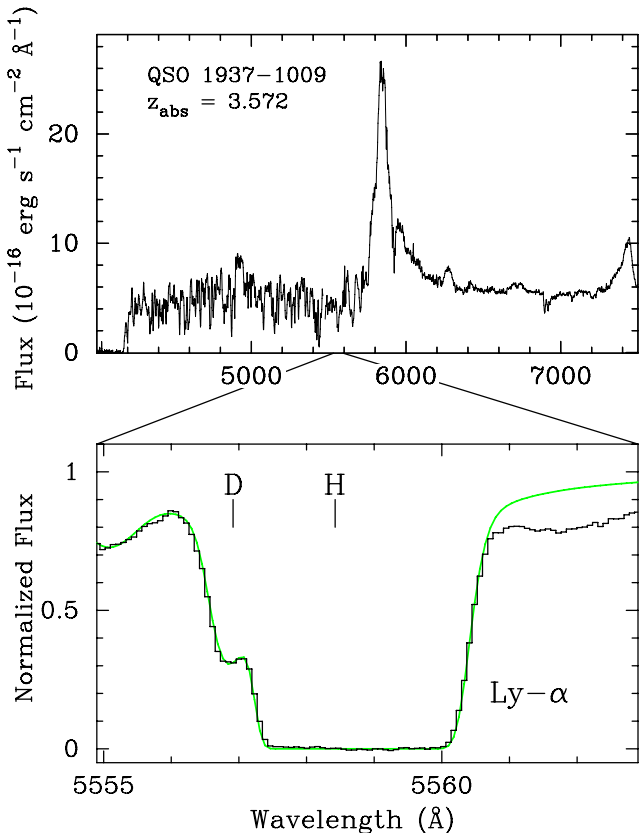


Fig. 3.6 D/H measurements, through the spectrum of the quasar QSO 1937-1009, which show the Lyman- α absorption feature from a cloud at $z = 3.572$ (from Burles and Nollett [51])

3.2.5 Primordial abundance of helium-3

Finally, for the primordial abundance of helium-3, one can adopt the upper limit measured by Bania et al. [83]:

$$\left(\frac{\text{He}}{\text{H}}\right)_p < 1.1 \pm 0.2 \times 10^{-5}. \quad (3.22)$$

But helium-3 can be better seen as a probe of the galactic chemical evolution than a cosmological probe.

3.2.6 Conclusions on observations of primordial abundances

All the above primordial abundances of helium-4, lithium-7 and deuterium can be summarized in Fig. 3.7, due to Steigman [67]. This figure shows the predicted values of η_{10} corresponding to the various primordial abundances given in previous subsections and the value η —CMB/LSS inferred from the three-year WMAP data [14], and the large-scale structure data [84]:

$$\eta_{\text{CMB/LSS}} = 6.11 \pm 0.20. \quad (3.23)$$

If the CMB/LSS data are taken to be the best baryometer, there is agreement on the predictions of the SBBN model

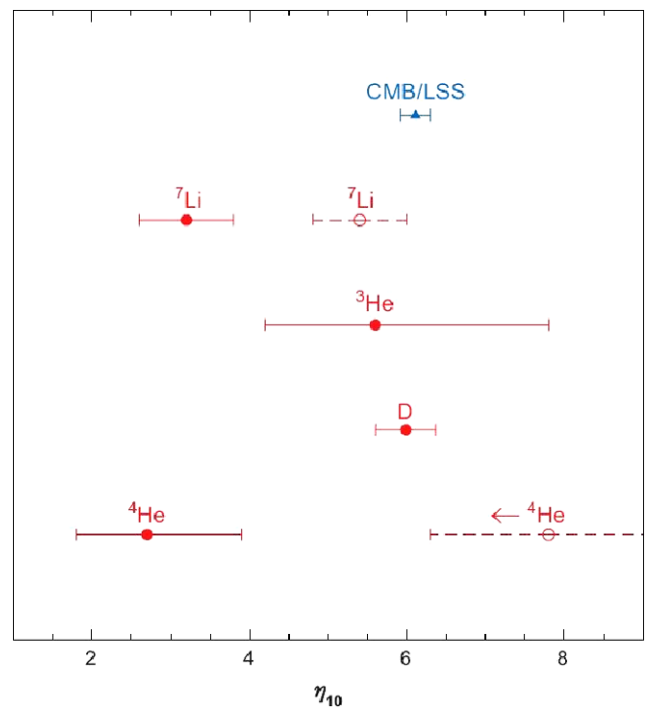


Fig. 3.7 The SBBN-predicted values of η_{10} (from Steigman [67]), their 1σ uncertainties (red filled circles), corresponding to the primordial abundances adopted by Steigman [67] and to the values CMB/LSS inferred from WMAP [14] and LSS [84] data (blue triangle). The open circles and dashed lines correspond to the alternate abundances proposed for ^4He and ^7Li by Steigman [67]

for the abundance of D and the observations of D but not for primordial ^4He and ^7Li . This disagreement between predictions and observations for ^4He and ^7Li is, as Kirkman et al. [65] and Steigman [67] said, certainly due to systematic uncertainties. More observations and more theoretical work needs to be done.

3.3 On non-standard BBN models

The above bounds on η were obtained in the framework of the standard BBN model, which assumes one and only one parameter η . But variant models of BBN exist. Below, we briefly discuss some deviations from SBBN.

3.3.1 On non-standard BBN models of Steigman's Group

The first departure from standard BBN is to assume that

- (i) the number of neutrinos species is $N_\nu = 3 + \Delta N_\nu$;
- (ii) there is a significant neutrino asymmetry parameter:

$\xi_e = \mu_e/k_B T$, where μ_e is the chemical potential of e^- . In particular, Kneller and Steigman [67, 85] have studied a BBN model with the three parameters η , ΔN_ν and ξ_e and showed that the ranges of the BBN parameters permitted by the data are small. They also show that D and ^4He abundances can constrain some classes of non-standard physics.

3.3.2 On inhomogeneous BBN models

There are possible variants of primordial nucleosynthesis with more parameters than the only one, η , of the SBBN model. The most motivated departure from standard BBN is the possibility that nucleosynthesis occurred in an inhomogeneous medium.

In the framework of these *inhomogeneous big-bang nucleosynthesis* (or IBBN) models, the formation of baryon inhomogeneous regions took place, for example during a first-order quark–hadron phase transition [54–56] or during the electroweak phase transition [57–59].

Moreover, inhomogeneities may have a particular symmetry. Lara et al. [60], who review various IBBN models, show that although the parameter space is more and more limited by more and more observations, interesting regions remain and IBBN continues to be a possibility for the early universe.

3.4 Conclusions

In the comparison of the abundance data with the theoretical expectations, we have noted the rather unsatisfactory state of the observational situation today. Whereas there has been some concerted effort in recent years towards precise abundance determinations, the quoted numbers, in particular for

the ^4He and ^7Li abundances, are still plagued by uncertain systematic errors. Moreover, CMB is a better baryometer than D.

Our understanding of the CMB has been revolutionized by the accurate and consistent database provided first by the COBE mission and then by the WMAP mission. A similar revolution is overdue for primordial nucleosynthesis.

4 The cosmic microwave background spectrum

Beyond any doubt, the CMB represents the first and best studied *cosmic relic*. The CMB provides a strong observational foundation for the standard cosmological scenario, the big-bang theory.

The success of primordial nucleosynthesis calculations requires a cosmic background radiation (CBR) characterized by a temperature of $k_B T \sim 1$ MeV at a redshift of $z \sim 10^9$. In their pioneering works, Gamow, Alpher and Herman [86–88] realized this requirement and predicted the existence of a faint residual relic of the primordial radiation, with a present temperature of a few kelvin.

The observed CMB is interpreted as the current manifestation of the hypothesized CBR. In 1964, the CMB was experimentally discovered by Penzias and Wilson [7]. The theoretical explanation of Dicke's Princeton team was published in an accompanying paper [89]. Then, the following decades saw huge advances in the measurement of the CMB radiation, with COBE's definitive discovery of anisotropies and measurement of a near perfect black-body spectrum.

The small deviations from isotropy—measured in particular by COBE and later by WMAP—have told us and will continue to tell us a great deal about the inhomogeneities in our universe. The small deviations from a black-body spectrum can also tell us about the energetics in our universe. Such deviations have already been discovered in the direction of clusters of galaxies. But the mean CMB radiation spectrum is, so far, indistinguishable from a black-body spectrum at 2.725 K.

This chapter gives an introduction to the observed spectrum of the CMB radiation, reviews observations of this CMB spectrum and discusses what can be learned about it. Earlier reviews and proceedings of conferences on the CMB spectrum can be found in [90–103].

4.1 On the thermal nature of the CMB spectrum

In the framework of the big-bang theory, extrapolating the expansion back to early epochs, the universe would have been hot and dense, and the universe would have been expanding rapidly in order to grow as large as it now can be observed to be. When the matter in the universe is hot and dense, the time to reach equilibrium is short. Thus, matter

rapidly approaches thermal equilibrium and photons should have a black-body spectrum at early times.

As already said, wavelengths are stretched with the cosmic expansion, while the frequencies scale inversely due to the same effect. The effect of cosmic expansion on the initial black-body spectrum is to retain its black-body nature, but just at lower and lower temperatures or lower and lower redshifts, since $T \sim 1 + z$.

Thus, as a first approximation we expect today's photons to have a black-body spectrum. The fact that the CMB radiation has nearly a black-body spectrum is strong evidence in support of the big-bang hypothesis. However, as discussed below, one can estimate that for each atom, the universe includes more than 10^9 photons. With so many more CMB photons than protons or electrons, matter cannot significantly distort the spectrum of the CMB radiation. The observed CMB spectrum, being so close to a black-body spectrum, should come as no surprise.

Now, let us recall some properties of a Planckian spectrum. In particular, the photon distribution $\eta_\nu^{\text{BB}}(\nu)$ —the photon density per unit of frequency interval—for a black-body spectrum is given by

$$\eta_\nu^{\text{BB}}(\nu) = \frac{1}{\exp(h_P\nu/k_B T) - 1}. \quad (4.1)$$

With the observed present CMB temperature of 2.725 K, we can calculate the number of photons in the CMB (see (2.5)):

$$n_\gamma = \frac{2\zeta(3)}{\pi^2} T_\gamma^3 = 413 \left(\frac{T_{\text{CMB}}}{2.725 \text{ K}} \right)^3 \text{ cm}^{-3}. \quad (4.2)$$

We can also compute the present energy density in CMB photons:

$$\rho_\gamma = \frac{\pi^2}{15} T_\gamma^4 \sim 4.68 \times 10^{-34} \text{ g cm}^{-3}, \quad (4.3)$$

and the entropy of CMB radiation is given by

$$s_\gamma = \frac{4}{3} \frac{\rho_\gamma}{T_\gamma} = \frac{4\pi^2}{45} T_\gamma^3, \quad (4.4)$$

while the ratio s_γ/n_γ is given by

$$\frac{s_\gamma}{n_\gamma} = \frac{2\pi^4}{45\zeta(3)} \sim 3.6. \quad (4.5)$$

Since—during the cosmic expansion—the temperature scales as $T_0 = T_i(1 + z_i)$, we can calculate the photon numerical density, $n_{\gamma i} = (1 + z_i)^3 n_\gamma$, and energy density, $\rho_{\gamma i} = (1 + z_i)^4 \rho_\gamma$, for any epoch i with redshift z_i . Moreover, as we have seen in Sect. 1, we can introduce the dimensionless Ω_γ through the relation: $\rho_\gamma = \rho_c \Omega_\gamma$.

The fraction of total energy in the universe in the form of relic radiation ($T_\gamma = 2.725$ K) is thus

$$\Omega_\gamma h^2 \sim 4 \times 10^{-5}. \quad (4.6)$$

The energy density at present is thus dominated by matter, since $\Omega_m h^2 \sim 0.127$. But let us also remark that $n_b/n_\gamma \sim 10^{-10}$.

One of the problems of modern cosmology is to understand why the present baryon number is so small. Another way to describe the puzzle for cosmologists could be formulated thus:

How did the universe evolve from early times, in which there were equal numbers of baryons and antibaryons, to the present universe in which there is a precisely measured—through BBN and CMB—“baryon asymmetry of the universe”?

All the solutions to this puzzle provide examples of the interplay between particle physics and cosmology. In effect, many theories beyond the standard model of particle physics when considered in the context of the expanding universe could lead to mechanisms which could explain the “baryon asymmetry of the universe”. Moreover, future experiments, such as the Large Hadron Collider (hereafter LHC) and the International Linear Collider (hereafter ILC), will refute or confirm these mechanisms.

If the cosmic microwave background radiation decoupled from matter at a redshift of about 1000, the scale factor of the universe was about 1000 times smaller than its current size, and the original wavelength of the radiation was 1000 times smaller than that observed today.

In Sect. 5, we shall describe the *recombination epoch* and we shall make precise the redshift of the matter–radiation decoupling.

In order to fully understand the various observations of the CMB radiation, a few words of a technical nature are needed. The spectral brightness I_ν is defined as the incident energy per unit area, per unit solid angle, per unit frequency, per unit time. It may be written

$$I_\nu = \frac{2h_P\nu^3}{c^2} \eta_\nu^{\text{BB}}, \quad (4.7)$$

where η_ν^{BB} is given by (4.1). Therefore, in natural units I_ν (in $\text{W Hz}^{-1} \text{ m}^{-2} \text{ sr}^{-1}$) we have

$$I_\nu = \frac{2h_P\nu^3}{c^2} \frac{1}{\exp(h_P\nu/k_B T) - 1}. \quad (4.8)$$

The high-frequency ($h_P\nu \gg k_B T$) limit of the Planck spectrum is known as Wien's law:

$$I_\nu^W = \frac{2h_P\nu^3}{c^2} \exp(-h_P\nu/k_B T), \quad (4.9)$$

while the low-frequency ($h\nu \ll k_B T$) limit of the Planck spectrum is known as the Rayleigh–Jeans law:

$$I_v^{\text{RJ}} = \frac{2h_P^2 k_B T}{c^2}. \quad (4.10)$$

4.2 On observations of the CMB spectrum

Since 1946–1948, a firm prediction for the existence of a universal black-body radiation was available in the scientific literature. In 1950, Gamow [104] rederived the value of the CMB temperature in a paper published in Physics Today, giving a value of 3 K. The computation was repeated in 1953, for a Danish journal [105], leading to 7 K and in 1956, for Vista in Astronomy [106], to a value of 6 K.

Alpher and Herman also published these predictions several times [107–109]. Later on, Alpher and Herman [110] have underlined that the first prediction of CMB is in their 1948 paper [88] and not in the previous papers by Gamow [86, 87].

We think that the first prediction has to be attributed to Gamow. Let us also note that Gamow was never strongly interested in establishing the priority of his CMB prediction, because he was convinced that CMB was well below the possibility of any detection.

After this long period of prediction, we can easily distinguish three epochs:

- (i) the epoch of the discovery;
- (ii) the epoch of the confirmation of the Planckian character of the spectrum;
- (iii) the epoch of the search for spectral distortions.

4.2.1 From the discovery until COBE

By the 1960s, Dicke and his colleagues, at Princeton University in New Jersey (USA), had begun to build the hardware required to search for the CMB radiation. Simultaneously, Penzias and Wilson of the Bell Telephone Laboratories—involved in the NASA Project ECHO—were calibrating microwave detectors in order to make astronomical observations in the centimeter waveband. Before the Princeton Group could complete a measurement of $T_{\gamma 0}$, Penzias and Wilson had observed a weak background signal at the radio wavelength of 7.35 cm in the large horn antenna of Holmdel, also in New Jersey. Their measurements did indicate a black-body radiation at 3.5 K:

$$T_{\gamma 0}(7.35 \text{ cm}) = 3.5 \text{ K} \pm 1 \text{ K}. \quad (4.11)$$

This observation was published in 1965 [7] under the modest title *A Measurement of Excess Antenna Temperature at 4080 MHz* along with the paper by Dicke, Peebles, Roll and Wilkinson [89] appearing as a companion article to explain the fundamental significance of this measurement.

This detection of the CMB radiation was recognized as the most spectacular evidence supporting the big-bang theory after Hubble's discovery of the expansion of the universe. But it is also very important to emphasize that Penzias and Wilson had only measured a radiation flux at a single wavelength.

One must note that the CMB radiation was first seen via its effect on the interstellar CN radical by, for instance, Adams [111], McKellar [112] in 1941, Herzberg [113] in 1950 and others. For an example, McKellar [112], from data due to Adams [111] relative to the absorption of CN in an interstellar molecular cloud derived in 1941 the excitation temperature of the rotational states to be around 2.3 K, with no obvious source of excitation.

But one must also remark that the significance of these data was not realized until after 1965 by, in particular, Thaddeus [114] in 1972, Kaiser and Wright [115] in 1990, Roth et al. [116] in 1993 and others.

Let us only note that these interstellar CN measurements at wavelengths 2.64 and 1.32 mm provided cosmologists with a way to determine $T_{\gamma 0}$ that was completely independent of ground-based or rocket-borne techniques.

Generally speaking, the measurements of the CMB spectrum could be divided in three epochs. The first set of measurements, carried out before 1975, were essentially directed towards testing the existence and the nature of CMB, such as the millimetric observations done by the Firenze Group of Melchiorri [19, 117].

The second set of measurements, covering the period from 1975 up to 1990, observing primarily the low-frequency (Rayleigh–Jeans) region of the spectrum, was dominated by the results of the so-called *White-Mountain Collaboration* (Berkeley–Bologna–Milano–Padua); all these results are presented in many reviews [19, 118].

The last set of observations were from rocket-borne experiments and from the COBE satellite. Most of these data are shown on Fig. 4.1.

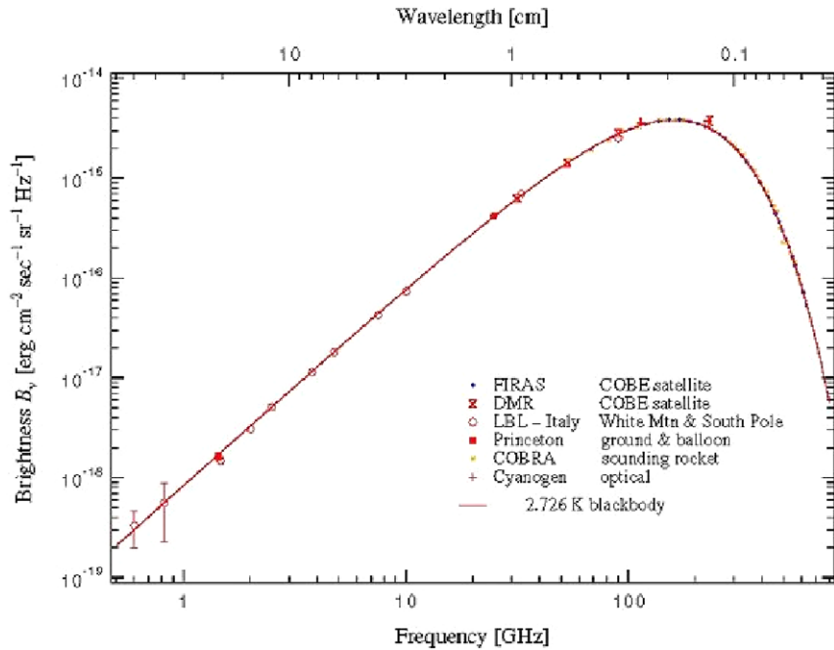
4.2.2 The CMB spectrum from FIRAS aboard COBE

Before describing these COBE data on the CMB spectrum, let us give some details. The three experiments aboard the COBE—the Cosmic Background Explorer—satellite are the Far-Infrared Absolute Spectrophotometer (60–630 GHz, FIRAS), the Differential Microwave Radiometers (30–90 GHz, DMR), and the Diffuse InfraRed Background Experiment [2.2; 2.4] μm, DIRBE). Mather, Principal Investigator of FIRAS and Smoot, Principal Investigator of DMR, were awarded the 2006 Nobel Price in physics.

The FIRAS experiment has given an absolutely beautiful measurement of the flux from the sky between 2 and 20 cm⁻¹ (i.e. 6–630 GHz). The intensity of the background sky radiation is consistent with a black body at [119]:

$$T_{\text{COBE}} = 2.728 \pm 0.002 \text{ K}. \quad (4.12)$$

Fig. 4.1 Collection of selected data, until COBE, relative to the CMB spectrum



When the FIRAS investigators released their results, they claimed that deviations from this black-body spectrum, at the spectral resolution of the instrument, are less than 1% of the peak brightness. The measured spectrum by FIRAS is shown in Fig. 4.2.

The peak of the CMB is near $\nu \sim 5.5 \text{ cm}^{-1} \sim 165 \text{ GHz}$. The intensity measured there is roughly 385 MJy sr^{-1} . Figure 4.3 shows the deviations from a black-body spectrum published by Mather et al. [120].

Note that measurements of the CMB spectrum, at the present level of sensitivity, face significant problems of foreground contamination. Figure 4.4 shows the CMB anisotropy (see Sect. 8) and the various major components of the microwave sky [118, 121]. Emission due to galactic synchrotron radiation from energetic electrons in interstellar magnetic fields, and due to bremsstrahlung from thermal

electrons in ionized HII regions dominates at very low frequencies. At high frequencies, the dominant source is cold interstellar dust.

The decrease of the galactic electron emission with frequency along with the increasing dust emission combine to create a broad window throughout the microwave region where the cosmic background dominates. However, since we cannot expect to observe the CMB radiation outside of the galaxy, this is a fundamental limitation. Many of the results given by the FIRAS team include significant corrections for these contaminations.

On the other hand, while the bolometers of FIRAS revolutionized the field, making obsolete most other high-frequency measurements of the CMB radiation spectrum, they did not observe the low-frequency range of the spectrum. Therefore, it is important that some groups are pur-

Fig. 4.2 The first FIRAS result (Mather et al. 1990). The small squares show measurements with a conservative error estimate of 1%. The full line is a fit to the black-body form

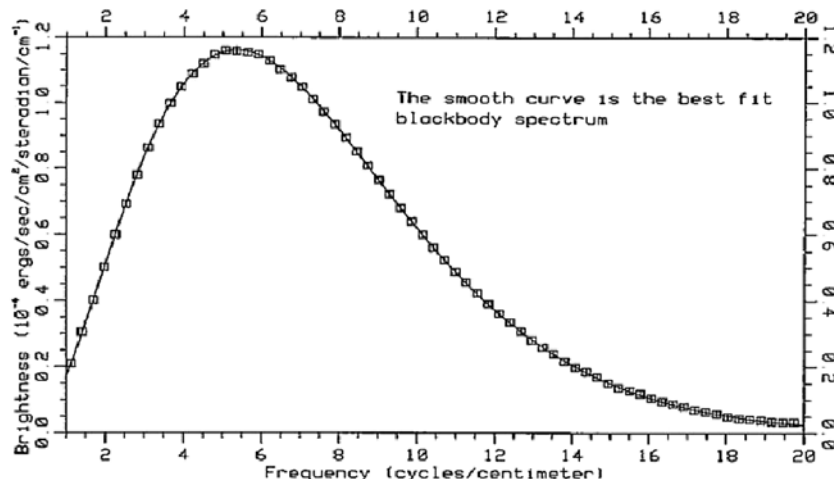


Fig. 4.3 Results from FIRAS published by Mather et al. in 1994. Data points show deviations from the black-body spectrum with the temperature 2.727 K (the final result for the temperature is 2.725 ± 0.002 K). The largest deviations were 0.03 percent of the maximum radiation; see Mather et al. [120]

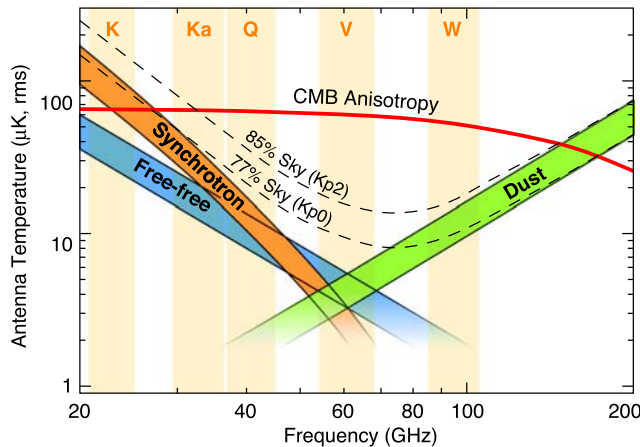
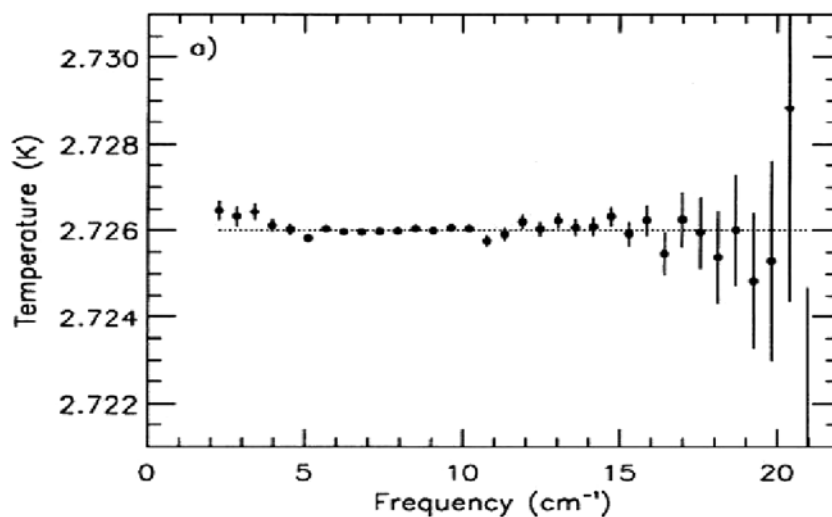


Fig. 4.4 Overview of the foreground spectra: the WMAP frequency bands were chosen to be in a spectral region where the CMB anisotropy (see Sect. 8) is dominant over the competing galactic and extragalactic foreground emissions (curves from <http://lambda.gsfc.nasa.gov/product/foreground>)

ing long-wavelength measurements of the spectrum. Moreover, as we shall see below, some of the spectral distortions we are looking for are more visible on the Rayleigh–Jeans side of the spectrum.

Finally, the FIRAS Team gave us, with the above black-body spectrum and its temperature, two upper limits on possible spectral distortions. But, now, let us discuss the various processes which could occur in the early universe and which could contribute to these different possible spectral distortions.

4.3 Thermalization

The CMB exhibits a perfect black-body shape to the precision of current measurements. The question arises: how did the black-body form and how was it maintained? In the

early universe, a delicate interplay between radiation and matter took place. Moreover, any energy released into the primordial plasma could generate spectral distortions in the cosmic background radiation and, at present, signatures of these early epochs.

The main physical processes which were important for thermalizing the CMB spectrum in the early universe were Compton scattering:

$$e^- + \gamma \rightleftharpoons e^- + \gamma, \quad (4.13)$$

bremsstrahlung, also called free–free emission:

$$e^- + X \rightleftharpoons e^- + X + \gamma, \quad (4.14)$$

where X is an ion, and double-Compton scattering:

$$e^- + \gamma \rightleftharpoons e^- + \gamma + \gamma. \quad (4.15)$$

Their joined action changes the photon occupation number $\eta(v, t)$ with time [123]:

$$\frac{\partial \eta}{\partial t} = \left. \frac{\partial \eta}{\partial t} \right|_C + \left. \frac{\partial \eta}{\partial t} \right|_B + \left. \frac{\partial \eta}{\partial t} \right|_{DC}. \quad (4.16)$$

Kompaneets [132] solved the general problem for the Compton scattering passing from the collisional integral equation to a very simple kinetic equation, which reads

$$\frac{\partial \eta}{\partial t} \Big|_C = \frac{1}{t_C} \frac{1}{x_e^2} \frac{\partial}{\partial t} \left[x_e^4 \frac{\partial \eta}{\partial x_e} + \eta + \eta^2 \right], \quad (4.17)$$

where $x_e = h_P v / (k_B T_e)$ is a dimensionless frequency; T_e is the electron temperature. The characteristic time t_C is given by

$$t_C \sim \frac{10^{28}}{\Omega_b h^2} \frac{2.725 \text{ K}}{T_0} \frac{T_r}{T_e} (1+z)^{-4} \text{ s}, \quad (4.18)$$

where $T_r = T_0(1+z)$ is the radiation temperature; the ratio T_e/T_r plays an important role only in cases where the electron temperature is not tightly coupled to the photon temperature.

Note that many authors have studied the problem for the three processes; in particular, Danese and De Zotti [123, 130, 131], Sunyaev and Zel'dovich [122], Burigana et al. [133, 134], Salati [41, 124], Hu and Silk [137], Danese and Burigana [135].

The bremsstrahlung term $\partial\eta/\partial t|_B$ is given by

$$\frac{\partial\eta}{\partial t}\Big|_B = \frac{1}{t_B} g_B(x_e) e^{-x_e} \frac{1}{x_e^3} [1 - \eta(e^{x_e} - 1)]; \quad (4.19)$$

a quite similar expression holds for the double-Compton scattering term $\partial\eta/\partial t|_{DC}$:

$$\frac{\partial\eta}{\partial t}\Big|_{DC} = \frac{1}{t_{DC}} g_{DC}(x_e) e^{-x_e} \frac{1}{x_e^3} [1 - \eta(e^{x_e} - 1)], \quad (4.20)$$

where $g_B(x_e)$ and $g_{DC}(x_e)$ are the Gaunt factors of bremsstrahlung and double Compton respectively, see for instance [135].

In terms of cosmological parameters the characteristic times during which the bremsstrahlung t_B and double Compton t_{DC} are able to change the occupation number are given by

$$t_B \sim \frac{10^{23}}{\Omega_b^2 h^4} \left(\frac{T_0}{2.725 \text{ K}} \right)^{7/2} \left(\frac{T_e}{T_r} \right)^{7/2} (1+z)^{-5/2} \text{ s}, \quad (4.21)$$

$$t_{DC} \sim \frac{10^{39}}{\Omega_b h^2} \left(\frac{2.725 \text{ K}}{T_0} \right)^2 \left(\frac{T_r}{T_e} \right)^2 (1+z)^{-5} \text{ s}. \quad (4.22)$$

Salati [124] has studied the typical time scales of these processes: t_C , t_B , t_D as a function of the redshift and has compared them to the age of the universe t_U in the case of an $\Omega = 1$ universe.

4.4 Spectral distortions of CMB radiation

Coupling between radiation and matter can lead to observable distortions of the CMB. If a significant amount of energy is injected to matter by some process, the coupling will transfer part of this energy into the CMB. From the study of Salati [124], one can show that three possibilities occur, depending on when the energy is released into the primordial plasma.

- $z \geq z_{PI}$.

In this case the age of the universe t_U exceeded both t_C and t_{DC} . Double-Compton emission acted efficiently, and any spectral distortion was erased during an expansion time. No matter how large the energy release was, the microwave background is not affected. One can note that for $z \geq z_{PI}$, the CMB radiation spectrum is not telling much about the

energetics of the universe. However, one can use big-bang nucleosynthesis to probe the total energy of the universe up to $z \sim 10^{10}$ (when the universe was 100 s old).

- $z_{BE} < z < z_{PI}$.

The age of the universe t_U was still larger than the Comptonization time scale t_C , so that thermalization of the photon gas ensued. However, there is no production of additional photons because the double-Compton time scale t_{DC} exceeded t_U . Any energy release generated a μ -distortion, since the radiation spectrum relaxed towards a Bose–Einstein distribution faster than the universe expanded ($t_C < t_U$).

However, pure black-body radiation could not be achieved, since double-Compton emission was slower than expansion ($t_{DC} > t_U$). The photon bath was still in thermal equilibrium, but with an average photon energy larger than for a Planck spectrum, i.e. with a non-zero chemical potential μ . From the Bose–Einstein distribution, we have

$$\eta_\gamma^{\text{BE}} = \frac{1}{\exp(h_P v / k_B T_e - \mu / k_B T_e) - 1}. \quad (4.23)$$

If $\Delta\rho_\gamma$ denotes the increase of the energy density due to an energy injection, one may express the chemical potential μ as a function of the relative increase of the photon energy by

$$\frac{\Delta\rho_\gamma}{\rho_\gamma} \sim 0.714\mu. \quad (4.24)$$

- $z_{\text{rec}} \sim 10^3 < z < z_{BE}$.

Both t_{DC} and t_C exceeded the expansion time. Photons may still collide with electrons, and y -distortions may result if the Compton parameter y is small; $y = t_U/t_C$. If energy is released in the primordial plasma, the Rayleigh–Jeans region of the spectrum is slightly depleted by a factor $\exp(-2y)$, while a rapid rise in the temperature in the Wien region occurred. The magnitude of the distortion is related to the energy transfer $\Delta\rho_\gamma$ by

$$\frac{\Delta\rho_\gamma}{\rho_\gamma} \sim 4y. \quad (4.25)$$

Therefore, one can say that the thermalization redshift is approximately given by $z_{PI} \sim 10^7$. Any energy deposition at a later time, i.e. for $z \leq z_{PI} \sim 10^7$, $T < 10 \text{ keV}$ or $t > t_{PI} \sim 10^5 \text{ s}$ will leave a potentially observable distortion in the CMB spectrum:

- a μ -distortion for an early energy release: $z \sim 10^7$ – 10^5 with a possible drop in brightness temperature at centimeter wavelengths;
- a y -distortion for a late energy release: $z \sim 10^5$ – 10^3 with a decrease in temperature on the Rayleigh–Jeans side of the spectrum and a rise in temperature on the Wien side of the spectrum, i.e. a shift of photons from low to high frequencies. Therefore, precision measurements of the CMB

spectrum probe the thermal history of the universe back to this epoch.

At present the definitive limits on both y and μ come from the FIRAS instrument aboard COBE. The 95% limits are [119]:

$$y \leq 1.5 \times 10^{-5}, \quad (4.26)$$

$$\mu \leq 9 \times 10^{-5}. \quad (4.27)$$

Therefore, the limit on energy release corresponding to a y -distortion for a late energy release ($z \sim 10^5\text{--}10^3$) is

$$\frac{\Delta\rho_\gamma}{\rho_\gamma} \leq 6 \times 10^{-5}, \quad (4.28)$$

and the limit on energy release corresponding to a μ -distortion for an early energy release ($z \sim 10^7\text{--}10^5$) is

$$\frac{\Delta\rho_\gamma}{\rho_\gamma} \leq 6.6 \times 10^{-5}. \quad (4.29)$$

Finally, from these limits on the energy release as a function of the redshift, one can induce limits on various processes which possibly took place in the early universe. We just mention:

- particle decays [124, 125];
- gravitational energy from large-scale structures [126, 127];
- primordial black-hole evaporation;
- superconducting cosmic strings and explosive formation [128, 129];
- variations of fundamental constants.

5 Cosmological recombination

In the hot big-bang picture, after the nucleosynthesis period a natural question concerns the possibility to form atoms by recombination of a primordial nucleus with free electrons, and a second question concerns the degree to which the recombination is inhibited by the presence of recombination radiation.

The reason why these questions are central were mentioned by Peebles [138] and Peebles and Dicke [139], based, at this epoch, on the *primeval-fireball* picture of Gamow [87] for the evolution of the universe.

The cosmological recombination process was not instantaneous, because the electrons, captured into different atomic energy levels, could not cascade instantaneously down to the ground state. Atoms reached the ground state either through the cosmological redshifting of the Lyman α line photons or by the $2s\text{--}1s$ two-photon process. Nevertheless the universe expanded and cooled faster than recombination could be completed, and a small fraction of free electrons and protons remained.

5.1 Recombination of hydrogen and deuterium

Peebles [138] was the first to present a theory in which the very complicated recombination process is reduced to simpler terms. The methodology of the calculations consists in taking into account a three-level atom with a ground state, a first excited state and a continuum, represented by a recombination coefficient. A single ordinary differential equation is derived to describe the ionization fraction. The assumptions are as follows.

- Hydrogen excited states are in equilibrium with the radiation.
- Stimulated de-excitation is negligible.
- Collisional processes are negligible.

The approximations are based on the rate of transfer of energy per unit volume between radiation and free electrons, developed by Kompaneets [132] and next by Weymann [140, 141] and finally coupled with the expansion of the universe.

One of the key points is to estimate the photorecombination rate R_{ci} directly to each level for multilevel H and D:

$$R_{ci} = 4\pi \int_{v_0}^{\infty} \frac{\sigma_{ic}(v)}{h_P v} I(v, T_r) dv. \quad (5.1)$$

Here i refers to the i th excited state and c refers to the continuum; v_0 is the threshold frequency for ionization from the i th excited state. The radiation field $I(v, T_r)$, the Planck function, depends on the frequency v and time t ; see (4.7).

By using the principle of detailed balance in the case of local thermodynamical equilibrium (LTE), the radiative recombination rate can be calculated from the photoionization rate. Moreover, radiative recombination includes spontaneous and stimulated recombination.

Spontaneous recombination involves a free electron, but its calculation requires no knowledge of the local radiation field, because the energy of the photon is derived from the electron's kinetic energy [27]. The correction for stimulated recombination depends on T_m , because the recombination process is collisional. Thus the form of the total photoionization rate is

$$\sum_{i>1}^N n_i R_{ci} = \sum_{i>1}^N n_i 4\pi \int_{v_0}^{\infty} \frac{\sigma_{ic}(v)}{h_P v} I(v, T_r) dv, \quad (5.2)$$

and the total recombination rate is

$$\begin{aligned} \sum_{i>1}^N n_e n_c R_{ci} &= n_e n_i \sum_{i>1}^N \left(\frac{n_i}{n_e n_c} \right)^{\text{LTE}} \\ &\quad \times 4\pi \int_{v_0}^{\infty} \frac{\sigma_{ic}(v)}{h_P v} \left(\frac{2h_P v^3}{c^2} + I(v, T_r) \right) \\ &\quad \times \exp\left(-\frac{h_P v}{k_B T_m}\right) dv. \end{aligned} \quad (5.3)$$

5.2 Recombination of helium

The ${}^4\text{He}$ nucleus is the second most abundant nuclei in the primordial universe after the hydrogen nucleus. The conditions for the helium recombination are such that in both cases it occurs in accordance with the Saha equation [142, 143]. The recombination history of the early universe consists of three stages, but helium recombination occurs in two steps.

- at $z \sim 6000$ (or when the temperature became less than 16 000 K) the first electron recombines in order to form the singly ionized HeII from doubly ionized HeIII.
- Then at $z \sim 2700$ (or temperature close to 7 300 K), HeII recombines into a neutral state.
- from $z \sim 1500$ recombination of hydrogen took place.

Seager et al. [27] and then Dubrovich and Grachev [144] have developed an improved recombination calculation of H, He (with HeII and HeIII) that involves a line-by-line treatment of each atomic level. They found that HeI recombination is much slower than previously thought, and it is delayed until just before H recombines.

5.3 Recombination of lithium

The ionization potential $I_{\text{Li}} = 5.392$ eV of LiI is lower than that of hydrogen ($I_{\text{H}} = 13.6$ eV). Stancil et al. [149] suggested the existence of Li^+ ions after the period of the hydrogen recombination and showed that radiative recombination is again effective at the redshift $z \sim 450$. This last point is particularly important for lithium chemistry as we shall see.

6 Standard chemistry

The studies on the primordial chemistry (or postrecombination chemistry) have been the source of a tremendous increase of the literature. The first chemical network study including the primordial molecules (such as H_2 , HD and LiH) and ions was carried out by Lepp and Shull [145], Latter and Black [146], Puy et al. [147], Galli and Palla [148], Stancil et al. [149], Lepp et al. [150], Pfenniger and Puy [151], and more recently Puy and Pfenniger [152].

After hydrogen recombination, the ongoing physical reactions are numerous, partly due to the presence of the cosmic microwave background radiation. Three classes of reactions are established.

- Collisional $\xi + \xi' \longleftrightarrow \xi_1 + \xi_2$ association, associative detachment, mutual neutralization, charge exchange, and reverse reactions.
- Electronic $\xi + e^- \longleftrightarrow \xi_1 + \xi_2$ recombination, radiative attachment, dissociative attachment.

- Photoprocesses $\xi + \gamma \longleftrightarrow \xi_1 + \xi_2$ dissociation, detachment, ionization, radiative association.

The chemical kinetics of a reactant ξ , which leads to the products ξ_1 and ξ_2 , imposes the following evolution of the *mean numerical density* \bar{n}_ξ :

$$\left(\frac{d\bar{n}_\xi}{dt} \right)_{\text{chem}} = \sum_{\xi_1 \xi_2} k_{\xi_1 \xi_2} \bar{n}_{\xi_1} \bar{n}_{\xi_2} - \sum_{\xi'} k_{\xi \xi'} \bar{n}_\xi \bar{n}_{\xi'}, \quad (6.1)$$

where $k_{\xi_1 \xi_2}$ is the reaction rate of the ξ -formation process from ξ_1 and ξ_2 , and $k_{\xi \xi'}$ is the reaction rate of ξ -destruction by collision with the reactant ξ' . The typical rate of the collisional reactions, k_{coll} (in $\text{cm}^3 \text{s}^{-1}$), is calculated by averaging the cross sections, $\sigma(E)$, over a Maxwellian velocity distribution at temperature T_m :

$$k_{\text{coll}} = \sqrt{\frac{8}{\pi m_r (k_B T_m)^3}} \int_0^\infty \sigma(E) e^{-E/k_B T_m} E \, dE, \quad (6.2)$$

where E is the collision energy, m_r the reduced mass of the collisional system (ξ, ξ'), and T_m is the temperature of the matter. The radiative rate coefficient k_{rad} (in s^{-1}), which depends on the radiative cross section σ_{rad} , and on the CMB radiation, is defined by

$$k_{\text{rad}} = \frac{8\pi}{c^2} \int_{\nu_{\text{th}}}^\infty \frac{\sigma_{\text{rad}}(\nu) \nu^2 \, d\nu}{\exp(h_P \nu / k_B T_r) - 1}, \quad (6.3)$$

where ν_{th} is the threshold frequency above which the radiative process is possible, and T_r is the radiation temperature. As usual, c is the speed of light and h_P the Planck constant.

6.1 Helium chemistry

Helium chemistry plays an important role for the primordial chemistry because He is the first neutral atom which appeared in the universe. Once neutral He is significantly abundant, charged transfer with ions is possible, allowing for the formation of other neutral species. Thus HeH^+ is the first stable molecular bond formed in the radiative processes [153]:



The dominant destruction process at low redshifts is charge exchange via



which yields chemical equilibrium. However, knowledge of helium chemistry is still incomplete. For example, no information is yet available concerning HeD^+ [150].

6.2 Hydrogen chemistry

In the absence of solid surfaces, such as dust grains, it is possible to form neutral molecules through the radiative association between two neutral atoms. Molecular hydrogen cannot form easily by this radiative process, because H_2 does not have a permanent dipole moment.

Thus, any H_2 formed in the uniform background is dissociated by the radiation, until the density is too low to produce it. Nevertheless, once HeH^+ appears, it becomes an important source of H_2^+ through the exchange reaction with some neutral H, as we have mentioned in the preceding section. Charge transfer from H_2^+ becomes the most likely alternative to form H_2 . Saslaw and Zipoy [154] and then Shchekinov and Enté [155] showed the importance of the charge-transfer reactions:



initiated by the radiation association



They pointed out that the H_2^+ ion is converted to H_2 as soon as it is formed, and the H_2^+ concentration never becomes large.

Moreover, as the radiation temperature decreases, H_2 can be formed through H^- by radiative attachment. Peebles [138], in a scenario concerning the origin of globular star clusters, showed that these clusters may have originated as gravitationally bound gas clouds before the galaxies formed and suggested that some molecular hydrogen could be formed inside them, mainly by way of negative hydrogen by the reactions such as [155, 156])



followed by the associative detachment



The photodetachment of H^- and the photodissociation of H_2^+ by the background radiation field restrict the abundance of molecular hydrogen formed at the early stages, although the photodestruction of molecular hydrogen is negligible. The destruction is due to collisional dissociation. We notice that H_3^+ reactions, which are pivotal to the chemistry of dense interstellar clouds [157–159] do not play an important role in primordial chemistry.

6.3 Deuterium chemistry

HD forms in ways similar to H_2 ,



Deuterated-hydrogen molecules do have permanent dipole moments, which lead to the capacity to be formed by radiative association (forbidden between two hydrogen atoms):



Nevertheless, HD formation is very significant when H_2 appears, the mechanism of dissociative collision



Thus the formation of HD is carried out in two steps.

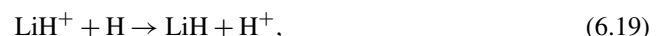
Nevertheless, when the abundance of H_2 is sufficient, the second way of formation is dominant (i.e. H^- way); see the work of Stancil et al. [149], who presented a complete review of the deuterium chemistry of the early universe.

6.4 Lithium chemistry

The lithium chemistry received large attention by the cosmochemistry community. Precise investigations of the chemical network were developed by [160] and [161]. Besides the classical radiative association, LiH can be formed by different exchange reactions. The lithium chemistry is initiated by the recombination of lithium, which occurred near the redshift $z \sim 450$. The formation of the molecular ion LiH^+ , formed by radiative association processes,



opens the way of the formation of the LiH molecules through the exchange reactions:



which are more rapid than the formation by radiative association of H and Li atoms. Despite the radiative association from electronically excited lithium atoms, tentatively proposed by [162–164], the LiH abundance remains low.

6.5 Equations of evolution

All the rates of recombination and chemical reactions depend on the electron density n_e , the matter and radiation temperatures and the baryon density. Thus, it is necessary to take into account the dynamical and thermal equations of evolution.

6.5.1 Evolution of matter and radiation temperature

The matter temperature is affected by the Compton cooling (which is the major source of energy transfer between electrons and photons), adiabatic cooling (due to the expansion of the universe).

The first law of thermodynamics imposes

$$\frac{d}{dt}[\varepsilon_{\text{tot}} V] = -p_{\text{tot}} \frac{dV}{dt} + \Gamma_{\text{com}} V, \quad (6.20)$$

p_{tot} is the total pressure, which depends on p_r (radiative pressure) and p_m (baryonic gas pressure):

$$p_{\text{tot}} = p_r + p_m = \frac{a_r T_r^4}{3} (1 + f_v) + \bar{n}_b k_B T_m, \quad (6.21)$$

where f_v is the neutrino contribution to the radiation density for three massless, non-degenerate, neutrino flavors given by

$$f_v = 3 \frac{7}{8} \left(\frac{4}{11} \right)^{4/3}. \quad (6.22)$$

Γ_{com} is the energy transfer from the radiation to matter via Compton scattering of CMB radiation on free electrons [26, 140], given by

$$\Gamma_{\text{com}} = 4 \bar{n}_e \sigma_T a_r k_B T_r^4 \frac{T_r - T_m}{m_e c}, \quad (6.23)$$

and σ_T defines the Thomson cross section, m_e the electron mass and, finally, \bar{n}_e the mean numerical density of the electron.

Note that in the external heating and cooling contribution, the sum of enthalpy reaction and energy transfer (via excitation and de-excitation of the molecular transition) are negligible [147, 148, 150] (but this is not the case in the collapse of molecular protoclusters).

Thus, in a comoving frame the evolution of the baryon temperature T_m is given by the expression

$$\frac{dT_m}{dt} = -2H(t)T_m + \frac{8}{3} \frac{\sigma_T a_r}{m_e c} T_r^4 (T_r - T_m) x_e, \quad (6.24)$$

where $H(t)$ is the Hubble parameter, $x_e = \bar{n}_e / \bar{n}_b$ characterizes the ionization fraction (i.e., the electronic abundance).

This equation is coupled with the radiation temperature evolution and the time-redshift relation:

$$\frac{dT_r}{dt} = -H(t)T_r. \quad (6.25)$$

6.5.2 Evolution of the baryon density

The numerical mean baryon density, \bar{n}_b , is expressed by

$$\bar{n}_b = \sum_{\xi} \bar{n}_{\xi} = \frac{\sum_{\xi} N_{\xi}}{V}, \quad (6.26)$$

where N_{ξ} is the number of species ξ , and V is a comoving volume proportional to the scale factor cubed, $V \propto a^3$. Thus the mean numerical density evolution is given by

$$\frac{d\bar{n}_b}{dt} = -3H\bar{n}_b + \sum_{\xi} \left(\frac{d\bar{n}_{\xi}}{dt} \right)_{\text{chem}}. \quad (6.27)$$

The last term of the second member of this equation represents the variation of the number of particles due to chemistry.

Moreover, for each chemical species ξ we have

$$\frac{d\bar{n}_{\xi}}{dt} = -3H(t)\bar{n}_{\xi} + \left(\frac{d\bar{n}_{\xi}}{dt} \right)_{\text{chem}}, \quad (6.28)$$

where \bar{n}_{ξ} is the numerical density of ξ . The last term of the second member of this equation expresses the contribution of the chemical kinetics, see (6.1), and H is the Hubble parameter given by (1.2).

6.6 Results of thermochemistry

The set of ordinary differential equations depends on the temperatures (radiation or matter) and the matter density.

We have solved the full equations for the time evolution of the chemical abundance, temperature and baryonic density with the numerical code developed by Puy and Pfenniger [152].

Here we use the chemical network and reaction rates described by the seminal papers of [148] and [165], except for the hydrogen and deuterium recombinations which are calculated from the reaction rates given by [166] from numerical approximations.

6.6.1 Cosmological recombination

Various approaches exist to the calculation of the time evolution of the electronic fraction during the cosmological recombination; see the exhaustive work of Schleicher et al. [167].

In our case, in order to illustrate the mechanism of cosmological evolution, the value of the rate of radiative transition from the continuum to the excited states is the simple power-law fit given by [166].

The results are shown in Fig. 6.1, separately for each atomic element (i.e. H, He, D and Li). We introduce the redshift of the recombination z_{rec} by the epoch when the abundance of a species equals the one of its corresponding ion. Thus, we obtain the successive redshifts of HeII, HeI, DI and HI recombination (see Fig. 6.1):

- $z_{\text{rec,He}^+} \approx 6101$,
- $z_{\text{rec,He}} \approx 2604$,
- $z_{\text{rec,D}} = z_{\text{rec,H}} \approx 1425$.

Fig. 6.1 Successive cosmological recombination versus redshift. The helium and hydrogen recombination are plotted on the *right panel*, while the deuterium and lithium recombination are indicated on the *left panel*. The ordinates represent the relative abundances, calculations from the numerical code developed by Puy and Pfenniger [152]

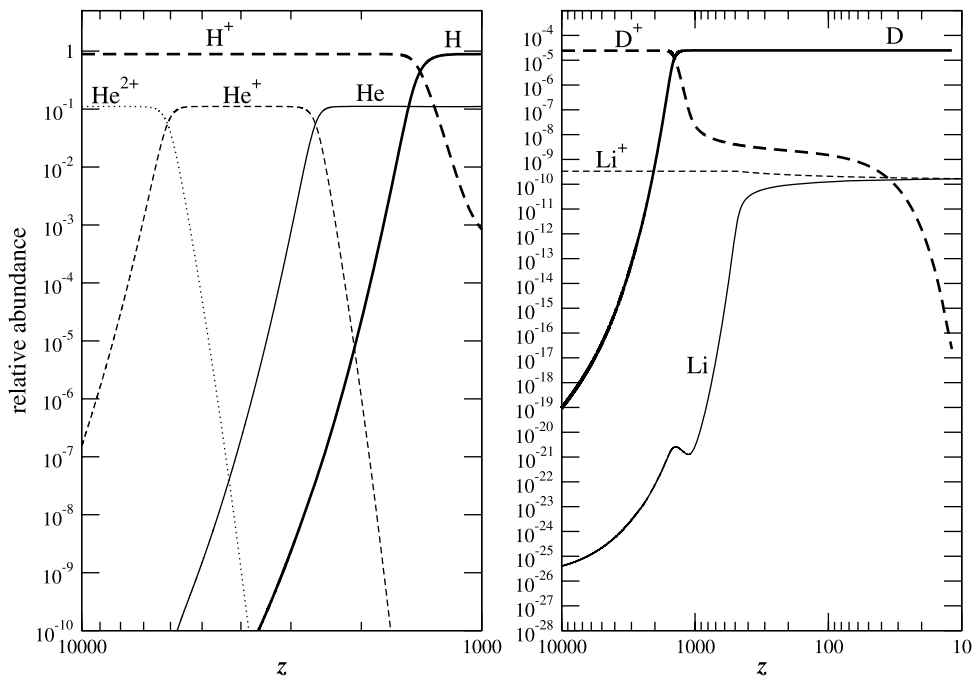
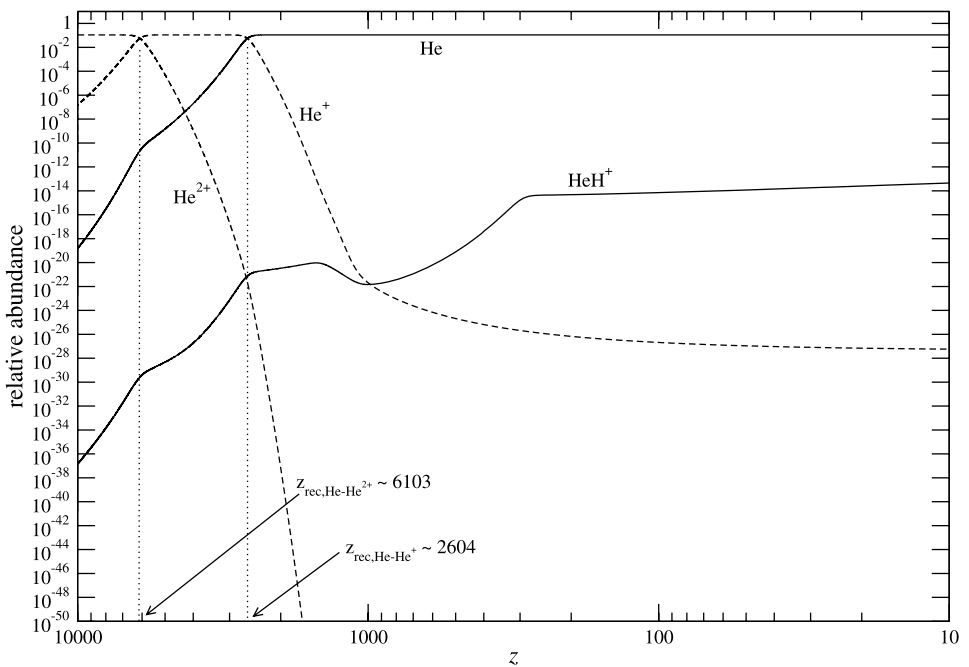


Fig. 6.2 Evolution of the chemical abundances of helium components. The redshift of the successive helium recombination are indicated. The ordinates represent the relative abundances, calculations from the numerical code developed by Puy and Pfenniger [152]



Let us notice that the ionization energy of neutral lithium amounts to $I_{Li} \sim 5.39$ eV, at the lowest ground-state configuration. Despite the more abundant electrons after hydrogen recombination (a few times 10^{-4} , while Li^+ reaches a few times 10^{-10}), Li might be the last element that we consider to recombine. However, the charge transfer ($Li-H^+$) and (Li^+-H) remains active. For these reasons Li does not recombine totally, and neutral and ionized Li tend to match their abundances.

We find that the residual ionization fraction x_e is close to 5.78×10^{-5} . The reduced number of free electrons and

protons are going to have a direct effect on the chemical evolution of the gas.

6.6.2 Helium chemistry

The main molecular species containing helium is HeH^+ , formed, as we have seen, by the radiative association processes; see Fig. 6.2. As Galli and Palla [148] mentioned, the HeH^+ ions are removed by the CMB photons at $z < 250$ also by collisions with H atoms. This process explains the

abrupt change in the slope of the curve of HeH^+ , as shown in Fig. 6.2.

At the redshift $z_f = 10$ we find the *frozen* abundances:

- $[\text{He}] = 0.111$,
- $[\text{He}^+] = 6.41 \times 10^{-28}$,
- $[\text{He}^{++}] = 6.86 \times 10^{-96}$,
- $[\text{HeH}^+] = 4.6 \times 10^{-14}$.

6.6.3 Hydrogen chemistry

Figure 6.3 illustrates the evolution of the hydrogen species. We see that the formation of H_2^+ is controlled by radiative association and photodissociation at $z > 100$. At high redshift, the formation of this ion is regulated by the destruction of HeH^+ .

The steady drop of H^- is determined by the mutual neutralization with H^+ at $z < 100$.

Thus, the two major routes of H_2 formation are relative to the two jumps at the redshifts $z \sim 500$ (via the H_2^+ channel) and $z \sim 150$ (via H^- channel).

At the redshift $z_f = 10$ we find the hydrogen abundances

- $[\text{H}] = 0.889$,
- $[\text{H}^+] = 5.78 \times 10^{-5}$,
- $[\text{H}^-] = 7.34 \times 10^{-14}$,
- $[\text{H}_2^+] = 6.63 \times 10^{-14}$,
- $[\text{H}_3^+] = 3.55 \times 10^{-17}$,
- $[\text{H}_2] = 1.13 \times 10^{-6}$.

Fig. 6.3 Evolution of the chemical abundances of hydrogen components. The redshift of the hydrogen recombination is indicated. The ordinates represent the relative abundances, calculations from the numerical code developed by Puy and Pfenniger [152]

6.6.4 Deuterium chemistry

Figure 6.4 shows the evolution of deuterium chemistry. We remark that the only molecule formed in significant amounts is HD , whose evolution with redshift follows closely that of H_2 . A complete description of the abundance evolution is found in the paper of Galli and Palla [148].

The final deuterium abundances are, at the redshift $z_f = 10$,

- $[\text{D}] = 2.436 \times 10^{-5}$,
- $[\text{D}^+] = 2.1 \times 10^{-19}$,
- $[\text{HD}^+] = 5.31 \times 10^{-20}$,
- $[\text{H}_2\text{D}^+] = 2.33 \times 10^{-19}$,
- $[\text{HD}] = 3.67 \times 10^{-10}$.

6.6.5 Lithium chemistry

The abundances of lithium chemistry are very low as we see in Fig. 6.5. The more abundant complexes are LiH and LiH^+ , whose formation is sensibly controlled by the radiative association of Li^+ and H (see [160] and [148] for an exhaustive description).

The final deuterium abundances are, at the redshift $z_f = 10$,

- $[\text{Li}] = 1.668 \times 10^{-10}$,
- $[\text{Li}^+] = 1.675 \times 10^{-10}$,
- $[\text{Li}^-] = 1.25 \times 10^{-21}$,
- $[\text{LiH}^+] = 1.26 \times 10^{-18}$,
- $[\text{LiH}] = 2.53 \times 10^{-20}$.

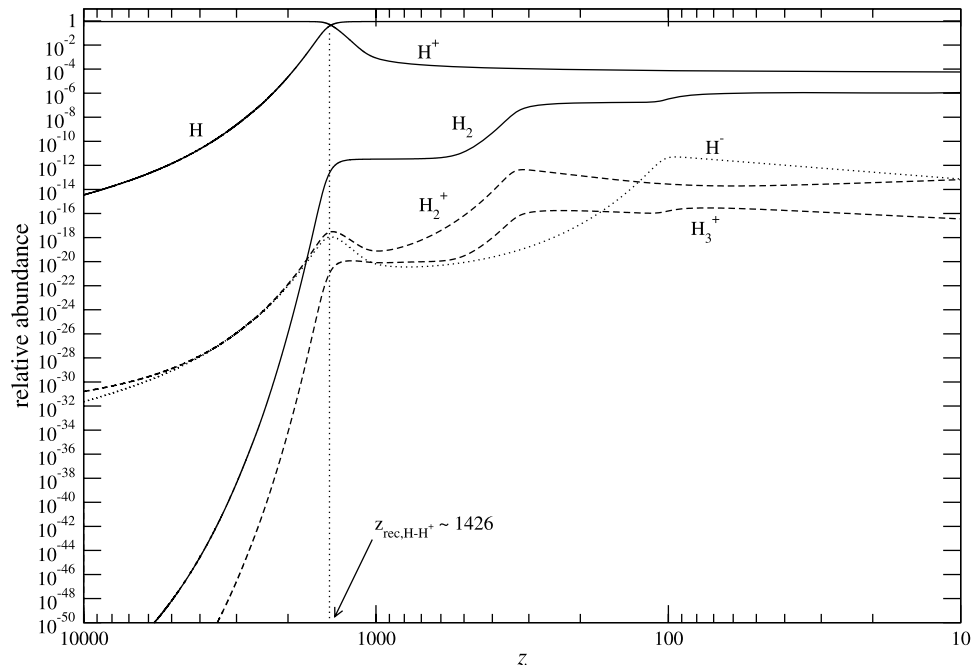


Fig. 6.4 Evolution of the chemical abundances of the deuterium components. The redshift of the deuterium recombination is indicated. The ordinates represent the relative abundances, calculations from the numerical code developed by Puy and Pfenniger [152]

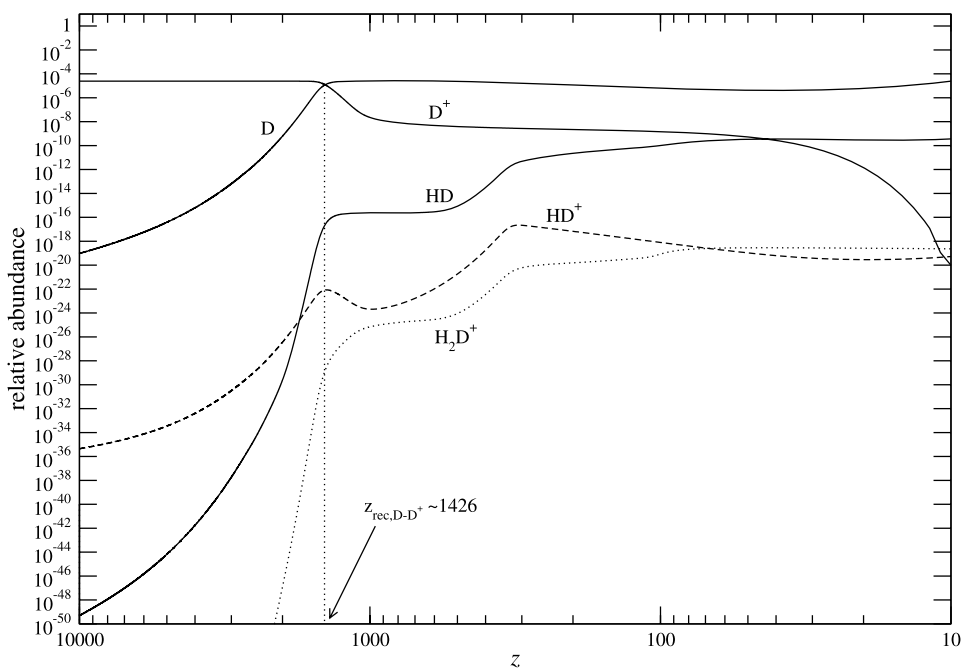
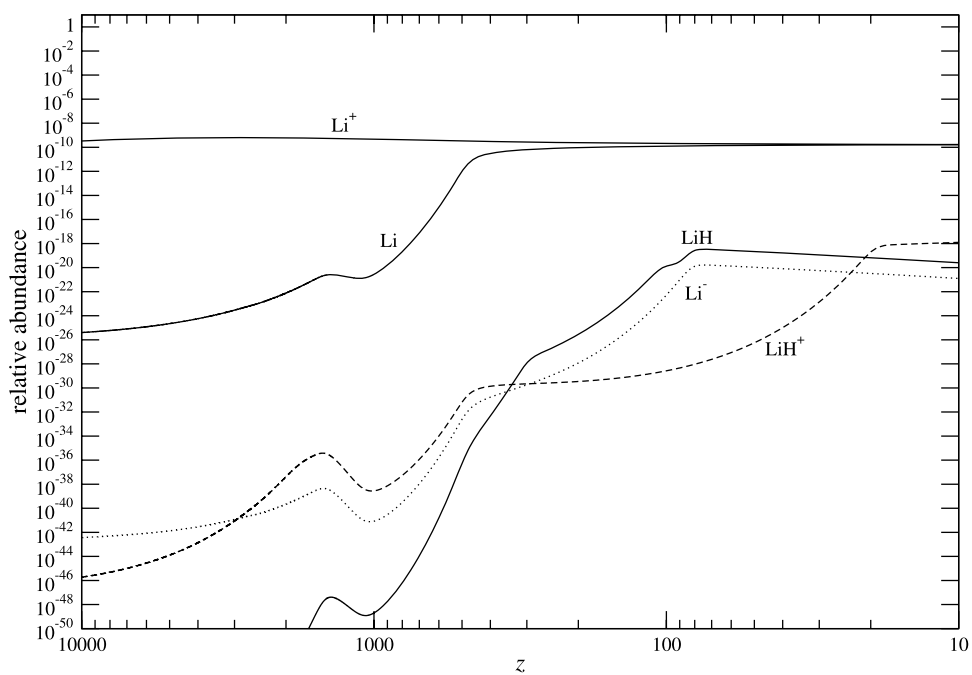


Fig. 6.5 Evolution of the chemical abundances of lithium components. The ordinates represent the relative abundances, calculations from the numerical code developed by Puy and Pfenniger [152]



6.6.6 Thermal decoupling

Due to the decreasing of the ionized fraction, Thomson scattering becomes more and more inefficient during the evolution of the universe. Actually the temperature of matter (i.e. without radiation coupling) evolves as $(1+z)^2$ when the radiation temperature evolves as $1+z$. We can define an ef-

fective redshift of decoupling $z_{\text{dec,eff}}$ by *last epoch* when the radiation and matter temperatures are equal:

$$T_r(z_{\text{dec,eff}}) = T_m(z_{\text{dec,eff}}). \quad (6.29)$$

Moreover, we define the decoupling redshift $z_{\text{dec,1\%}}$, for which the matter temperature is equal to 1% of the radiation temperature.

Fig. 6.6 Thermal decoupling between radiation and matter in the standard big-bang chemistry model. T_r (dashed line) represents the temperature of radiation, T_m (bold line) is the temperature of matter. $T_{m,s}$ (thin line) is the standard matter evolution, where $T_{m,0} = T_{r,0}/(1 + z_{dec,eff})$. $z_{dec,\xi}$ is respectively the redshift of recombination for He^+ , He, H and D. $z_{dec,1\%}$ is the decoupling redshift for which the matter temperature is equal to 1% of the radiation temperature; figures from Puy and Pfenniger [152]

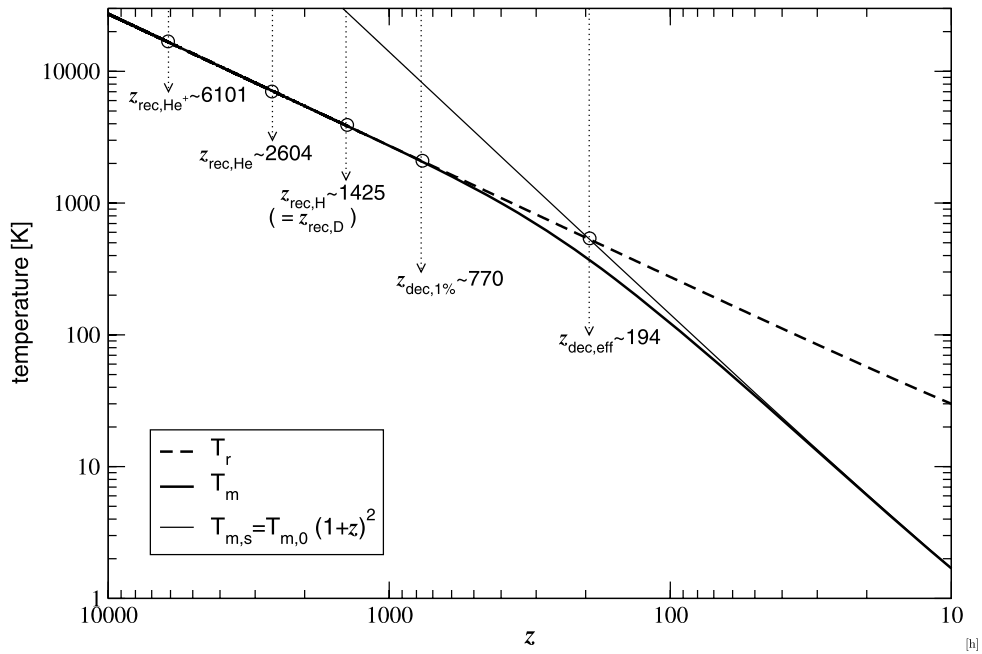


Figure 6.6 represents the evolution of matter and radiation. We see that the two epochs, $z_{dec,eff}$ and $z_{dec,1\%}$, are

$$z_{dec,eff} \sim 194 \quad \text{when } z_{dec,1\%} \sim 770, \quad (6.30)$$

which differ from the common approximation $z_{dec} \sim 1500$. Generally there is a strong confusion between the redshift of hydrogen recombination—we have seen $z_{rec,H} \sim 1425$ —and this redshift of thermal decoupling.

Let us notice that at the redshift $z_{dec,1\%} \sim 770$, matter is again strongly thermally coupled with the radiation. This is, in part, the reason that the formation of the first objects will be later.

7 The CMB dipole anisotropy

As already said in Sect. 1, the photons in the universe decoupled from matter at $T \sim 3000$ K or $z \sim 1000$. These photons have been propagating freely in space-time since then and can be detected today.

In an ideal Friedmann universe, a comoving observer will see these photons as a black-body spectrum at the temperature T_0 . The deviations in the metric from that of the Friedmann universe, the motion of the observer with respect to the comoving frame and any astrophysical process occurring along the trajectory of the photon can lead to effects in this radiation. There are two possible kinds of effects.

- (1) From a particular direction in the sky, the spectrum may not be strictly Planckian with a single temperature T_0 .
- (2) The spectrum, in any direction, may be Planckian, but the temperature may be different in different directions:

$T_0 = T_0(\theta, \phi)$, where θ and ϕ are the angular coordinates on the sky.

In Sect. 4, we have seen that there is no distortion of the first kind in the CMB. In particular, FIRAS aboard COBE gave only upper limits on possible μ - and y -distortions which could establish strong constraints on many cosmological models.

On the contrary, the CMB radiation shows deviations of the second kind at different angular scales generally called anisotropies. These CMB anisotropies are the subject of Sects. 7, 8 and 9.

The most dominant anisotropy in the CMB radiation, which could be interpreted as being due to the motion of our galaxy with respect to the cosmic rest frame, would exhibit a so-called dipole pattern, hotter in our direction of motion and colder in the opposite. Partly following previous discussions [19, 171], we shall present this dipole anisotropy: its prediction, its discovery and measurements and its physical origin.

7.1 The prediction of the dipole anisotropy

7.1.1 The historical problem

The first step towards the study of the dipole anisotropy was done by Hasenöhr [168, 169] and by von Mosengheil [170]. They computed the Doppler signal seen by an observer moving at a constant speed v inside a cavity at a given temperature T on the basis of Galilei and Lorentz transformations, respectively. The radiation emitted by the cavity is that of a black body. The problem is: how it will appear to the moving observer? For von Mosengheil—who was a student of

Max Planck—the proposal of his thesis combined two important discoveries: Planck's formula for a black body and the Lorentz transformations recently introduced by Einstein in his theory of special relativity. After a cumbersome computation, he found the correct result [170]:

$$T_{\text{obs}} = T_{\text{wall}} \sqrt{1 - \frac{v^2}{c^2} [1 - \mathbf{v} \cdot \mathbf{n}/c]^{-1}}, \quad (7.1)$$

where the vector \mathbf{n} gives the direction of observation. In von Mosengheil's time, there was no chance of verifying the solution through an experiment. This result had been forgotten until 1965, when the CMB was discovered.

7.1.2 The present predictions

In the framework of big-bang theory, we are living inside a *cavity* limited by the so-called *last scattering surface* (see Sect. 1), a layer of ionized gas, opaque to electromagnetic radiation.

The only difference with respect to the situation discussed by von Mosengheil is that the large scattering surface is expanding and receding from us, so that the photons of the last scattering surface suffer a substantial reddening, thereby appearing as a black body at about 2.7 K.

One notes that the recession of the large scattering surface is due to the expansion of space and it is not a pure velocity of recession: the proper velocity of the observer adds algebraically to the recession velocity and not through the Lorentz formula of special relativity. Since the earth is moving around the sun, the sun is moving inside the galaxy and the galaxy is expected to move with respect to other galaxies, an earth's observer should detect the effect noted by von Mosengheil, thereby measuring his motion with respect to the last scattering surface. In a first approximation in $\beta = v/c$, the above equation predicts a *dipole pattern* on the sky, i.e.

$$T_{\text{obs}} \sim T_{\text{wall}}(1 + \beta \cos \Theta) \quad \text{with } \beta = v/c, \quad (7.2)$$

where Θ is the angle between the direction of observation and that of the motion.

Later on, at the time of CMB observations, this pattern became known as the *dipole anisotropy*.

In early 1967, with only scarce and marginal data available on the isotropy of CMB—in particular, Partridge and Wilkinson [172] have established an upper limit of about 3 mK to any large-scale component of the CMB anisotropy—Sciama [173] noted: *It should be possible to measure the “absolute” motion of the solar system, that is, its motion relative to the universe as a whole.*

As a consequence, Sciama attempted to derive the motion of the sun versus distant galaxies and added the important note: that *in principle all the galaxies concerned ($z < 0.5$)*

could be moving as a whole with respect to the matter with larger redshifts.

Also in 1967, Rees and Sciama [174], and next Steward and Sciama [175], gave different predictions in approximate agreement with the *possible* detection suggested by Partridge and Wilkinson [172]. Next, all these predictions turned out to be in disagreement with observations, but they confirmed the validity of the cautious comment of Sciama about the possibility of a *bulk* motion. All these publications stimulated the interest of experimentalists toward direct observations of the CMB dipole. Several authors attempted to estimate the sky pattern due to this anisotropy.

In 1968, Heer and Kohl [176] and—in the same volume of Physical Review—Peebles and Wilkinson [177] published the correct result. In particular, they used the following expression:

$$T = T_0(1 + \beta \cos \Theta), \quad (7.3)$$

where T_0 is the mean temperature of the CMB over the sky, $\beta = v/c$ is the velocity of the observer with respect to the LSS at $z \sim 1000$, and Θ is the angle between the direction of observation and that of motion.

Finally, note that the derivation of the dipole formula can be done by briefly considering the distribution function $f(\mathbf{p})$ of particles of momentum \mathbf{p} in the observer's frame (see [178] and all the good textbooks such as [179]). These quantities, $f(\mathbf{p})$ and \mathbf{p} , obey the following relation:

$$f(\mathbf{p}) = f'(\mathbf{p}'), \quad (7.4)$$

where $f'(\mathbf{p}')$ is the distribution function in the LSS frame in which the photon background is isotropic and where \mathbf{p} and \mathbf{p}' are related through the Lorentz transformation:

$$\mathbf{p} = \sqrt{1 - \frac{v^2}{c^2} [1 - \mathbf{v} \cdot \mathbf{n}/c]^{-1}} \mathbf{p}'. \quad (7.5)$$

Applying these equations to a black body, one finds

$$T(\mathbf{n}) = \sqrt{1 - \frac{v^2}{c^2} [1 - \mathbf{v} \cdot \mathbf{n}/c]^{-1}} T'. \quad (7.6)$$

Introducing Θ as the angle between the direction of motion and that of observation:

$$T(\Theta) = \sqrt{1 - \beta^2} [1 - \beta \cos \Theta]^{-1} T'. \quad (7.7)$$

This is the formula derived by von Mosengheil [170], Peebles and Wilkinson [177], Heer and Kohl [176].

7.2 The observation of the dipole anisotropy

First of all, we have to recall the observations of Bracewell and Conklin [180] spanning from 1967 to 1969 [181, 182].

They were carried out from the ground with a radiometer, working at 8 GHz and pointing at a constant declination with a peak at 13 h RA (right ascension). Galactic contamination was rather severe. These observations are described in the PhD thesis work of Conklin (performed at Stanford University, 1969). Later, during a IAU Symposium, Conklin reported more data, claimed dipole detection, estimating an amplitude of

$$\Delta T \sim 2.28 \pm 0.92 \text{ mK}, \quad (7.8)$$

with the peak at 10 h 58' RA [183]. The declination of the dipole peak was first measured by Henry [184] for his PhD thesis work (Princeton University, 1971). Henry and Wilkinson used a balloon-borne radiometer at 10–15 GHz. They found

$$\Delta T = 3.2 \pm 0.8 \text{ mK}, \quad (7.9)$$

directed toward a RA of 10.5 ± 4 h and a declination D of $[-30 \pm 25]^\circ$. These preliminary observations—Conklin in 1969 and in 1972, Henry in 1971—have indicated the existence of a dipole anisotropy; but both the direction and the amplitude were largely uncertain. The next generation of experiments started in 1976 with the balloon experiments of the Princeton group [185], the U-2 experiments of the Berkeley group [186] and the balloon experiments of the Florence group [187].

These three groups precisely measured the amplitude and direction of the dipole anisotropy and extended the analysis to millimeter wavelengths, thereby confirming the Planckian character of the observed signal. A first review of the subject is in [93], where the previous data are compared with the first results of COBE; see also [19, 171].

The main CMB dipole measurements—which are more and more accurate both in amplitude and in direction—are collected in Table 7.1.

Note that in this table the results from Henry and from Corey and Wilkinson constituted respectively the discovery and a first confirmation of the dipole, while the other

ones provided improved measurements of the dipole. Remark also that the results from the Melchiorri group were the first ones, before DMR/COBE, in the millimetric part of the CMB.

7.3 The physical origin of the dipole anisotropy

The large value—about two orders of magnitude higher than other anisotropies—of the dipole anisotropy clearly points in favor of a kinetic origin. The kinetic explanation requires a peculiar velocity of the observer, which can be only explained as the result of gravitational acceleration integrated in time.

Therefore, the dipole anisotropy results from the sum of many components of velocity due to gravitational attraction of various mass concentrations.

In particular, from the value of the dipole measured by WMAP [191], we have $\Delta T = 3.346 \pm 0.017$ mK, and the implied velocity for the solar system barycenter is $v = 368 \pm 2$ km/s, towards $(l, b) = (263.85^\circ \pm 0.1^\circ, 48.25^\circ \pm 0.04^\circ)$. Such a velocity of the solar system implies a velocity—relative to the CMB—for the galaxy and the Local Group of galaxies of $v_{LG} = 627 \pm 22$ km/s towards $(l, b) = (276^\circ \pm 3^\circ, 30^\circ \pm 3^\circ)$. For a discussion of the size of the region within which the motion of the Local Group is shared by other galaxies, see for instance [192]; Branchini, Plionis and Scrima [193] have observed that the gravitational acceleration of many different samples of extragalactic objects is relatively well aligned with the direction of the CMB dipole.

The motion is also confirmed by measurements of the velocity field of local galaxies [194]. Anyway, understanding the peculiar velocity field in the universe is an important addition to the study of the anisotropies in the CMB.

7.4 Conclusions

An examination of the CMB map—see for instance Fig. 7.1—reveals a very gradual shift in temperature, by

Table 7.1 The main CMB dipole measurements (dipole amplitude, galactic longitude l , galactic longitude b , observational frequency)

Reference	Amplitude $\pm 1\sigma$ (in mK)	$l \pm 1\sigma$	$b \pm 1\sigma$	Frequency (in GHz)
Henry [184]	3.3 ± 0.7	270 ± 30	24 ± 25	10
Corey and Wilkinson [185]	2.4 ± 0.6	306 ± 28	38 ± 20	19
Smoot et al. [186]	3.5 ± 0.6	248 ± 15	56 ± 10	53
Fabbri et al. [187]	2.9 ± 0.95	256.7 ± 13.8	57.4 ± 7.7	300
Boughn et al. [188]	3.78 ± 0.30	275.4 ± 3.9	46.8 ± 4.5	46
Lubin et al. [189]	3.44 ± 0.17	264.3 ± 1.9	49.2 ± 1.3	90
COBE/FIRAS [119]	3.372 ± 0.005	264.14 ± 0.17	48.26 ± 0.16	300
COBE/DMR [190]	3.358 ± 0.023	264.31 ± 0.17	48.05 ± 0.10	53
WMAP [191]	3.346 ± 0.017	263.85 ± 0.1	48.25 ± 0.04	

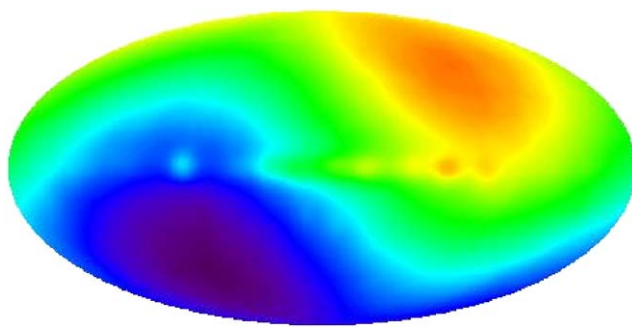


Fig. 7.1 Map of the dipole based on four years of DMR/COBE observations: the red part of the sky is hotter by $(v/c)T_0$, while the blue part of the sky is colder by $(v/c)T_0$. This all-sky image in galactic coordinates is plotted using the equal-area Molweide projection; see <http://lambda.gsfc.nasa.gov/product/cobe>

about 1.27 part in 1 000, from one side of the sky to the opposite side. One direction is a little hotter than the average, and the opposite direction a little cooler. The origin of this dipole anisotropy seems to be kinetic, thereby confirming the initial predictions of Scrima: maps of the CMB enable us to measure our velocity through the universe quite precisely—both how fast we are going and in what direction—to an accuracy of a few percent.

8 Cosmic microwave background anisotropies (CMBA)

The detection of the CMB radiation [7] and the confirmation of the thermal nature of the CMB radiation by the COBE/FIRAS instrument [195]) can be seen as the first revolution of the 2.7 K radiation.

The temperature anisotropy of the CMB, first detected by the COBE/DMR instrument [12]—spatial variations of order $\Delta T/T \sim 10^{-5}$ across $10^\circ\text{--}90^\circ$ on the sky—can be seen as the *second revolution* of the 2.7 K radiation.

These 10^{-5} variations in temperature represent the direct imprint of initial gravitational potential perturbations on the CMB photons, called the Sachs–Wolf effect [196].

One must note that until 1990 CMB anisotropies have been supposed to be marginally detected, in a few limited regions, by the Groups of Melchiorri [197], Lubin [199] and Davies [198].

The very low amplitude of the observed signals, usually at 1–2 standard deviations above the noise, and the lack of confirmations have led cosmologists to consider these observations as *upper limits*.

However, these upper limits, especially those at small angular scales by Wilkinson Group [200] and those around 3 and 6 degrees by Davies and Melchiorri have led cosmologists to exclude pure baryonic universes, thereby opening the door to the possibility of contributions of non-baryonic dark matter.

Then, just after the COBE/DMR detection, from 1992 to 1998, several experiments detected a rise and fall in the level of anisotropy from degree scales to arcminute scales.

From a theoretical point of view, since the seventies, cosmologists like Peebles and Yu [201], Doroshkevich et al. [202] and Bond and Efstathiou [203] have shown that most of the structure in the temperature anisotropy, on scales close on $\sim 1^\circ$ scales, must be associated with acoustic oscillations of the photon–baryon plasma at the time of recombination or just before.

The detailed theory predicting these CMBA—these acoustic peaks in the CMB temperature—has been elaborated by Seljak [204], Hu and Sugiyama [221], Hu and White [205] and Hu et al. [206], in particular.

The location of the first peak of the anisotropy was determined by the BOOMERANG [207], MAXIMA [208] and ARCHEOPS [31] experiments. The measurement of this first peak has been confirmed by many other groups. More precise measurements of the first five peaks are currently done by ground-based experiments and by the satellite WMAP [66, 217].

General reviews on the CMB anisotropies have been written, in the last decade, by many authors. Among them, let us recall Bond [209], Kamionkowski and Kosowsky [210], Hu and Dodelson [211], Hu [213] and, more recently, again Hu [214].

Present and future CMB measurements are essentially concerned with small-scale anisotropies on scales of close to 1° and less. The recent data, WMAP in particular, provide undeniable evidence for the interpretation of these small-scale CMBA in terms of acoustic oscillations; therefore we adopt the notation, the set of equations governing the small-scale CMB anisotropies and, of course, the interpretation given by Hu et al.

In this section, we define the CMBA observables; then we recall the role of Thomson scattering in the primordial plasma. Therefore, we recall the basics of fluid dynamics, and finally, we present acoustic oscillations in the primordial plasma.

8.1 CMB observables

The primary aim of the CMB satellite experiments such as COBE, WMAP and PLANCK is to map the temperature $T(\hat{n})$ of the CMB and its polarization, described by the Stokes parameters $Q(\hat{n})$ and $U(\hat{n})$, as functions of position \hat{n} on the sky. Many temperature–polarization angular correlation functions, or equivalently, power spectra, can be extracted from such maps. Then these quantities can be compared with detailed predictions from cosmological models.

A harmonic description is well adapted in order to analyze the anisotropy of the distribution of photons in the sky.

Thus the temperature field $\Theta(\hat{\mathbf{n}})$ can be expressed in spherical harmonics:

$$\Theta(\hat{\mathbf{n}}) = \frac{\Delta T}{T} = \frac{T(\hat{\mathbf{n}}) - T_0}{T_0} = \sum_{lm} \Theta_{lm} Y_{lm}(\hat{\mathbf{n}}), \quad (8.1)$$

$\hat{\mathbf{n}}$ is the normalized direction of the line of sight, Y_{lm} is the ordinary harmonic and $T_0 \sim 2.728$ K is the present CMB temperature [200]. If we have a Gaussian random temperature fluctuations, the fluctuations are fully characterized by their power spectrum (where the * symbol characterizes the conjugate term):

$$\langle \Theta_{lm}^* \Theta_{l'm'} \rangle = \delta_{ll'} \delta_{mm'} C_l^{TT}, \quad (8.2)$$

with

$$C_l^{TT} = \sum_{m=-l}^{m=l} \Theta_{lm} \Theta_{lm}^*. \quad (8.3)$$

The temperature correlation power spectrum, $\Delta_T |_{TT}$, is usually displayed thus:

$$\Delta_T^{TT} \equiv T \sqrt{\frac{l(l+1)C_l^{TT}}{2\pi}} \quad (\text{in } \mu\text{K}), \quad (8.4)$$

the power per logarithmic interval in wave number for $l \gg 1$. This quantity gives the contribution to the total variance in temperature from the mean-square fluctuation at an angular scale: $\theta \sim 180^\circ/l$. Figure 8.1, which shows the temperature power spectrum from WMAP in five-year data, provides *incontrovertible* evidence for the interpretation of these anisotropies in terms of *acoustic peaks* [217].

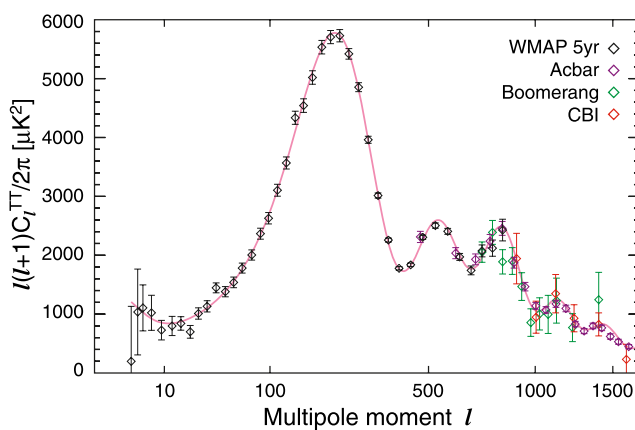


Fig. 8.1 The WMAP five-year TT power spectrum along with recent results from the ACBAR (due to Reichardt [215], purple), Boomerang (Jones [224], green), and CBI (Readhead [225], red) experiments. The red curve is the best-fit Λ CDM model to the WMAP data, (curves from the CAPMAP experiment; see <http://lambda.gsfc.nasa.gov/product/map/>)

8.2 Thomson scattering

Let us remember that the properties of the plasma before recombination are governed by Thomson scattering of photons on free electrons, which has a differential cross section, where ϖ is the solid angle, such as

$$\frac{d\sigma}{d\varpi} = \frac{3}{8\pi} [\check{\mathbf{E}}' \cdot \check{\mathbf{E}}]^2 \sigma_T, \quad (8.5)$$

with the Thomson cross section

$$\sigma_T \sim 6.65 \times 10^{-25} \text{ cm}^2. \quad (8.6)$$

$\check{\mathbf{E}}$ and $\check{\mathbf{E}}'$ denote the incoming and outgoing directions of the electric field.

The optical depth τ (related to the comoving mean free path of photons, l_λ), is given by

$$d\tau = n_e \sigma_T c dt. \quad (8.7)$$

This equation is coupled with the evolution equation of chemistry, because it is strongly dependent on the electron densities (see Sect. 5).

At $z = 1000$, where the ionized fraction $x_e \sim 1$, the comoving mean free path of photons is $l_{\lambda 1000} \sim 2.5$ Mpc. On scales $l_\lambda \gg l_{\lambda 1000}$, photons are tightly coupled to the electrons by Thomson scattering, which in turn are tightly coupled to the baryons by Coulomb interactions. The dynamics that results involves for the primordial plasma description by a single photon–baryon fluid (called the *tight-coupled fluid* or the *photon-dominated fluid*) instead of two fluids for the general case.

Now, we shall consider inhomogeneities in the primordial plasma. These inhomogeneities, which will eventually become the large-scale structures we see in the universe today, grew from tiny seeds at the last scattering surface. To handle this situation, we need to use relativistic perturbation theory in an expanding universe. Well inside the horizon, we can use ordinary Newtonian gravity, but on larger scales the details of general relativity come into play. Details of relativistic perturbation theory lie beyond the scope of this paper but are discussed in [218–220].

Let us only remark that there exists a disparity between the smooth photon distribution and the clumpy matter distribution which is due to radiation pressure: even if inhomogeneities in the matter in the universe and anisotropies in the CMB originated from the same sources, they appear very different today. Here, as said above, we adopt the point of view of Hu et al. and treat the primordial plasma in a *fluid approximation*. We shall see that the photon pressure sets up sound waves or acoustic oscillations in the fluid. These sound waves are frozen into the CMB at recombination. Regions that have reached their maximal compression by recombination become hot spots on the sky; those that reach

maximum rarefaction become cold spots. In order to understand the angular pattern of temperature fluctuations seen by the observer today, one must not only understand the spatial temperature pattern at recombination, but more generally, the evolution of perturbations in the photon–baryon fluid. In the next subsection, we shall recall some sound physics (i) in a perfect fluid, (ii) when gravity effects are added, (iii) when baryon effects are also taken into account, (iv) and finally, when the most dissipative baryon–photon fluid is considered.

8.3 Acoustic oscillations in the photon–baryon fluid

As suggested above, we consider, for the primordial plasma, a description by a photon–baryon fluid. Perturbations, in this description, satisfy an equation of continuity and an Euler equation—for each component—which can be written in Fourier space.

The spatial power spectrum at recombination can be decomposed into its Fourier modes:

$$\Theta(x) = \frac{1}{(2\pi)^3} \int e^{ikx} \Theta(k) d^3k, \quad (8.8)$$

where k is the wave number. Since perturbations are very small, we can do the linear approximation for the perturbations. We introduce the following variables: the photon “temperature” $\Theta = \Delta T/T$, the photon-fluid velocity v_γ for the photon fluid, the baryonic-density perturbation δ_b , the bulk velocity v_b for the baryon fluid. We consider that in the primordial plasma this photon-fluid velocity, in particular, is approximately parallel to the wave vector \mathbf{k} . In the following subsection, in the framework of the very particular case of a *perfect-fluid approximation* for the primordial plasma, we can show the main features—peaks and troughs—of the anisotropy spectrum.

8.3.1 Acoustic oscillations in the photon-dominated fluid

Therefore, we consider, first, the *tight-coupled fluid* or the *photon-dominated fluid* as a perfect gas without gravity and dissipative effects. The only variables at work are Θ and v_γ . In the Fourier space, the equation of continuity for Θ is

$$\frac{d\Theta}{dt} = -\frac{1}{3}kv_\gamma, \quad (8.9)$$

while the corresponding Euler equation is

$$\frac{dv_\gamma}{dt} = k\Theta, \quad (8.10)$$

where we have taken into account that the numerical density of photons n_γ scales as

$$n_\gamma \sim T^3, \quad (8.11)$$

and with the equation of state for photons:

$$p_\gamma = \frac{\rho_\gamma}{3}, \quad (8.12)$$

where p_γ and ρ_γ are respectively the pressure and the energy density of the photon fluid.

Combining the equation of continuity (8.9) with the Euler equation (8.10) in the Fourier space, one gets the harmonic oscillator equation:

$$\frac{d^2\Theta}{dt^2} + c_s^2 k^2 \Theta = 0, \quad (8.13)$$

where the sound speed is given by

$$c_s^2 = \frac{dp_\gamma}{d\rho_\gamma} \equiv \frac{1}{3}, \quad (8.14)$$

for the photon-dominated fluid. The solution of this oscillator equation can be written

$$\Theta(\eta) = \Theta(0) \cos(ks) + \frac{1}{kc_s} \frac{d\Theta}{dt}(0) \sin(ks), \quad (8.15)$$

where the value $\Theta(0)$ is relative to the initial conditions and s , such as in $ds = c_s d\eta$, is the horizon. In real space, these oscillations appear as standing waves for each Fourier mode. These standing waves continue to oscillate until recombination. At this point, the free-electron density drops drastically and the photons freely stream to the observer. The pattern of acoustic oscillations on the recombination surface seen by the observer becomes the acoustic peaks in the temperature anisotropy. Actually, assuming a negligible initial velocity perturbation, the temperature distribution at recombination η_{rec} is

$$\Theta(\eta_{\text{rec}}) = \Theta(0) \cos(ks_{\text{rec}}). \quad (8.16)$$

On small scales, the amplitude of the Fourier modes exhibits temporal oscillations as shown in Fig. 8.1. Modes caught in the extrema of their oscillations at recombination, corresponding to peaks in the spectrum, follow a harmonic relation:

$$k_n = \frac{\pi}{s_{\text{rec}}} n \quad \text{for } n = 1, 2, 3, \dots \quad (8.17)$$

As shown by Hu and White [205], observational verification of this harmonic series is the primary evidence for inflationary initial conditions.

A spatial perturbation in the CMB temperature of wavelength λ appears as an angular anisotropy of scale $\theta \sim \lambda/D$, where $D(z)$ is the comoving angular diameter distance to redshift z . The above harmonic relation implies a series of acoustic peaks in the anisotropy spectrum, located at

$$l_n = \frac{\pi D_{\text{rec}}}{s_{\text{rec}}} n \quad \text{for } n = 1, 2, 3, \dots \quad (8.18)$$

In a flat ($D_{\text{rec}} = \eta_0 - \eta_{\text{rec}}$) matter-dominated ($\eta \equiv \sqrt{a}$) universe, we have

$$\frac{\eta_{\text{rec}}}{\eta_0} \sim 2^\circ \quad \text{or} \quad l_1 \sim 200. \quad (8.19)$$

Let us only remark that in a spatially curved universe, the angular diameter distance no longer equals the coordinate distance. One can show that a given comoving scale at a fixed distance subtends a larger (smaller) angle in a closed (open) universe than a flat universe (see Fig. 8.2).

Therefore, the observed first peak at $l_1 \sim 200$ (see Fig. 8.1) constrains the universe to be nearly spatially flat. Note that, for any perturbation in the primordial plasma before recombination, even this simple approximation of a photon-dominated perfect fluid already leads to the above description of acoustic oscillations in the temperature power spectrum. Thus far, we have neglected gravitational forces and redshifts in our discussion of our plasma description. Now, we shall include these effects.

8.3.2 Oscillations in the photon-dominated fluid with spatial curvature Φ and gravitational potential Ψ

Here, we shall see how the gravitational potential perturbations from inflation can be the sources of the initial temperature fluctuations. For a flat cosmology, one can write the metric

$$ds^2 = a^2[(1 + 2\Psi)d\eta^2 - (1 + 2\Phi)dx^2]. \quad (8.20)$$

The continuity equation, (8.9), for the fluctuations in the Fourier space becomes

$$\frac{d\Theta}{dt} = -\frac{1}{3}kv_\gamma - \frac{d\Psi}{dt}, \quad (8.21)$$

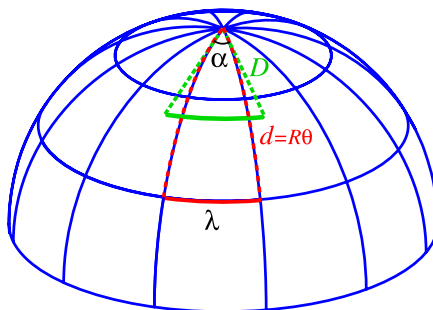


Fig. 8.2 In a closed universe, objects are further than they appear to be from Euclidean (flat) expectations corresponding to the difference between coordinate distance d and angular distance D . Consequently, at a fixed coordinate distance, a given angle corresponds to a smaller spatial scale in a closed universe. Acoustic peaks therefore appear at larger angles or lower l in a closed universe. The converse is true for an open universe (illustration from Hu and Dodelson [211])

while the corresponding Euler equation (8.10) can be written

$$\frac{dv_\gamma}{dt} = k(\Theta + \Psi). \quad (8.22)$$

Combining these two last equations one obtains the *forced harmonic oscillator* equation:

$$\frac{d^2\Theta}{dt^2} + c_s^2 k^2 \Theta = -\frac{k^2}{3}\Psi - \frac{d^2\Phi}{dt^2}. \quad (8.23)$$

To better come to know the effect of gravity on acoustic oscillations we need now to specify Φ and Ψ through a cosmological Poisson equation. Here, we only consider the particular case of constant gravitational potentials. The oscillator equation (8.23) becomes

$$\frac{d^2\Theta}{dt^2} + \frac{d^2\Psi}{dt^2} + c_s^2 k^2 (\Theta + \Psi) = 0. \quad (8.24)$$

The solution given for adiabatic initial conditions in (8.16) can be generalized by

$$[\Theta + \Psi](\eta) = [\Theta + \Psi](0) \cos(ks). \quad (8.25)$$

Like a mass on a spring in a constant gravitational field of the earth, the solution represents oscillations around a displaced minimum. Furthermore, $\Theta + \Psi$ is also the observed temperature fluctuation. Photons lose energy climbing out of gravitational potentials at recombination and so the observer at present will see

$$\frac{\Delta T}{T} = \Theta + \Psi. \quad (8.26)$$

For the observer, acoustic oscillations are unchanged, but now he observes initial perturbations in the effective temperature which oscillate around zero with a frequency given by the sound speed. In fact, what the consideration of gravity adds is a way of connecting the initial conditions to inflationary curvature fluctuations.

8.3.3 Oscillations in the photon-dominated fluid with Θ , Ψ and baryonic effects: baryon loading

Now, we consider that baryons add extra mass to the above tightly coupled plasma with gravity. If the continuity equation remains given by

$$\frac{d\Theta}{dt} = -\frac{1}{3}kv_\gamma - \frac{d\Phi}{dt}, \quad (8.27)$$

one can show that the Euler equation is

$$\frac{d[(1 + R)v_\gamma]}{dt} = k\Theta + (1 + R)k\Psi, \quad (8.28)$$

with

$$R \equiv \frac{p_b + \rho_b}{p_\gamma + \rho_\gamma}. \quad (8.29)$$

Therefore, the oscillator equation becomes

$$\begin{aligned} \frac{d}{dt} \left((1+R) \frac{d\Theta}{dt} \right) + \frac{k^2}{3} \Theta \\ = -\frac{k^2}{3} (1+R) \Psi - \frac{d}{dt} \left((1+R) \frac{d\Phi}{dt} \right). \end{aligned} \quad (8.30)$$

One can show that after several simplifications

$$\Phi = -\Psi = \text{constant} \quad \text{and} \quad \frac{1}{R} \frac{dR}{dt} \ll \omega,$$

where ω is the frequency of oscillations, and the above solution is modified as follows:

$$[\Theta + (1+R)\Psi](\eta) = [\Theta + (1+R)\Psi](0) \cos(ks). \quad (8.31)$$

These equations are those of a mass $m \equiv 1+R$ added to the spring in a constant gravitational field. One can show that there are several baryonic effects.

- The amplitude of the oscillations increases by a factor of $(1+3R)$.
- The *zero point* of the oscillations is shifted.
- The symmetry of the oscillations is broken so that even and odd peaks have different amplitudes.

Therefore, the modulation of the peak heights provides most of the information about the baryon–photon ratio in the acoustic peaks. One can say that, in particular, with the precise measurement of the first and second peaks, one obtains for the baryon–photon ratio a better sensitive value than the value given by nucleosynthesis.

8.3.4 Oscillations in the photon-dominated fluid with radiation effects: radiation driving

For all the above acoustic oscillations and their peaks, we assumed that recombination roughly takes place, for reasonable values of cosmological parameters, at the epoch of energy-density equality (which corresponds to the redshift z_{eq}) between matter and radiation, i.e. when

$$\frac{\rho_m}{\rho_r} \sim 24 \frac{\Omega_m h^2}{(1+z_{\text{eq}})^3} \sim 1. \quad (8.32)$$

Now, we consider peaks which correspond to wave numbers that began oscillating earlier than that epoch. These higher peaks must carry all the effects of the radiation-domination epoch.

Hu and Sugiyama [221] have shown that radiation has the unique effect of driving the acoustic oscillations by making

the gravitational force evolve with time while matter does not. They have also calculated [222] that across the horizon scale at matter–radiation equality the amplitude of these acoustic oscillations increases by a factor of 5 for a pure photon fluid and dark-matter universe and a factor of 4 when including neutrinos and baryons.

Therefore, observations of these high peaks bring about important information about the contents of the universe at recombination.

8.3.5 Oscillations in the two-fluid primordial system: photon and baryon damping

Until this point, photons and baryons are considered as a single perfect fluid, the so-called photon-dominated fluid approximation or *tight-coupling approximation* with, in particular, a single bulk velocity $v_b = v_\gamma$ and hence no entropy generation.

First, fluid imperfections are only associated with the Compton mean free path λ_C given by the relation

$$\lambda_C = \frac{1}{n e \sigma_T a_{\text{rec}}} \sim 2.5 \text{ Mpc}. \quad (8.33)$$

Damping can be thought of as the result of the random walk in the baryons that takes photons from hot into cold regions and vice and versa. In particular, Silk [223] has shown that dissipation can become strong at the diffusion scale, the distance a photon can random walk in a given time η :

$$\lambda_D = \lambda_C \sqrt{\eta \lambda_C}. \quad (8.34)$$

Then, to consider these dissipative effects, one must treat the photons and baryons as separate systems and introduce two continuity equations:

$$\frac{d\Theta}{dt} = -\frac{1}{3} k v_\gamma - \frac{d\Phi}{dt}, \quad (8.35)$$

$$\frac{d\delta_b}{dt} = -k v_b - 3 \frac{d\Phi}{dt}, \quad (8.36)$$

with two coupled Euler equations:

$$\frac{dv_\gamma}{dt} = k(\Theta + \Psi) - \frac{k}{6} \pi_\gamma - \frac{d\tau}{dt} (v_\gamma - v_b), \quad (8.37)$$

$$\frac{dv_b}{dt} = -\frac{1}{a} \frac{da}{dt} v_b + k\Psi + \frac{d\tau}{dt} \frac{v_\gamma - v_b}{R}, \quad (8.38)$$

where δ_b and v_b are respectively the density perturbation and the bulk velocity of the baryons and where

$$R = \frac{p_b + \rho_b}{p_\gamma + \rho_\gamma} \sim 3 \frac{\rho_b}{\rho_\gamma} \quad (8.39)$$

is the photon–baryon momentum-density ratio. Note that the third term in both Euler equations—with $d\tau/dt$ given by

(8.33)—is a momentum-exchange term from Compton scattering but with opposite signs, since the total momentum is conserved. The second term in the Euler equation of the photon is due to radiation viscosity π_γ , which can be given by

$$\pi_\gamma = 2k v_\gamma \left(\frac{d\tau}{dt} \right)^{-1} A_\gamma, \quad (8.40)$$

with $A_\gamma = 16/15$ [212].

The first term in the Euler equation of the baryon is, of course, due to the cosmological expansion. Thus, the final *oscillator equation* becomes

$$\begin{aligned} c_s^2 \frac{d}{d\eta} \left(\frac{1}{c_s^2} \frac{d\Theta}{dt} \right) + k^2 c_s^2 \left(\frac{d\tau}{dt} \right)^{-1} [A_\gamma + A_h] \frac{d\Theta}{dt} + k^2 c_s^2 \Theta \\ = -\frac{k^2}{3} \Psi - c_s^2 \frac{d}{d\eta} \left(\frac{1}{c_s^2} \frac{d\Theta}{dt} \right), \end{aligned} \quad (8.41)$$

where A_h represents heat conduction with

$$A_h = \frac{R^2}{1+R}. \quad (8.42)$$

As for a mechanical oscillator, a term that depends on $d\Theta/dt$ provides a dissipation term to the solutions. Furthermore, a precise examination of this damped oscillator equation [211, 214] shows that diffusion damps the oscillation amplitude by a factor of order α_τ such as

$$\alpha_\tau = \exp \left[-k^2 \eta \left(\frac{d\tau}{dt} \right)^{-1} \right], \quad (8.43)$$

the damping scale being

$$k_d \sim \sqrt{\frac{1}{\eta} \frac{d\tau}{dt}}; \quad (8.44)$$

see Fig. 8.3, where we plotted a numerical solution of (8.36) and (8.37) with the various effects on acoustic oscillations described above: gravity, baryon loading, radiation driving and damping.

We have described the various effects which can be at the origin of the wave form of the temperature anisotropy spectrum: see, for instance, in Fig. 8.1 the WMAP five-year TT power spectrum. We shall present later (Sect. 10) what precise pieces of information—such as cosmological parameters—have been extracted from such a spectrum by the WMAP team. But now it is time to introduce polarization and its different power spectra.

8.4 Polarization anisotropies

The CMB polarization is an important quest of the observational cosmology, because this observation permits one

to characterize the earliest photons from the universe. After a long list of ever-decreasing upper limits, detection of polarization was made in 2002 by the DASI team at the Legendre number $l \sim 500$ and confirmed with the CAPMAP (i.e. Cosmic Anisotropy Polarization MAP) instrument with the measurement of the E-mode and B-mode power spectra [216].

The existence of polarization is a robust prediction of the standard cosmological picture, so a precise measurement of the CMB polarization should come as a confirmation of the standard model. Nevertheless, polarization measurements represent an experimental challenge. The weakness of the polarization signal requires both a demanding instrumental sensitivity and attention focused to all sources of systematic error.

Polarization of the CMB is naturally created by the Thompson scattering of photons off electrons at the moment of decoupling. The cross section of radiation scattered by a charged particle of charge e and mass m is given by

$$\frac{d\sigma}{d\omega} = \left(\frac{e^2}{m_e c^2} \right)^2 |\hat{\mathbf{e}} \cdot \hat{\mathbf{e}}|^2, \quad (8.45)$$

where $\hat{\mathbf{e}}$ and $\hat{\mathbf{e}}$ are the unit vectors indicating the linear polarization of the incident and scattered photon. This equation predicts that only a quadrupole distribution of initially unpolarized radiation will generate a linearly scattered polarization.

Thus, during the epoch of recombination, the electrons can produce a net linear polarization because of local quadrupole moments generated by Doppler-shifted radiation. The Doppler shift is the result of local velocity fields in the baryon–photon plasma. The scattered radiation will be polarized parallel to the crest and perpendicular to the wave vector.

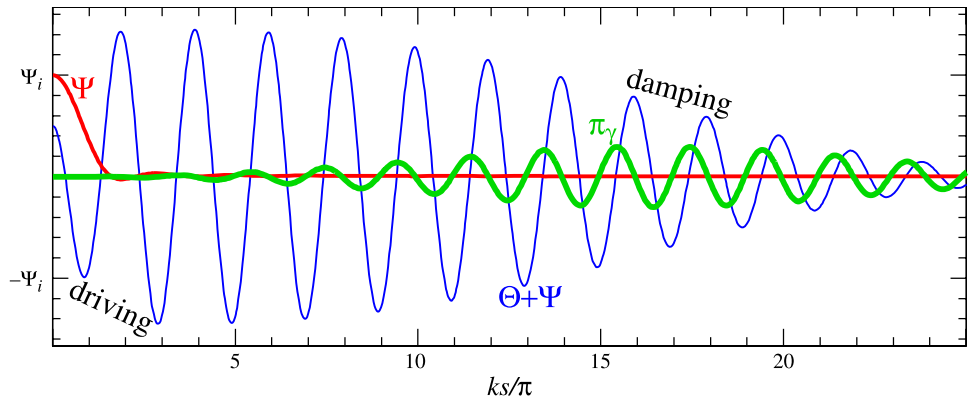
In general, when the scattered polarization direction is either parallel or perpendicular to the wave vector of the perturbation, the polarization pattern is referred to as an E-mode pattern. When the polarization direction is at 45° to the wave vector, the polarization pattern is called a B-mode.

The decomposition of a polarization field into a sum of E- and B-modes has become the standard of analyzing polarization maps. Note that a B-mode pattern cannot be created by density perturbations and its presence would be a distinctive signature of primordial gravitational waves from inflation [210].

In terms of a multipole decomposition of the radiation field into spherical harmonics, Y_{lm} , the five quadrupole moments are represented by $m = 0, \pm 1$ and ± 2 . The orthogonality of the spherical harmonics guarantees that no other moment can generate polarization from Thomson scattering.

The state of polarization is described in terms of Stokes parameters, and it is convenient to describe the observables

Fig. 8.3 Acoustic oscillations with gravitational forcing and dissipation damping; illustration from [213]



by a temperature fluctuation matrix decomposed in the Pauli basis [211]:

$$\mathbf{P} = \Theta(\check{\mathbf{n}})\mathbf{I} + Q(\check{\mathbf{n}})\sigma_3 + U(\check{\mathbf{n}})\sigma_1 + V(\check{\mathbf{n}})\sigma_2, \quad (8.46)$$

where I is the total intensity, Q the Stokes parameter of linear polarization, V for the circular polarization and U gives information on the phase. I and V remain invariant, but with a rotation angle ψ . Q and U are transformed thus:

$$\begin{pmatrix} Q' \\ U' \end{pmatrix} = \begin{pmatrix} \cos 2\psi & \sin 2\psi \\ -\sin 2\psi & \cos 2\psi \end{pmatrix} \begin{pmatrix} Q \\ U \end{pmatrix}. \quad (8.47)$$

In cosmology the circular polarization V is absent; then we can decompose the field of polarization

$$E_{lm} \pm B_{lm} = - \int d\check{\mathbf{n}}_{\pm 2} Y_{lm}^*(\check{\mathbf{n}}) [Q(\check{\mathbf{n}}) \pm iU(\check{\mathbf{n}})], \quad (8.48)$$

where the vectors of the fields are given by

$$E(\check{\mathbf{n}}) = \sum E_{lm} Y_{lm}(\check{\mathbf{n}}) \quad (8.49)$$

and

$$B(\check{\mathbf{n}}) = \sum B_{lm} Y_{lm}(\check{\mathbf{n}}). \quad (8.50)$$

In this case we can define the multiple moments which are used as the primary observable, i.e. the two-point correlation between the fields E and B , in order to define the polarization correlation power spectra $\Delta_T^{(EE)}$ and $\Delta_T^{(BB)}$:

$$\begin{aligned} \langle E_{lm}^* E_{l'm'} \rangle &= \delta_{ll'} \delta_{mm'} C_l^{(EE)}, \\ \langle B_{lm}^* B_{l'm'} \rangle &= \delta_{ll'} \delta_{mm'} C_l^{(BB)} \end{aligned} \quad (8.51)$$

and the temperature–polarization correlation power spectra

$$\langle \Theta_{lm}^* E_{l'm'} \rangle = \delta_{ll'} \delta_{mm'} C_l^{(TE)}. \quad (8.52)$$

The E-mode polarization power spectrum not only provides a more direct link to the properties of the last scattering

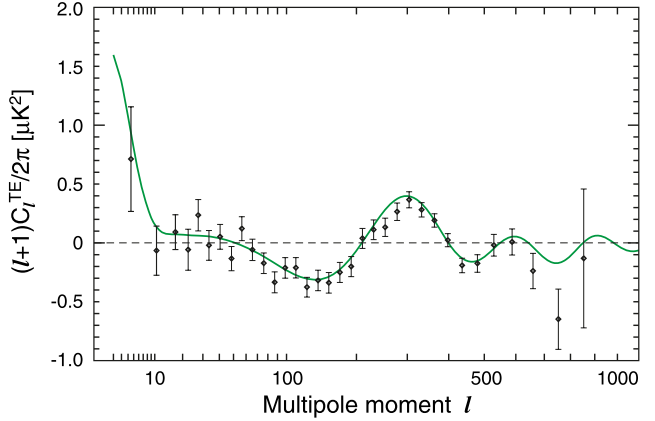


Fig. 8.4 The WMAP five-year TE power spectrum. The green curve is the best-fit theory spectrum from the Λ CDM/WMAP Markov chain [230]. The clear anticorrelation between the primordial plasma density (corresponding approximately to T) and velocity (corresponding approximately to E) in causally disconnected regions of the sky indicates that the primordial perturbations must have been on a superhorizon (curves from the CAPMAP experiment; see <http://lambda.gsfc.nasa.gov/product/map>)

surface than the temperature anisotropy but also offers complementary information which can be used to break various degeneracies in the determination of cosmological parameters. Nevertheless, the polarization signals (EE and BB) are much smaller than the temperature anisotropy spectrum; see Figs. 8.4, 8.5 and 8.6. Moreover, the polarized radiation is produced only near the end of recombination. The polarization spectra decline at large angular scales (low l), because photons could not diffuse so far before the end of recombination.

8.5 Secondary anisotropies

Beyond the peaks exists a lot of information on the origin and evolution of structure in the universe. As CMB photons travel from the recombination epoch to the observer, they traverse the large-scale structure of the universe and they pick up secondary temperature anisotropies. These sec-

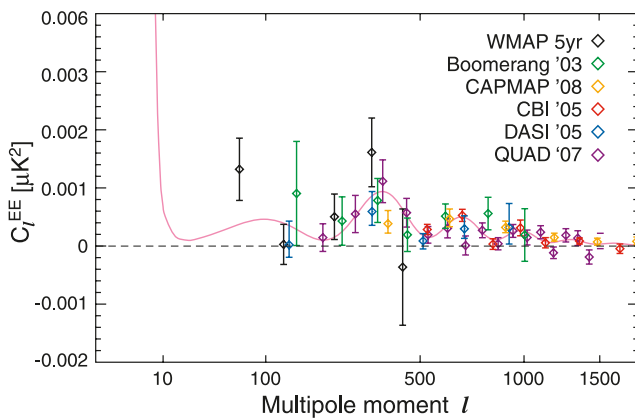


Fig. 8.5 WMAP five-year EE power spectrum, compared with results from the Boomerang (Montroy et al. [231], green), CBI (Sievers et al. [232], red), CAPMAP (Bischoff et al. [216], orange), QUAD (Ade et al. [233], purple), and DASI (Leitch et al. [234], blue) experiments. The pink curve is the best-fit theory spectrum from the Λ CDM/WMAP Markov chain [230], (curves from the CAPMAP experiment; see <http://lambda.gsfc.nasa.gov/product/map> and Nolta [235])

ondary anisotropies depend on the temperature distribution and on the intervening dark matter, dark energy, baryonic density and, if they exist, on primordial gravitational waves. Secondary anisotropies can be divided in two classes: secondaries due to gravitational effects and secondaries induced by scattering off of electrons.

8.5.1 Gravitational secondaries anisotropy

There are two main sources for gravitational anisotropy: fluctuations of gravitational potential and gravitational lensing.

- *The ordinary Sachs–Wolfe effect* (SW effect) [196] is simply the gravitational redshift (or blueshift) due to the potential differences between the points of emission and reception of a photon.
- *The integrated Sachs–Wolfe effect* (ISW effect) comes when the gravitational potential changes with time along the photon trajectory: the photon accumulates a redshift as it travels, which translates into a temperature perturbation. The magnitude of this ISW effect can be written by an integral along the photon's path:

$$\left(\frac{\Delta T}{T}\right)_{\text{ISW}} = \int [\Psi^o(x, \eta) - \Phi^o(x, \eta)] d\eta, \quad (8.53)$$

where, as seen above, Φ is the perturbation to the spatial curvature and Ψ is essentially the Newtonian gravitational potential. Let us remark that the ISW effect is linear in the perturbations. Finally, one can stress that the ISW effect is the most direct signature of the dark energy available in the CMB and is very sensitive to its equation of state.

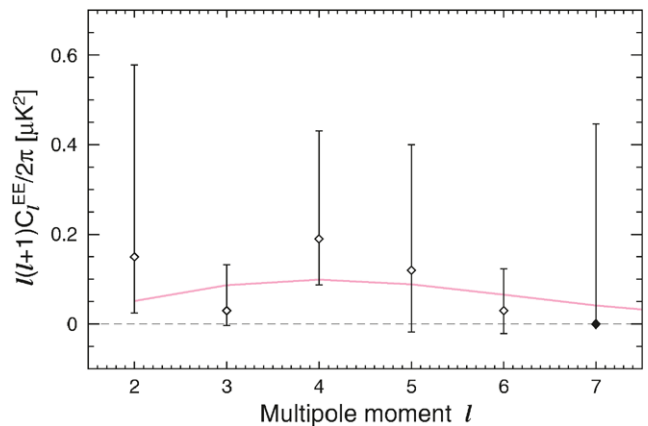


Fig. 8.6 WMAP five-year EE power spectrum at low l . The error bars are for 68% CL of the conditional likelihood of each multipole, with the other multipoles fixed at their fiducial theory values; the diamonds mark the peak of the conditional likelihood distribution. The error bars include noise and cosmic variance; the point at $l = 7$ is the 95% CL upper limit. The pink curve is the fiducial best-fit Λ CDM model [230] (curves from the CAPMAP experiment; see <http://lambda.gsfc.nasa.gov/product/map>)

• *The Rees–Sciama effect* (RS effect) [226]. When structure forms, linear perturbations become non-linear ones and the corresponding ISW effect may be called the RS effect. Note that the bulk motion of dark-matter halos of all masses contribute to the RS effect. But note also that this RS effect is much weaker than all the other effects.

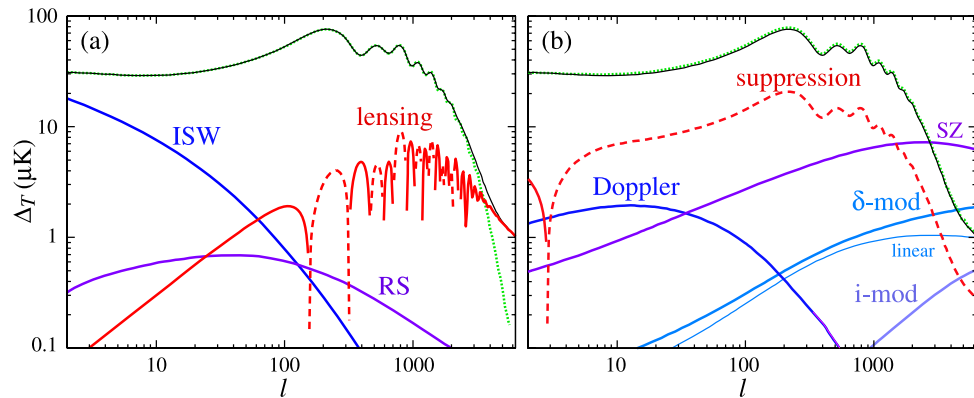
• *The lensing effect*. The above gravitational secondaries (in particular the ISW effect) may be thought of as gravity imparting a “kick” to a photon forward or backward along the direction of motion. Gravity can also kick the photons in the transverse directions, changing their directions of motion but not their energies. The result of this weak gravitational lensing is that our image of the last scattering surface is slightly distorted. This results in a very slight smearing of the angular power spectrum, with power from the peaks being moved into the valleys [227]. Let us only note that gravitational lensing also generates a small amount of power in the anisotropies on its own. See all these gravitational anisotropies in Fig. 8.7 (left panel), where their amplitudes are plotted versus l or the angular scale $\theta = 180^\circ/l$.

8.5.2 Scattering secondaries anisotropy

The main sources of scattering anisotropies are interactions of CMB photons with newly available electrons: the Sunyaev–Zel'dovich effect and reionization effects.

- *The Sunyaev–Zel'dovich effect* (SZ effect) [228]. CMB photons passing through clusters undergo Compton scattering by collisions with electrons in the ionized plasma causing spectral distortions in the CMB, where photons on the Rayleigh–Jeans side are transferred to the Wien tail. This largely measured effect gives important information on the

Fig. 8.7 Secondary anisotropies. (a) Gravitational anisotropies: ISW, lensing and Rees–Sciama (moving halo) effects. (b) Scattering secondaries: Doppler, density (δ) and ionization (i) modulated Doppler, and the SZ effect. Curves and model come from Hu and Dodelson [213]



physics of clusters and on dark energy. Although this effect is supposed to dominate the power spectrum of secondary anisotropies, other effects of scattering anisotropies are measurable.

- *The reionization effects.* In all cosmological models, the universe is thought to have undergone reionization sometime between $6 < z < 30$: a few percent of the photons have rescattered since recombination. This rescattering induces: suppression of the peaks of the primary anisotropies by a $\exp(-\tau)$, where τ is the optical depth defined above; and the generation of polarization.

These effects are very interesting since they give information about the sources of ionizing radiation, i.e. about the epoch of the formation of the first objects in the universe. Note that the WMAP five-year data show, in particular, that the epoch of reionization is now more than 3σ earlier than $z = 6.2$. All of these scattering anisotropies are described in Fig. 8.7 (right panel), where their amplitudes are plotted versus l or the angular scale $\theta = 180^\circ/l$.

As emphasized, in particular, by Melchiorri, one might add to this list: the *colored CMB anisotropies*. Actually, primary anisotropies can be partially erased at specific frequencies via Thomson resonant scattering, while the molecular clouds responsible for that are producing colored secondary anisotropies. Among the various possible primordial molecules, LiH has been chosen, in a first work [229], but the study is valid for other molecules, ions and atoms; see Sect. 9.

9 Cosmic microwave background anisotropies and primordial molecules

There have been several studies in order to gain understanding of chemical processes in the early universe as well as in the interactions of molecules with the CMB.

Dubrovich [236] analyzed the effect of hydrogen recombination lines on the CMB spectrum, while Rubiño–Martin et al. [237, 238] considered the effect of helium; see also the

recent discussions of Wong et al. [239] on the cosmological recombination process.

The main studies are relative to the postrecombination universe and possible imprints in the CMB from this period. The exhaustive work on the mechanisms of imprints from primordial molecules on the CMB was proposed by Schleicher et al. [167]. They presented the main effect of interaction and the rich physics which is involved.

Dubrovich [240, 241] analyzed the interaction of primordial molecules with the CMB, and the effect of various molecules due to their optical depths. Recently Mayer and Duschl [242] gave an overview of the opacity of the primordial gas. The main studies have focused on two directions:

- the influence on primary CMB fluctuations due to molecular optical depth, and
- the generation of secondary fluctuations due to scattering with protomolecular objects.

9.1 Imprint from primordial chemistry on CMB

The main mechanisms of interaction between CMB photons and primordial molecules are emission and absorption. Because their abundances are quite modest, collisional excitation and de-excitation are negligible and therefore emission and absorption are ineffective. The most obvious on the CMB is a frequency-dependent change in the observed CMB spectrum $I(\nu)$ due to absorption by a molecular species. For a given molecule, specified by the index mol , this effect is characterized by the attenuation, where $B(\nu)$ is the *incident* CMB spectrum:

$$I(\nu) = B(\nu)e^{-\tau_{mol}}, \quad (9.1)$$

where τ_{mol} is the optical depth of molecular species mol at the observed frequency ν_{obs} . If the emitted frequency is denoted ν_{em} at the redshift z_{em} , we have $\nu_{obs} = (1+z)\nu_{em}$.

Thus along the line of sight the optical depth is expressed by

$$\tau_{mol} = \int n_{mol}\sigma(\nu) dl, \quad (9.2)$$

or with an integration over the redshift:

$$\tau_{\text{mol}} = \int_0^{z_{\text{em}}} cn_{\text{mol}}(z) \sigma(v_{\text{em}}(1+z)) \frac{dz}{(1+z)H(z)} dz, \quad (9.3)$$

where n_{mol} is the numerical density of the molecular species mol and $\sigma(v_{\text{em}}(1+z))$ the absorption cross section of the considered species.

This optical depth can be caused by different processes of absorption, such as resonant line transitions, free–free processes or photodestruction of species which have a low photodissociation threshold.

Schleicher et al. [167] mentioned that this optical depth gives only an upper limit because inverse mechanisms, such as spontaneous and stimulated emission, can be balanced by the processes of absorption.

Thus, if we introduce the excitation temperature T_{ex} , which is determined by the ratio of collisional and radiative de-excitations, the frequency change in the radiation temperature T_r is expressed by [167]

$$\Delta T_r = (T_{\text{ex}} - T_r) \tau_{\text{mol}}. \quad (9.4)$$

From this expression a few remarks can be made on the efficiency of the processes of absorption.

- Molecular species with high dipole moments provide a high cross section of absorption but have an excitation temperature close to T_r .
- Molecular species with low dipole moments give a low optical depth, but their excitation temperature is different from the CMB temperature.
- Photodestruction processes are governed by the radiation temperature, while the formation processes are regulated by the gas temperature, which is the same for free–free mechanisms.
- Molecular resonant line transitions can lead to a net change in the radiation temperature, as the photodestruction processes can also lead to a net change in the number of CMB photons. Thus, a few effects associated with the chemistry may affect the optical depth seen by CMB photons.

9.1.1 Molecular lines

The elastic scattering is a mechanism during which a photon is first absorbed and then re-emitted at the same frequency, but not in the same direction. One should note that for a given molecular line, v_{ij} , each photon may be scattered only in a restricted range of redshift, when its redshifted frequency falls into the spectral width of the line such as

$$\frac{\Delta z}{z} \sim \frac{\Delta v_{ij}}{v_{ij}}. \quad (9.5)$$

The optical depth τ_{mol}^{ij} is given by

$$\tau_{\text{mol}}^{ij} = \int cn_{ij}^{\text{mol}} \sigma_d \frac{dz}{(1+z)H(z)}, \quad (9.6)$$

where n_{ij}^{mol} is the numerical density of the molecule diffusing at the level ij . The cross section of elastic scattering is given by the Sobolev diffusion cross section:

$$\sigma_d = \frac{(\lambda_{ij}^{\text{mol}})^3}{4c} A_{ij} \frac{v_{ij}}{\Delta v_D}, \quad (9.7)$$

where λ_{ij} and v_{ij} are respectively the wavelength and frequency of the transition roto-vibrational ij , A_{ij} is the first Einstein coefficient, and v_D the Doppler broadening.

For a dipole moment of order of unity, Maoli et al. [229, 243] showed that the resonant scattering could be 10^{10} – 10^{12} times more efficient than Thomson scattering (where $\sigma_T = 6.652 \times 10^{-25} \text{ cm}^2$).

They therefore suggested why the coupling with primordial molecules could be stronger than the coupling with electrons in spite of a low abundance of primordial molecules. Thus, the resonant scattering being an elastic process, it can result in a possible CMB primary anisotropy attenuation.

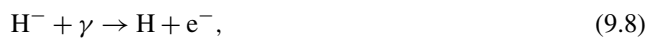
Maoli et al. [229] discussed that the optical depth from primordial molecules may smear out primary fluctuations in the CMB. They showed that, if the angular scale θ is below the angular diameter of the horizon θ_H , any given power spectrum of primary CMB anisotropies could be affected.

Recently, Schleicher et al. [167] proposed calculations for the different optical depths (corrected for stimulated emission) for HeH^+ and HD^+ , which are the most promising candidates. These molecules are interesting, because their dipole moment is relatively high, and because they are formed from quite abundant species. They showed that HeH^+ efficiently scatters CMB photons and smears out primordial fluctuations, leading to a change in the power spectrum close to 10^{-8} ; see Fig. 9.1.

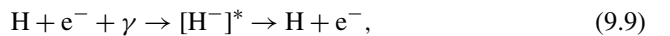
Notice that LiH is not considered because it has an even lower abundance [161] although the percentage of lithium converted to LiH is quite uncertain.

9.1.2 The negative hydrogen ion

Schleicher et al. [167] showed that there are two effects associated to the negative hydrogen ion H^- that can significantly affect the optical depth seen by the CMB photons. The first one is relative to the bound-free process of photodetachment:



and the second one is relative to the free–free transitions that involve excited H^- :



where $[\text{H}^-]^*$ is the intermediate state of excited H^- .

Schleicher et al. [167] showed that these are the most promising results. The free-free process leads to a frequency-change change in the power spectrum of the order 10^{-7} at 30 GHz; see Fig. 9.1.

9.1.3 Photodissociation of HeH^+

Photodissociation of HeH^+ can give extra photons and can give distortion on the power spectrum. The resulting cross section was calculated by Dubrovich [143].

Schleicher et al. [167] showed that the absorption optical depth due to this process is between $[10^{11}, 5 \times 10^{-11}]$ for frequencies higher than 2 000 GHz; see Fig. 9.1.

9.2 On the primordial molecular clouds

From an initial idea of Zel'dovich, Dubrovich [240, 241] showed that resonant elastic scattering must be considered as one of the most efficient processes in coupling matter and radiation at high redshift. It was noted that the cross section for resonant scattering between photons and molecules is several orders of magnitude larger than that between radiation and electrons: even a modest abundance of primordial molecules would produce significant Thomson-type scattering.

At this point, every velocity field (due to molecular motion or to cloud infall) would leave its imprints on CMB via a Doppler shift. This technique for exploring the dark ages of the universe has been analyzed by de Bernardis et al. [244], Melchiorri and Melchiorri [245], Maoli et al. [229] and Signore et al. [246] and was summarized by Puy and Signore [247].

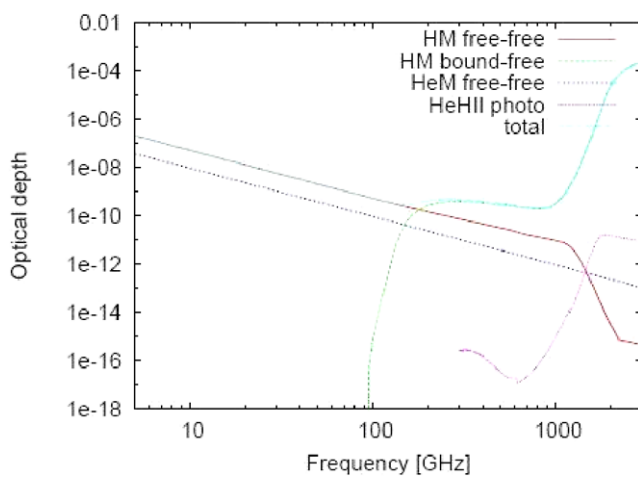


Fig. 9.1 The absorption optical depth due to different processes: HM line characterizes free-free processes, HM means bound-free process of H^- and the photodissociation of HeH^+ and the total line is the total optical depth. These curves come from the paper of Schleicher et al. [167]

Secondary anisotropies are expected if the scattering centers have peculiar velocities. In this case the angular distribution of the scattered photons is no more isotropic in the CMB reference frame, due to the Mosengheil effect.

The intensity is given by [229]

$$\frac{\Delta I}{I} = (3 - \alpha)\beta \cos \theta (1 - \exp(-\tau)), \quad (9.10)$$

with

$$\alpha = \frac{\nu}{I} \frac{\partial I}{\partial \nu}. \quad (9.11)$$

The lithium hydride LiH molecule was considered as a very good candidate for resonant scattering with CMB photons, because the value of the dipole moment is high (i.e. 5.88 Debye). Maoli et al. [229] first considered the spectrum of a single cloud located at different redshifts but with a mass corresponding to a galaxy cluster today. Figure 9.2 showed the theoretical spectrum for a cloud at $z = 200$ and for lithium abundance $[\text{LiH}] = 3 \times 10^{-8}$.

In order to estimate the real level of anisotropy, one has to take into account the effect of other N clouds along the line of sight having lines redshifted at the same frequency.

Figure 9.3 shows the expected anisotropy versus the frequency of observation. The angular size of these anisotropies would be that of protogalactic objects (i.e. $10''$ – $100''$). We note that these secondary anisotropies have a maximum in the range 20–100 GHz. Of course, the abundance of LiH in the molecular protoclusters are very high in comparison of the value given by the standard big-bang chemistry.

However, in the context of primordial molecular clouds, it is possible to think that the abundance could be higher, see the works of Puy and Pfenniger [152] on the differential chemistry in the baryonic fluctuations of matter.

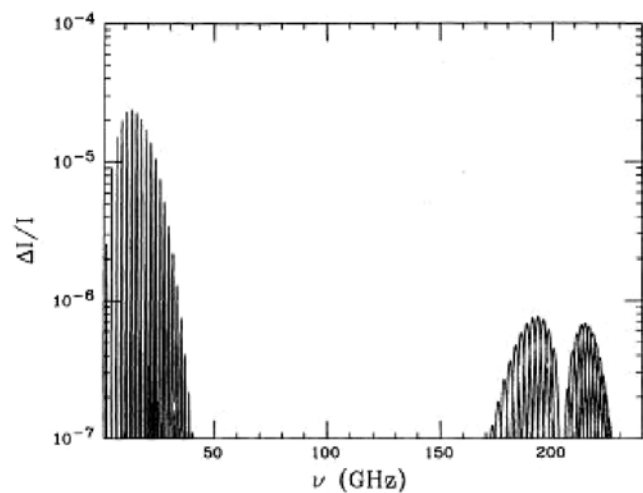


Fig. 9.2 Theoretical spectrum for a typical isolated cloud of galaxy cluster size at $z = 200$ moving at peculiar velocity. The abundance of LiH is close to $[\text{LiH}] = 3 \times 10^{-9}$ solar mass (curves from Maoli et al. [229])

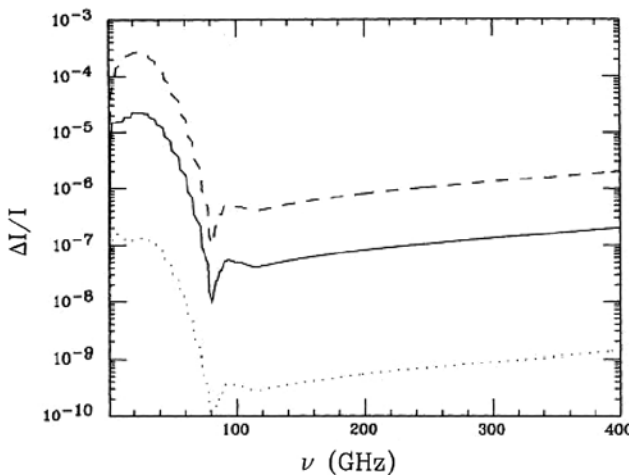


Fig. 9.3 Integrated theoretical spectrum (curves from Maoli et al. [229])

The search for primordial molecular lines may be one of the best tools to investigate the evolution of protostructure in the universe.

9.3 Observational situation

As said above, first searches for primordial resonant lines were carried out a few years ago using the 30 meter IRAM telescope at Pico Veleta (Spain) [244]. Observations were performed at three different frequencies: in the 1.3, 2, 3 mm atmospheric windows. They were characterized by a small band width and concerned only five spots in the sky. In this case, one obtained only upper limits for the abundance of the considered chemical species as a function of the redshift for a small interval in z and in a given direction.

A spectral line survey is performed using the ODIN satellite. This is a Swedish satellite developed in collaboration with France, Finland and Canada, equipped with a 1.1 meter telescope. Two sky regions—towards two of WMAP’s hot spots [191]—are observed in the two frequency ranges of 542–547 and 486–492 GHz, with a resolution of 1 mK over 10 MHz and with a particular strategy for detecting lines produced by nearly formed structures.

The future for primordial resonant lines will be the ESA’s HERSCHEL Space Observatory, which will allow one to observe a statistically representative area in the sky with a very large frequency range and a high sensitivity.

Primordial resonant lines are one of the main tools for exploring the pre-reionization and the post-reionization universe. The rich information associated with spectral lines can help to understand the formation and evolution of structures as well as the history of the metal enrichment of the high-redshift medium.

10 Past and future observations: COBE, WMAP, PLANCK

CMB is a cornerstone of modern cosmology. It is not surprising that the CMB provides us with a quantitative tool for studying the evolution of the universe. Because of atmospheric absorption, it was long ago realized that measurements of the high-frequency part of the CMB spectrum (wavelengths shorter than about 1 mm) should be performed from space. A satellite instrument also gives full sky coverage and a long observation time.

Observations by the NASA satellite the *Cosmic Background Explorer* (i.e. COBE) marked a turning point in CMB research both by establishing a definitive limit on spectral distortions through FIRAS measurements [119] and by discovering the temperature anisotropy through DMR measurements [12].

The NASA satellite the *Wilkinson Microwave Anisotropy Probe* (i.e. WMAP)—a descendant of the legendary COBE—has been mapping the temperature and polarization anisotropies of the CMB radiation. The PLANCK ESA’s satellite is currently scheduled for launch at the beginning of 2009. In the following, we give a brief overview of these three spatial missions together with some long-duration ballooning observations.

10.1 The Cosmic Background Explorer COBE

In November 1989, NASA launched the COBE satellite. During the duration of its flight, the three instruments on board COBE (FIRAS, DIRBE and DMR) were mapping the sky at wavelengths from 1 μm to 1 cm with the fundamental missions of

- making precise measurements of the spectrum and of the large scale anisotropy of the cosmic microwave background back in redshift to $z \sim 10^6$ or $t \sim 1$ year;
- detecting a possible cosmic infrared background (hereafter CIB) due to the cumulative emissions of objects formed since the decoupling of matter and radiation ($z \sim 10^3$ or $t \sim 10^4$ years), and
- studying the large-scale infrared and submillimeter emissions of the galaxy.

The Far Infrared Absolute Spectrophotometer (i.e. FIRAS)—with Mather as Principal Investigator—covered wavelengths in two ranges: from 0.1 to 0.5 mm and from 0.5 to 1 mm. The purpose of the FIRAS was to compare the spectrum of the CMB radiation with that of an exact black body and therefore to measure the small deviations from a Planckian spectrum. The CMB spectrum—Fig. 4.2—and the definitive limits on both the Compton parameter y and the chemical potential μ were given by FIRAS [119] as seen in Sect. 4.



Fig. 10.1 False-color image of the near-infrared sky as seen by the DIRBE. Data at 1.25, 2.2, and 3.5 μm wavelengths are represented respectively as blue, green and red colors. The image is presented in galactic coordinates, with the plane of the Milky Way galaxy horizontal across the middle and the galactic center at the center. The dominant sources of light at these wavelengths are stars within our galaxy. The image shows both the thin disk and central bulge populations of stars in our spiral galaxy. Our sun, much closer to us than any other star, lies in the disk (which is why the disk appears edge-on to us) at a distance

of about 28 000 light years from the center. The image is redder in directions where there is more dust between the stars absorbing starlight from distant stars. This absorption is so strong at visible wavelengths that the central part of the Milky Way cannot be seen. DIRBE data will facilitate studies of the content, energetics and large-scale structure of the galaxy, as well as the nature and distribution of dust within the solar system; figures from <http://cmbdata.gsfc.nasa.gov/product/cobe/dirbeimage.cfm>

The Diffuse Infrared Background Experiment (i.e. DIRBE)—with Hauser as Principal Investigator—spanned wavelengths from 1 to 300 μm in ten bands: J, K, L, M, the four IRAS bands (i.e. 12, 25, 60, 100 μm) and two large bands (100–200 μm and 200–300 μm). The cosmological objective of the DIRBE was to conduct a definitive search for CIB radiation. This purpose required extensive careful measuring and modeling of all the foreground emissions.

The DIRBE has mapped, in particular, the near-infrared sky: the false-color image of the near-infrared sky map is given in Fig. 10.1. The CIB had been first claimed by Puget et al. [248], using COBE data and was confirmed by several studies: those performed by Hauser et al. [249], Fixsen et al. [250], and Lagache et al. [251].

A set of Differential Microwave Radiometers (i.e. DMR)—with Smoot as Principal Investigator—operated at 3.3, 5.7 and 9.6 mm bands. The purpose of the DMR was to measure and map the large-scale anisotropy of the CMB radiation. The DMR results [12] are presented in Fig. 10.2, showing the near-uniformity of the CMB (top), the dipole (middle), and the multipole features of anisotropy (bottom).

Some cosmologists anticipated the 1992 COBE announcement. Almost at the same time that DMR measured these features, several observations were carried out

by some nineteen other ground-based or balloon-borne experiments. But let us note that these anisotropies were not observed until one reached the full sky coverage and long integration times that were provided by the COBE space mission.

The Wilkinson Microwave Anisotropy Probe (i.e. WMAP) mission was the second satellite—devoted to CMB by NASA—which followed the COBE. The PLANCK surveyor will be the third generation of space missions—for the CMB experiment—but conducted by ESA, the European Space Agency.

To conclude on COBE, let us mention that Mather and Smoot have jointly received the Nobel Prize in Physics for 2006.

10.2 The balloon observations of millimetric extragalactic radiation and geophysics BOOMERANG

Waiting for the two planned major satellite experiments WMAP in 2001 and PLANCK Surveyor in 2009—each with full sky and wide frequency coverage—several balloon-borne experiments were developed at the end of the nineties. These smaller experiments covered smaller sky areas with comparable sensitivity and similar observational strategy

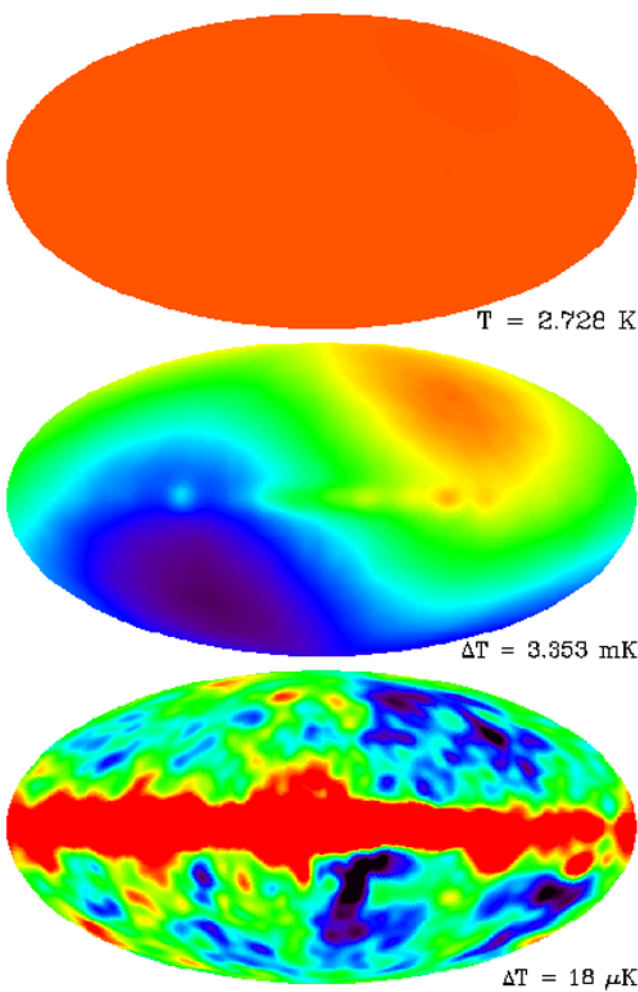
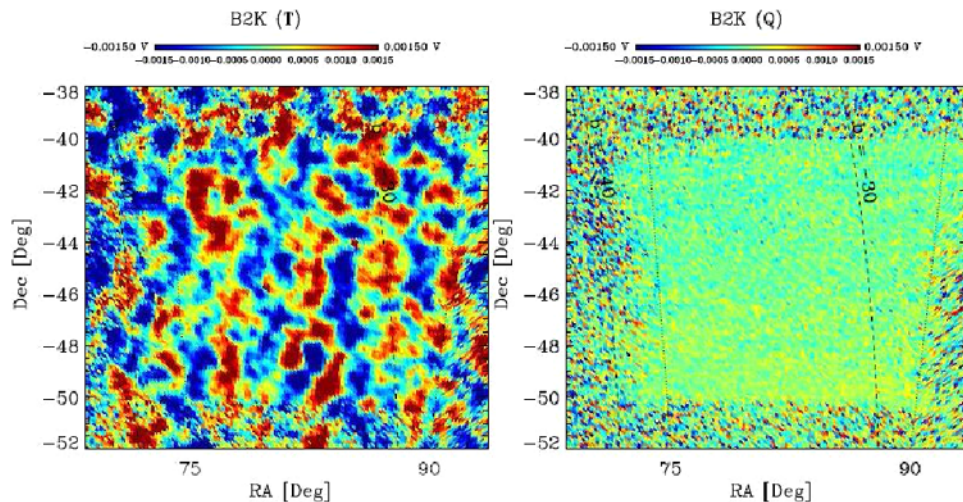


Fig. 10.2 The following image represents DMR data from the 53 GHz band (*top*) on a scale from 0–4 K, showing the near-uniformity of the CMB brightness (*middle*) on a scale intended to enhance the contrast due to the dipole described above, and (*bottom*) following subtraction of the dipole component; figures from <http://cmbdata.gsfc.nasa.gov/product/cobe/dmrimage.cfm>

Fig. 10.3 *Left:* preliminary CMB anisotropy map in the region with deeper integration surveyed during the B2K flight. *Right:* map of the Stokes parameter Q obtained from the 8 PSB bolometers; curves from de Bernardis et al. [253]



compared to the two satellite missions. They used also the critical technologies which were under development for WMAP and PLANCK.

Let us present the most famous one: BOOMERANG (hereafter used for Balloon Observations Of Millimetric Extragalactic Radiation and Geophysics). This microwave telescope, from an idea of Melchiorri and Richards, was developed by the teams of de Bernardis and Lange. This instrument was intended to measure the CMB anisotropies at angular scales between a few degrees and ten arcminutes. It featured a wide focal plane with 16 detectors in the frequency bands centered at 90, 150, 220 and 400 GHz with FWHM ranging between 18 and 10 arcminutes. BOOMERANG was launched on 29 December 1998 from Mc Murdo Station in Antarctica and was carried by a stratospheric balloon to an altitude of 38 km, where the low atmospheric pressure and low moisture content of the atmosphere facilitate such measurements.

The experiment collected data for 11 days without interruption, captured the first detection of the first peak due to acoustic oscillations localized at $l_{\text{peak}} = 197 \pm 6$ [207] and later provided the first high-resolution map of CMB anisotropies [252]. The teams upgraded the instrument and flew it again in 2003, this time detecting yet fainter patterns in the polarization of the CMB. Then, BOOMERANG provided the first high-resolution maps of CMB anisotropies. See, for instance, Fig. 10.3, for maps of CMB anisotropies and of the Stokes parameter, Q , as seen by the 2003 flight. Let us only remark that the color scaling of the Stokes parameter plot is identical to the temperature plot, emphasizing the tiny amplitude of the polarized signal.

In the previous section, we have seen that there is no doubt that we can see the acoustic wave projected on the sky. After the first release of the power spectra, for instance, Komatsu [260] asked *how the wave form in C_l determines the cosmological parameters*.

From the 2003 flight of BOOMERANG, they measured—not only the TT power spectrum [224]—but also the EE power spectrum [231]; moreover, they detected a significant TE correlation in the l -range between 50 and 950 [254]. It was the first measurement of the TE power spectrum using bolometer detectors.

Note that the TT and EE power spectra of the WMAP five-year data are compared with recent results of other experiments and in particular with the results [224, 231] obtained from the 2003 flight of BOOMERANG. Figures 8.1 and 8.5 show that now there exist many instruments devoted to CMB anisotropies and these moreover work with a great consistency between their various results. Before describing WMAP, let us mention that the Balzan Prize for 2006 was jointly awarded to de Bernardis and Lange.

10.3 The Wilkinson Microwave Anisotropy Probe WMAP

The WMAP satellite was launched in June 2001 from Cap Canaveral. It makes observations at the L2 Lagrangian point where the emission and magnetic field of the earth do not affect the satellite. The WMAP mission was designed to produce high-quality full-sky CMB maps, with the angular resolution a factor of 30 better than that of COBE, in five microwave bands: 22.8 GHz (or 13 mm), 33 GHz (or 9.1 mm), 40.7 GHz (or 7.3 mm), 60.8 GHz (or 4.9 mm), 93.5 GHz (or 3.2 mm).

WMAP released its first year results in February 2003. At that time, the mission was renamed the “Wilkinson Microwave Anisotropy Probe” to honor the late David Wilkinson who was a key “Investigator” of both COBE and WMAP missions until his death in September 2002.

On March 2008, WMAP released its five-year data set with new maps, power spectra and eight papers posted to LAMBDA; see <http://lambda.gsfc.nasa.gov>, [217, 230, 235, 255–258] and [259]). Figure 10.4 shows the five-year full-sky map of the CMB after foreground removal: colors repre-

sent the tiny temperature fluctuations of the *remnant glow* from the early universe.

From the only temperature TT power spectrum, in order to determine the parameters of a cosmological model, it is important to consider and to use all the features seen in Sect. 8.3—such as the locations, the heights of the peaks, etc.—which carry cosmological information.

- *Peak locations* lead to the distance to the last surface scattering which gives the 3D geometry, the age of the universe and the Hubble parameter altogether leading to the dark energy.
- *The first peak height* leads to the matter/radiation density ratio and to the dark-matter density.
- *The second peak height* leads to the baryon/radiation density ratio and therefore to the baryon density.

These parameters are primarily derived from the temperature data but the *fit* must include the polarization data which have a profound implication for cosmology.

- (i) For instance, on possible reionization: from the C_l^{TE} released in 2003, WMAP was supposed to detect a significant TE correlation at $l < 7$ which gave a measure of the optical depth against Thomson scattering of $\tau = 0.17 \pm 0.04$ [261].

A naive interpretation of the 2003 WMAP polarization and quasar data was that the universe has begun to reionize at $z_r \sim 20$ and became completely reionized [260] by $z \sim 6$. As we shall see later, the new 2008 WMAP data favor a smaller optical depth and therefore a different conclusion for the possible reionization of the universe. But, anyway, τ is a primary key parameter.

- (ii) On primordial fluctuations: the shape of the power spectrum of primordial curvature perturbations, $P_R(k)$, is one of the most powerful and practical tools for distinguishing among inflation models. In the Λ CDM

Fig. 10.4 Five-year WMAP

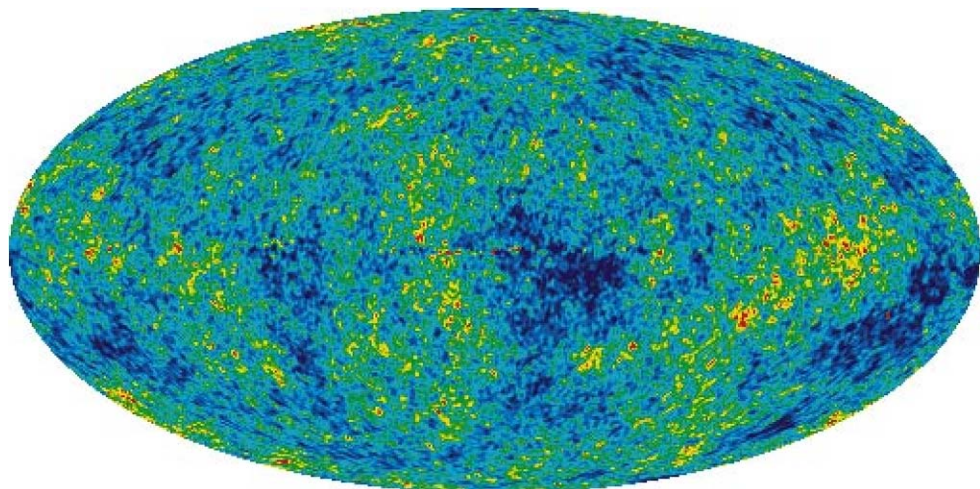


Table 10.1 Primary cosmological parameters of the Λ CDM model and their 68% intervals from WMAP five-year mean, adapted from [256]

$100 \Omega_b h^2$	2.273 ± 0.062	for the parameter of baryon energy-density parameter
$\Omega_d h^2$	0.1099 ± 0.0062	for the parameter of the dark-matter energy density
Ω_Λ	0.742 ± 0.030	for the cosmological parameter of energy density
n_s	0.963 ± 0.014	for the spectrum index
τ	0.087 ± 0.017	for the optical depth against Thomson scattering
$\Delta_R^2(k)$	$2.410.11 \times 10^{-9}$	for discriminating between inflation models

model, primordial scalar fluctuations are adiabatic and Gaussian, and they can be described by

$$\Delta_R^2(k) = \frac{k^3}{2\pi^2} P_R(k) \text{ proportional to } \left(\frac{k}{k_0}\right)^{n_s - 1}, \quad (10.1)$$

with $k_0 = 0.002 \text{ Mpc}^{-1}$. $\Delta_R^2(k_0)$ and n_s are also considered as *key parameters*.

Now, let us note that the *wave form* is more and more accurately measured. Figures 8.1 and 8.4 show respectively the temperature TT and temperature–polarization correlation TE power spectra based on the five-year WMAP data. The EE power spectrum and other BB, TB and EB spectra are carefully studied [235]; see Fig. 8.5 for the EE power spectrum. Finally, Table 10.1 gives a set of six parameters of the minimal Λ CDM model and the corresponding 68% uncertainties derived from the five-year WMAP data.

Let us note that not only *primary parameters* but also *derived parameters* [256] are given. All these parameters are deduced from the WMAP five-year data but also when these data are combined with other data on Type-Ia supernovae and on the distribution of the galaxies [256].

Komatsu et al. [256] have also explored the possible deviations from the simplest minimal Λ CDM model. These deviations appear as tests of inflation: flatness, adiabaticity and Gaussianity of the fluctuations, “scale invariance” of the power spectrum, and primordial gravitational waves. The WMAP team gives significant improvements on the limits on these deviations, while the satellite contributes to acquire more data. In conclusion, one can say that a lot of wonderful results can be found in the eight papers of the five-year WMAP data written by the members of its team.

Before describing the PLANCK mission, let us present parameters governing the sensitivity for both missions (see Table 10.2).

10.4 The future: the PLANCK satellite

10.4.1 On the satellite

PLANCK—see Fig. 10.6—is a mission of the European Space Agency designed to answer key cosmological ques-

Table 10.2 Parameters governing mission sensitivity from [263]. (a) NET/BLIP_{CMB} is the ratio of detector sensitivity to the fundamental CMB background limit at 100 GHz, (b) NET/1° × 1° is the statistical noise equivalent CMB temperature at 100 GHz, assuming the total integration time to be spread evenly over the sky

Mission	WMAP (100 GHz)	PLANCK (100 GHz)
Duration	8 years	1.2 years
Detector number	8	8
NET/BLIP _{CMB}	~60	~4
NET/1° × 1°	=6 μK	=1 μK

tions. It will be the first to map the entire sky with an unprecedented combination of sensitivity ($\Delta T/T \sim 2 \times 10^{-6}$), angular resolution (to 5') and frequency coverage (30–857 GHz). There are two instruments: the Low Frequency Instrument (i.e. LFI)—with HEMT arrays—covers the frequency range 30–70 GHz in three bands, and the High Frequency Instrument (i.e. HFI)—with bolometer arrays—covers the frequency range 100–857 GHz in six bands. Technical details of the PLANCK mission are given in *PLANCK: The Scientific Programme* [262]. Figure 10.5 shows the CMB spectrum and the nine frequency bands.

10.4.2 On the goals of PLANCK

Given that WMAP has already been extremely successful, it is natural to ask: what after WMAP?

Because WMAP can, crudely, measure less than 10% of the information contained in the CMB temperature anisotropies and only a tiny fraction of the information contained in the polarization anisotropies, PLANCK will do, *a priori*, a very good job. It can

- improve tests of inflationary models of the early universe,
- give accurate estimates of cosmological parameters and parameter degeneracies,
- give accurate estimates of the polarization power spectra,
- test non-Gaussianity,
- give significant new secondary science probes, in particular, as regards the Sunyaev–Zel'dovich effect,
- measure and identify foregrounds with astrophysics on these foregrounds.

Fig. 10.5 Spectra of sources in brightness temperature (in which a Rayleigh–Jeans ν^2 spectrum is flat), superimposed on the PLANCK frequency bands. Spectra of the galaxy and M82, a star-forming galaxy, are shown. For the galaxy, the components contributing to the over-all spectrum are identified. Also shown are the expected level of CMB fluctuations on a 1° scale, and, as a light dashed line (EG), the expected level of fluctuations introduced by all foreground radio sources on a $10'$ scale; curves from the PLANCK science programme documents, ESA-SCI (2005)

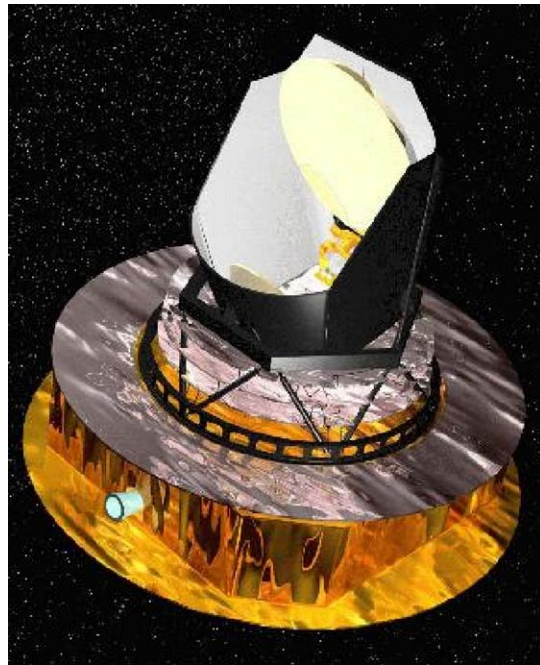
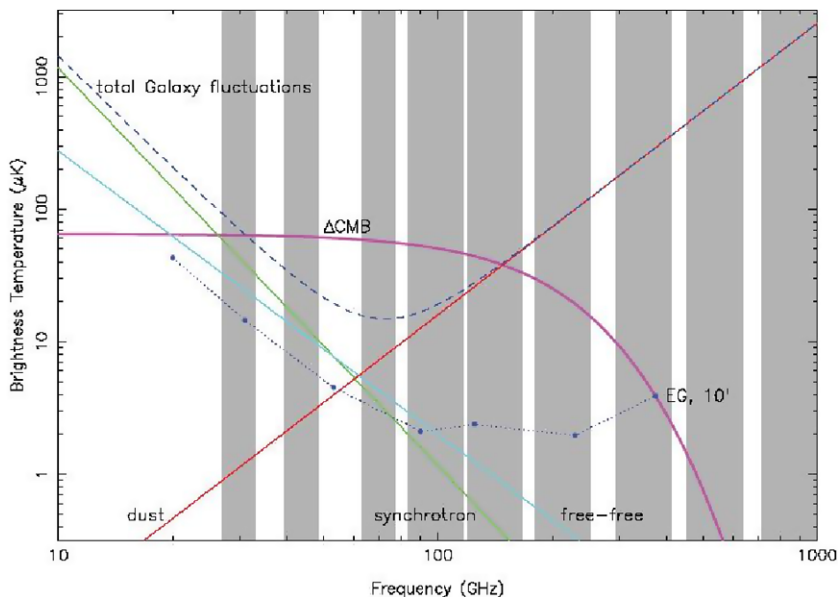


Fig. 10.6 PLANCK satellite, from the ESA web site www.esa.int

Concerning the effects of primordial chemistry on the CMB, Schleicher et al. [167] show that primordial chemistry does not alter the CMB at the significance level of the upcoming measurements by PLANCK. Nevertheless, the promising path to detect signals might be improved by the measurements of secondaries at small angular scales. These signals are related to the sizes of the primordial molecular clouds. This last information could be provided by the James Web Space Telescope (hereafter JWST) and the HERSCHEL telescope.



Fig. 10.7 HERSCHEL satellite, from the ESA web site www.esa.int

10.4.3 Conclusions

The scientific return from PLANCK will be spectacular. With a great increase in capabilities over previous CMB missions, we wait for completely new science.

10.5 The HERSCHEL and ODIN satellite

Observational prospects for HERSCHEL and ODIN have been discussed by Maoli et al. [264]. The molecular lines produced by resonant scattering of the CMB photons are

the most important signals coming from the dark age of the postrecombination universe. For these authors these signals associated with a linear evolution phase of perturbations are weaker and broader and their detection would be possible, as well as the primary anisotropy smearing, with millimetric multifrequency photometers under the condition of a very high sensitivity and a very precise characterization of foregrounds. This last requirement seems to be very challenging with the HERSCHEL satellite, see Fig. 10.7.

Let us notice that the relevance for PLANCK has recently been assessed by Dubrovich et al. [265].

11 Summary

One of the major discoveries in astrophysics was made in 1964: this was the first observation of the isotropic cosmic microwave background (CMB) radiation, by Penzias and Wilson, which has been of fundamental significance for our understanding of the development of the universe.

Since then, the FIRAS instrument, aboard the NASA satellite COBE, showed that the spectral distribution of the radiation is exactly that predicted for a black body at [119]: $T = 2.728 \pm 0.002$ K.

The DMR instrument, also aboard COBE, discovered temperature anisotropies, i.e. measured temperature fluctuations of about $\Delta T/T \sim 10^{-5}$. These can be interpreted as being due to a spatially varying gravitational potential at the time the CMB radiation was emitted. This happened at about $z \sim 1000$, which corresponds to some 300 000 years after the big bang.

Following COBE considerable progress has been made in higher-resolution measurements of the temperature anisotropy. With 45 times the sensitivity and 33 times the angular resolution of the COBE mission, WMAP was supposed to vastly extend our knowledge of cosmology: WMAP was supposed to measure the physics of the photon–baryon fluid at recombination and therefore to constrain models of structure formation, the geometry of the universe, and inflation.

After the release of the *One-year WMAP results*, the satellite is running extremely well with further improvements on anisotropy measurements. In particular, NASA, in 2008, presents the *Five-year WMAP observations*.

Meanwhile, HERSCHEL and PLANCK have been planned by ESA for a launch at the beginning of 2009. In these excellent perspectives, theoretical analyses of primordial molecules and CMB anisotropies with their profound implications on our knowledge of the physics of the early universe are actively studied in order to fully exploit the future results of HERSCHEL and PLANCK.

We should add that an important step for the big-bang theory was the discovery that light elements—hydrogen, helium-3, helium-4, lithium-7, deuterium—could be in relative abundances (once corrected for stellar nucleosynthesis)

as predicted by an early *hot phase*, the primordial nucleosynthesis. Therefore, this phase constituted, in a certain manner, the initial conditions for primordial chemistry.

The present status and prospects are as follows.

- Precise calculations give exact predictions for the fraction of each light element—D, ^3He , ^4He , ^7Li —that we should find from the early universe for any given value of η , where $\eta = \text{baryon number}/\text{photon number of photons}$. If the observed relic abundances of D and ^3He are in agreement with their predicted abundances, the observed relic abundances of ^4He and ^7Li pose a challenge to the SBBN (standard big-bang nucleosynthesis).
- The establishment of a Planck spectrum for the CMB radiation as well as its possible distortions are well studied. FIRAS aboard the NASA satellite COBE has shown that the CMB radiation is a pure black body and has given the 95% limits for the Compton distortion: $y < 1.5 \times 10^{-5}$ and for the chemical potential distortion: $\mu < 9 \times 10^{-5}$. These upper limits on any deviation of the CMB from a black-body spectrum place strong constraints on the energy transfer between the CMB and matter which can be expressed as functions of the redshift z .
- During the dark ages, the period between the recombination epoch and the first stars, molecules form from neutral and charged atomic species and open new channels of radiative exchange. The primordial chemistries of hydrogen, helium, deuterium and lithium allow us to investigate the first phase of structure formation in the universe.
- The CMB is very nearly isotropic, but a *dipole anisotropy* has been found a long time ago. In particular, the dipole anisotropy measured by the NASA satellite WMAP, $\Delta T = 3.346 \pm 0.017$ mK, shows that the solar system barycenter is moving at a velocity of 368 ± 2 km/s relative to the observable universe.
- For the first time, DMR aboard the NASA satellite COBE detected temperature anisotropies of the CMB: spatial variations of order $\Delta T/T \sim 10^{-5}$ across 10° – 90° on the sky. These 10^{-5} variations in temperature represent the direct imprint of initial gravitational potential perturbations on the CMB photons, called the Sachs–Wolf effect.
- On smaller angular scales ($\sim 1^\circ$), the general concept of CMB anisotropy uses a reasonable approximation known as the *tight-coupling* approximation: before the moment of recombination, the baryon–photon fluid existed as a single entity and after, the baryons and photons are completely decoupled fluids. Let us remember that in a spherical harmonic expansion of the CMB temperature field, the angular power spectrum specifies the contributions to the fluctuations coming from different multipoles, each corresponding to the angular scale $\theta = \pi/l$. The theory predicts that the temperature power spectrum has a series of peaks and troughs. Gravitational, baryonic, matter–radiation, dissipation effects on these acoustic phenomena are well understood and, as seen later, confirmed by observations.

- The main source of polarization from recombination is associated with the acoustic peaks in temperature. The EB harmonic description allows a direct confrontation between predictions and observations of the various angular power spectra.
- The BOOMERANG Team reported in 2000 the first images of structures in CMB anisotropies over a significant part of the sky and derived the temperature angular power spectrum of the CMB, $\langle TT \rangle$, from $l = 50$ to 600 with a first peak at multipole $l_{\text{pk}} = 197 \pm 6$ (1σ error).
- The NASA satellite WMAP, launched in 2001, has been mapping the temperature and polarization anisotropies of the CMB radiation on the full sky in five microwave bands: 22, 30, 41, 60, 94 GHz. The unprecedented quality of the WMAP data demands careful and rigorous analysis for deriving constraints. Note that the effect of undesired foreground emission—synchrotron, free-free and dust—from our galaxy and extragalactic sources are minimized by observing in five frequencies. In March 2008, the Team presented new full-sky maps based on data from the first five years of the WMAP sky survey. The team also presented the temperature and polarization angular power spectra of the CMB derived from these first five years of WMAP data. With greater integration time they, in particular, accurately measure the first few peaks in the TT power spectrum. More generally, the spectra are in excellent agreement with the best-fit, minimal, six-parameter Λ CDM model.
- The lines produced by resonant scattering of the CMB photons are among *the most important signals* coming from the dark ages of the postrecombination universe. The future for primordial resonant lines is clearly represented by the satellite HERSCHEL, which will allow us to observe a statistically representative area in the sky with a large band width and high sensitivity.

Measurements of the CMB anisotropy made in the last five years have clearly moved the cosmology model into an era of parameter determination till the inflationary epoch. As said above, a simple minimal Λ CDM model fits the five-year map WMAP data. However, as Komatsu recently notes: *Many popular inflation models have been either ruled out, or being in danger* (Talk given at the Chalonge school at the Observatoire de Paris, July 2008).

Moreover, the discussed results depend on the study of perturbations that are still in the linear, small-amplitude regime. We have also seen that problems will come with the confrontation with the non-linearities and difficulties associated with hydrodynamics and full chemistry.

On the other hand, many theoretical studies of primordial molecules are elaborated and we hope to observe them and the *echography* of the early universe. Finally, we also expect to answer the following question: when were the first objects formed?

We think that many of these mysteries will be cleared up by the release of data from the satellite PLANCK/HERSCHEL due to be launched in 2009.

In this review, we have mentioned some of the outstanding problems of modern cosmology: the origin of the fluctuations, the inflationary picture, the nature of dark energy, the nature of dark matter. Particle physics combined with astrophysics can lead to a better understanding of these problems and to a beginning of their solution: the very large—with the future space and ground-based telescopes—and the very small—with the Large Hadron Collider LHC and the International Linear Collider ILC—come together in the picture we have of the early universe.

Let us only emphasize that when we consider this view we are not only talking about the universe when it was a second or a nanosecond old; we are considering densities and temperatures which exceed anything that is experienced in the laboratories.

There is no other way of studying the conditions of the early universe. But there is a lot of new physics and astrophysics to be understood.

Acknowledgements We would like to dedicate our review to the memory of Professor Francesco Melchiorri—who died in July 2005—who was a key astrophysicist in the understanding of many research fields on the cosmic microwave background. He was a key person in our scientific lives.

M.S. is grateful to Professor Pierre Encrenaz, who made her feel very welcome at his Laboratoire of Observatoire de Paris and Ecole Normale Supérieure, for always supporting her research in cosmology and for initiating, in France, the search for primordial molecules at the IRAM 30 m telescope and later with the ODIN satellite. Finally, M.S. appreciates valuable discussions with Bianca Melchiorri, Françoise Combes and Jean-Michel Lamarre.

D.P. acknowledges the PNCG (Programme National de Cosmologie et Galaxies) and the PNPS (Programme National de Physique Stellaire) for their strong financial assistance, as well as Daniel Pfenniger, Viktor Dubrovich and Patrick Vonlanthen for their helpful advice.

The authors would like to thank Dieter Haidt for a very careful reading of the manuscript and fruitful suggestions.

References

1. A. Einstein, Ann. Phys. **17**, 891 (1905)
2. A. Einstein, Ann. Phys. **49**, 769 (1916)
3. A. Friedmann, Z. Phys. **10**, 377 (1922)
4. G. Lemaitre, Phys. Rev. **25**, 903 (1925)
5. W. De Sitter, Mon. Not. R. Astron. Soc. **78**, 3 (1917)
6. E. Hubble, Proc. Natl. Acad. Sci. **15**, 168 (1929)
7. A. Penzias, R. Wilson, Astrophys. J. **142**, 419 (1965)
8. M. White, D. Scott, J. Silk, Annu. Rev. Astron. Astrophys. **32**, 319 (1994)
9. R. Partridge, *3K: Cosmic Microwave Background Radiation* (Cambridge University Press, Cambridge, 1995)
10. W. Hu, S. Dodelson, Annu. Rev. A **40**, 171 (2002)
11. D. Puy, M. Signore, New Astron. Rev. **46**, 29 (2002)
12. G.F. Smoot et al., Astrophys. J. Lett. **396**, L1 (1992)
13. C. Bennett et al., Astrophys. J. Suppl. **148**, 1 (2003)
14. D. Spergel et al., Astrophys. J. Suppl. **170**, 377 (2007)

15. PLANCK Collaboration, ESA-SCI **1** (2005)
16. E. Kolb, M. Turner, *Gravitation and Cosmology* (Addison-Wesley, Reading, 1990)
17. P.J.E. Peebles, *Principles of Physical Cosmology* (Princeton University Press, Princeton, 1993)
18. J.A. Peacock, *Cosmological Physics* (Cambridge University Press, Cambridge, 1998)
19. F. Melchiorri, B. Olivo-Melchiorri, M. Signore, Riv. Nuovo Cimento **26**, 1 (2003)
20. A. Guth, Phys. Rev. D **23**, 347 (1981)
21. A.A. Starobinsky, Phys. Lett. B **91**, 99 (1980)
22. A.D. Linde, Phys. Lett. B **108**, 389 (1982)
23. A. Albrecht, P.J. Steinhard, Phys. Rev. Lett. **48**, 1220 (1982)
24. A.D. Linde, Phys. Lett. B **129**, 177 (1983)
25. J. Bock et al., [astro-ph/0604101](#)
26. P.J.E. Peebles, Astrophys. J. **153**, 1 (1968)
27. S. Seager, D. Sasselov, D. Scott, Astrophys. J. **128**, 407 (2000)
28. L. Bergstrom, A. Goobar, *Cosmology and Particles Astrophysics* (Springer, Berlin, 2004)
29. P. Peter, J.P. Uzan, *Cosmologie Primordiale* (Berlin, 2005)
30. P. de Bernardis et al., Astrophys. J. **564**, 559 (2002)
31. A. Benoit et al., Astron. Astrophys. **399**, L19 (2003)
32. D. Spergel et al., Astrophys. J. Suppl. **148**, 175 (2003)
33. L. Page et al., Astrophys. J. Suppl. **148**, 233 (2003)
34. S. Perlmutter et al., Nature **391**, 51 (1998)
35. B. Schmidt et al., Astrophys. J. **507**, 46 (1998)
36. S. Weinberg, *Gravitation and Cosmology: Principles and Applications of General Relativity* (Wiley, New York, 1972)
37. S. Weinberg, Rev. Mod. Phys. **61**, 1 (1989)
38. N. Straumann, Eur. J. Phys. **20**, 419 (1999)
39. S. Carroll, [astro-ph/0004075](#)
40. S. Weinberg, [astro-ph/0005265](#)
41. P. Salati, *The Cosmic Microwave Background*, ed. by C. Lineweaver et al. NATO-ASI Series C, vol. 502 (1997), p. 365
42. D.S. Akerib, S.M. Carroll, M. Kamionkowski, S. Ritz, *Summer Study on the Future of Particle Physics*, ed. by N. Graf (Snowmass, 2001), p. 409
43. E.W. Kolb, [hep-ph/9810362](#)
44. J. Ellis, Phys. Scr. T **85**, 221 (2000)
45. R. Wagoner, Astrophys. J. **179**, 343 (1973)
46. J. Yang, M. Turner, G. Steigman, D. Schramm, K. Olive, Astrophys. J. **281**, 493 (1984)
47. T. Walker, G. Steigman, D. Schramm, K. Olive, K. Kang, Astrophys. J. **376**, 51 (1991)
48. M. Smith, L. Kawano, R. Malaney, Astrophys. J. Suppl. **85**, 219 (1993)
49. S. Sarkar, Rep. Prog. Phys. **59**, 1493 (1996)
50. K. Olive, G. Steigman, T. Walker, Phys. Rep. **333**, 389 (2000)
51. S. Burles, K. Nollett, M. Turner, [astro-ph/9903300](#)
52. S. Burles, K. Nollett, M. Turner, Astrophys. J. **552**, L1 (2001)
53. B. Fields, S. Sarkar, Phys. Rev. D **66**, 010001 (2002)
54. H. Kurki-Suonio, Phys. Rev. D **37**, 2104 (1988)
55. R. Malaney, G. Mathews, Phys. Rep. **229**, 145 (1993)
56. K. Sumiyoshi, T. Kajino, C. Alcock, G. Mathews, Phys. Rev. D **42**, 3963 (1990)
57. G. Fuller, K. Jedamzik, G. Mathews, Phys. Lett. B **333**, 135 (1994)
58. A. Heckler, Phys. Rev. D **51**, 405 (1995)
59. K. Kainulainen, H. Kurki-Suonio, Sihvola, Phys. Rev. D **59**, 083585 (1999)
60. J. Lara, T. Kajino, G. Mathews, Phys. Rev. D **73**, 083501 (2006)
61. L. Kavano, [fermilab-Pub-92/04](#)
62. L. Kavano, <http://www-thphys.physics.ox.ac.uk/user/SubirSarkar/bbn.html>
63. K. Nollet, S. Burles, Phys. Rev. D **61**, 123505 (2000)
64. G. Steigman, Int. J. Mod. Phys. E **15**, 1 (2006)
65. D. Kirkman et al., Astrophys. J. Suppl. **149**, 1 (2003)
66. D. Spergel et al., Astrophys. J. Suppl. **170**, 377 (2007)
67. G. Steigman, Annu. Rev. Nucl. Part. Sci. **57**, 463 (2007)
68. Y.I. Izotov et al., Astrophys. J. Suppl. **108**, 1 (1997)
69. Y.I. Izotov et al., Astrophys. J. **500**, 188 (1998)
70. K. Olive, G. Steigman, Astrophys. J. Suppl. **97**, 49 (1995)
71. K. Olive et al., Astrophys. J. **483**, 788 (1997)
72. B. Fields, K. Olive, Astrophys. J. **506**, 177 (1998)
73. Y.I. Izotov, T.X. Thuan, Astrophys. J. **602**, 200 (2004)
74. K. Olive, E. Skillman, Astrophys. J. **617**, 29 (2004)
75. R. Gruenwald et al., Astrophys. J. **567**, 931 (2002)
76. M. Fukugita, M. Kawasaki, Astrophys. J. **646**, 1 (2006)
77. M. Peimbert et al., Astrophys. J. **666**, 636 (2007)
78. F. Spite, M. Spite, Astron. Astrophys. **115**, 357 (1982)
79. S.G. Ryan et al., Astrophys. J. **523**, 654 (1999)
80. S. Ryan et al., Astrophys. J. **530**, L57 (2000)
81. P. Bonifacio et al., Mon. Not. R. Astron. Soc. **292**, L1 (1997)
82. P. Bonifacio, P. Molnar, Mon. Not. R. Astron. Soc. **285**, 847 (1997)
83. T. Bania et al., Nature **415**, 54 (2002)
84. M. Tegmark et al., Phys. Rev. D **74**, 123507 (2006)
85. J.P. Kneller, G. Steigman, New J. Phys. **6**, 117 (2004)
86. G. Gamov, Phys. Rev. **70**, 572 (1946)
87. G. Gamov, Nature **162**, 680 (1948)
88. R.A. Alpher, R.C. Herman, Nature **162**, 774 (1948)
89. R.H. Dicke, P.J.E. Peebles, P.J. Roll, D.T. Wilkinson, Astrophys. J. **142**, 414 (1965)
90. R. Mandolesi, N. Vittorio, *The Cosmic Microwave Background: 25 Years Later* (Kluwer Academic, Dordrecht, 1990), p. 164
91. S.S. Holt, C.L. Bennett, V. Trimble, *After the First Three Minutes*. AIP Conference Proceedings, vol. 222 (1991)
92. M. Signore, C. Dupraz, *The Infrared and Submillimeter Sky after COBE*, NATO-ASI 502, 1992
93. B. Melchiorri, F. Melchiorri, Riv. Nuovo Cimento **17**, 1 (1994)
94. J.L. Sanz, E. Martinez-Gonzalez, L. Cayon, *Present and Future of the Cosmic Microwave Background*. Lecture Notes in Physics, vol. 429 (Springer, Berlin, 1994)
95. R.B. Partridge, *3K: The Cosmic Microwave Background Radiation* (Cambridge University Press, Cambridge, 1995)
96. C.H. Lineweaver et al., *The Cosmic Microwave Background*, NATO-ASI 502, 1997
97. M. Signore, F. Melchiorri, *Topological Defects in Cosmology* (World Scientific, Singapore, 1998)
98. L. Maiani, F. Melchiorri, N. Vittorio, *3K Cosmology*. AIP Conference Proceedings, vol. 476 (1999)
99. F. Melchiorri, G. Sironi, M. Signore, New Astron. Rev. **43**(1999)
100. J. Bartlett, New Astron. Rev. **45**, 283 (2001)
101. M. Signore, A. Blanchard, New Astron. Rev. **45** (2001)
102. A. Blanchard, M. Signore, *Frontiers of Cosmology*. NATO-ASI, vol. 187 (2005)
103. F. Melchiorri, Y. Rephaeli, *Background Microwave Radiation* (Scuola Enrico Fermi, Societ Italiana di Fisica, 2005)
104. G. Gamov, Phys. Today **3**, 16 (1950)
105. G. Gamov, K. Danske, Vidensk. Seks. Mat.-Phys. Medd. **7**, 1 (1953)
106. G. Gamov, in *Astronomy*, ed. by A. Beers (Pergamon, New York, 1956)
107. R.A. Alpher, R.C. Herman, Phys. Rev. **75**, 1089 (1949)
108. R.A. Alpher, R.C. Herman, Rev. Mod. Phys. **22**, 153 (1950)
109. R.A. Alpher, R.C. Herman, Phys. Rev. **84**, 60 (1951)
110. R.A. Alpher, R.C. Herman, *Modern Cosmology in Retrospect*, ed. by B. Bertotti et al. (1990), p. 129
111. W.S. Adams, Astrophys. J. **93**, 11 (1941)
112. A. McKellar, Publ. Dom. Astrophys. Obs. **1**, 251 (1941)
113. G. Herzberg, *Diatomeric Molecules* (Van Nostrand-Reinhold, New York, 1950)

114. P. Thaddeus, Annu. Rev. Astron. Astrophys. **10**, 305 (1972)
115. M.E. Kaiser, E.L. Wright, Astrophys. J. Lett. **356**, L1 (1990)
116. K.C. Roth, D.M. Meyer, I. Hawkins, Astrophys. J. Lett. **413**, L67 (1993)
117. G. Dall’Oglio et al., Phys. Rev. **13**, 1187 (1976)
118. G.F. Smoot, *The Cosmic Microwave Background*, ed. by C.H. Lineweaver et al. NATO ASI, vol. 502 (1997), p. 271
119. D.J. Fixsen et al., Astrophys. J. **473**, 576 (1996)
120. J.C. Mather et al., Astrophys. J. **420**, 440 (1994)
121. M.A. Janssen, *The Infrared and Submillimeter Sky after COBE*, ed. by M. Signore, C. Dupraz. NATO ASI, vol. 359 (1992), p. 391
122. R.A. Sunyaev, Y.B. Zel’dovich, Annu. Rev. Astron. Astrophys. **18**, 537 (1980)
123. L. Danese, G. De Zotti, Rev. Nuovo Cimento **7**, 277 (1977)
124. P. Salati, *The Infrared and Submillimeter Sky after COBE*, ed. by M. Signore, C. Dupraz. NATO ASI, vol. 359 (1992), p. 143
125. J. Ellis et al., Nucl. Phys. B **373**, 399 (1992)
126. M. Tegmark, J. Silk, A. Blanchard, Astrophys. J. **420**, 484 (1994)
127. A. Kogut et al., Astrophys. J. **419**, 1 (1993)
128. J.P. Ostriker, C. Thompson, Astrophys. J. **323**, L97 (1987)
129. J.J. Levin, K. Freese, D.N. Spergel, Astrophys. J. **389**, 44 (1992)
130. L. Danese, G. De Zotti, Astron. Astrophys. **84**, 364 (1980)
131. L. Danese, G. De Zotti, Astron. Astrophys. **107**, 39 (1982)
132. A.S. Kompaneets, Sov. Phys. JETP **4**, 730 (1957)
133. C. Burigana, L. Danese, G. De Zotti, Astron. Astrophys. **246**, 49 (1991)
134. C. Burigana, G. De Zotti, L. Danese, Astrophys. J. **379**, 1 (1991)
135. L. Danese, C. Burigana, in *Present and Future of the CMB*, ed. by J.L. Sanz et al. Lecture Notes in Physics, vol. 429 (Springer, Berlin, 1994), p. 28
136. A.P. Lightman, Astrophys. J. **244**, 392 (1981)
137. W. Hu, J. Silk, Phys. Rev. D **48**, 485 (1993)
138. P.J.E. Peebles, Astrophys. J. **153**, 1 (1968)
139. P.J.E. Peebles, R. Dicke, Astrophys. J. **154**, 891 (1968)
140. R. Weymann, Phys. Fluids **8**, 2112 (1965)
141. R. Weymann, Astrophys. J. **145**, 560 (1966)
142. I. Bernshtein, D. Bernshtein, V. Dubrovich, Astron. Z. **54**, 727 (1977)
143. V. Dubrovich, V. Stolyarov, Astron. Lett. **23**, 565 (1997)
144. V. Dubrovich, S.I. Grachev, Astrofizika **34**, 249 (1991)
145. S. Lepp, M. Shull, Astrophys. J. **280**, 465 (1984)
146. W. Latter, J. Black, Astrophys. J. **372**, 161 (1991)
147. D. Puy, G. Alecian, J. Le Bourlot, J. Léorat, G. Pineau des Forets, Astron. Astrophys. **267**, 337 (1993)
148. D. Galli, F. Palla, Astron. Astrophys. **335**, 403 (1998)
149. P. Stancil, S. Lepp, A. Dalgarno, Astrophys. J. **509**, 1 (1998)
150. S. Lepp, P. Stancil, A. Dalgarno, J. Phys. B **35**, R57 (2002)
151. D. Pfenniger, D. Puy, Astron. Astrophys. **398**, 447 (2003)
152. D. Puy, D. Pfenniger, Astron. Astrophys. (2008 submitted)
153. W. Roberge, A. Dalgarno, Astrophys. J. **255**, 489 (1982)
154. W. Saslaw, D. Zipoy, Nature **201**, 767 (1967)
155. Y. Shchekinov, M. Entél, Sov. Astron. **27**(6), 622 (1983)
156. R. Bienek, A. Dalgarno, Astrophys. J. **228**, 635 (1979)
157. T. Oka, Phys. Rev. Lett. **45**, 531 (1980)
158. J. Tennyson, Rep. Prog. Phys. **57**, 421 (1995)
159. E. Herbst, Philos. Trans. R. Soc. Lond. A **358**, 2523 (2000)
160. E. Bougleux, D. Galli, Mon. Not. R. Astron. Soc. **288**, 638 (1997)
161. P. Stancil, S. Lepp, A. Dalgarno, Astrophys. J. **458**, 401 (1996)
162. F. Gianturco, P. Gori Giorgi, Phys. Rev. A **54**, 4073 (1996)
163. F. Gianturco, P. Gori Giorgi, Astrophys. J. **479**, 560 (1997)
164. A. Dickinson, F. Gadéa, Mon. Not. R. Astron. Soc. **318**, 2000 (1227)
165. D. Galli, F. Palla, [astro-ph/0202329](#)
166. T. Abel, P. Anninos, Y. Zhang, M. Norman, New Astron. **2**, 181 (1997)
167. D. Schleicher, D. Galli, F. Palla, M. Camenzind, R. Kleseen, M. Bartelmann, S. Glover, [astro-ph/08033987](#)
168. F. Hasenöhrl, Ann. Phys. **15**, 344 (1904)
169. F. Hasenöhrl, Ann. Phys. **16**, 589 (1905)
170. K. Mosengheil, Ann. Phys. **22**, 867 (1907)
171. B. Melchiorri, F. Melchiorri, M. Signore, New Astron. Rev. **46**, 603 (2002)
172. B. Partridge, D.T. Wilkinson, Phys. Rev. Lett. **18**, 557 (1967)
173. D. Sciama, Phys. Rev. Lett. **18**, 1065 (1967)
174. M. Rees, D. Sciama, Nature **213**, 374 (1967)
175. J.M. Stewart, D.W. Sciama, Nature **216**, 748 (1967)
176. C.V. Heer, R.H. Kohl, Phys. Rev. **174**, 1611 (1968)
177. P.J.E. Peebles, Wilkinson, Phys. Rev. **174**, 2168 (1971)
178. M. Forman, Planet Space Sci. **18**, 25 (1970)
179. J.A. Peacock, *Cosmological Physics* (Cambridge University Press, Cambridge, 1998)
180. E.K. Conklin, R.N. Bracewell, Nature **216**, 777 (1967)
181. R.N. Bracewell, E.K. Conklin, Nature **219**, 1343 (1968)
182. E.K. Conklin, R.N. Bracewell, Nature **222**, 971 (1969)
183. E.K. Conklin, IAU Symp. **44**, 518 (1972)
184. P.S. Henry, Nature **231**, 516 (1971)
185. B.E. Corey, D.T. Wilkinson, Bull. Am. Astron. Soc. **8**, 351 (1976)
186. G.F. Smoot, M.V. Gorenstein, R.A. Muller, Phys. Rev. Lett. **39**, 898 (1977)
187. R. Fabbri, J. Guidi, F. Melchiorri, V. Natale, Phys. Rev. Lett. **44**, 1563 (1980)
188. S.P. Boughn et al., Astrophys. J. **243**, L113 (1981)
189. P.M. Lubin et al., Astrophys. J. **298**, L1 (1985)
190. C.L. Bennet et al., Astrophys. J. **464**, L1 (1996)
191. C.L. Bennet et al., Astrophys. J. Suppl. **148**, 1 (2003)
192. T. Pamanabhan, *Theoretical Astrophysics III* (Cambridge University Press, Cambridge, 2002)
193. E. Branchini, M. Plionis, D.W. Sciama, Astrophys. J. **461**, L17 (1996)
194. A. Dekel, *Cosmic Flows 1999*, ed. by S. Courteau et al. ASP Conf. Ser., vol. 420 (2000)
195. J.C. Mather et al., Astrophys. J. **354**, 37 (1990)
196. R.K. Sachs, A.M. Wolf, Astrophys. J. **147**, L1 (1967)
197. F. Melchiorri et al., Astrophys. J. **250**, 1 (1981)
198. R.D. Davies, A.N. Lasenby, R.A. Watson, Nature **236**, 462 (1987)
199. P.M. Lubin, G.L. Epstein, G.F. Smoot, Phys. Rev. Lett. **50**, 616 (1983)
200. D.J. Fixsen, E.S. Cheng, D.T. Wilkinson, Phys. Lett. **50**, 620 (1983)
201. P.J.E. Peebles, J.T. Yu, Astrophys. J. **162**, 815 (1970)
202. A.G. Doroshkevich, Y.B. Zel’dovich, R.A. Sunyaev, Sov. Astron. **22**, 523 (1978)
203. J.R. Bond, G. Efstathiou, Astrophys. J. **285**, L45 (1984)
204. U. Seljak, Astrophys. J. **435**, 87 (1994)
205. W. Hu, M. White, Astrophys. J. **471**, 30 (1996)
206. W. Hu, N. Sugiyama, J. Silk, Nature **386**, 37 (1997)
207. P. de Bernardis et al., Nature **404**, 955 (2000)
208. S. Hanany et al., Astrophys. J. Lett. **545**, L5 (2000)
209. J.R. Bond, in *Cosmology and Large Scale Structure*, ed. by R. Schaeffer, J. Silk, M.J. Spiro, J. Zinn-Justin (Elsevier Science, Amsterdam, 1996), p. 469
210. M. Kamionkowski, A. Kosowsky, Annu. Rev. Nucl. Part. Sci. **49**, 77 (1999)
211. W. Hu, S. Dodelson, Annu. Rev. Astron. Astrophys. **40**, 171 (2002)
212. N. Kaiser, Mon. Not. R. Astron. Soc. **202**, 1169 (1983)
213. W. Hu, Ann. Phys. **303**, 203 (2003)
214. W. Hu, [astro-ph/08023688](#)
215. C. Reichardt et al., [astro-ph/08011491](#)

216. C. Bischoff et al., [astro-ph/08020888](#)
217. G. Hinshaw et al., [astro-ph/08030722](#)
218. J.M. Bardeen, Phys. Rev. D **22**, 1882 (1980)
219. G. Efstathiou, *Physics of the Early Universe*. Proceedings of the Scottish Universities Summer School in Physics, vol. 36, p. 361
220. V.F. Mukhanov, H.A. Feldmann, R.H. Brandenberger, Phys. Rep. **215**, 203 (1992)
221. W. Hu, Sugiyama, Astrophys. J. **1444**, 489 (1995)
222. W. Hu, Sugiyama, Astrophys. J. **1471**, 542 (1996)
223. J. Silk, Sugiyama, Astrophys. J. **1151**, 459 (1968)
224. W.C. Jones et al., Astrophys. J. **647**, 823 (2006)
225. A.C.S. Readhead et al., Astrophys. J. **609**, 498 (2006)
226. M. Rees, D. Sciama, Nature **217**, 511 (1968)
227. U. Seljak, Astrophys. J. **463**, 1 (1996)
228. R. Sunyaev, Y. Zel'dovich, Comments Astrophys. Space Phys. **4**, 173 (1972)
229. R. Maoli, F. Melchiorri, D. Tosti, Astrophys. J. **425**, 372 (1994)
230. J. Dunkley et al., [astro-ph/08030586](#)
231. T.E. Montroy et al., Astrophys. J. **647**, 813 (2006)
232. J.L. Sievers et al., Astrophys. J. **660**, 976 (2007)
233. P. Ade et al., Astrophys. J. **674**, 22 (2008)
234. E. Leitch et al., Astrophys. J. **624**, 10 (2005)
235. M.R. Nolta et al., [astro-ph/08030593](#)
236. V.K. Dubrovich, Pis'ma Astron. Z. **1**, 10 (1975)
237. J.A. Rubiño-Martin, J. Chluba, R.A. Sunyaev, Astron. Astrophys. **371**, 1939 (2006)
238. J.A. Rubiño-Martin, J. Chluba, R.A. Sunyaev, [astro-ph/07110594](#)
239. W.Y. Wong, D. Scott, Mon. Not. R. Astron. Soc. **375**, 1441 (2007)
240. V.K. Dubrovich, Sov. Astron. Lett. **3**, 128 (1977)
241. V.K. Dubrovich, Astron. Astrophys. Trans. **5**, 57 (1994)
242. M. Mayer, W.J. Duschl, Mon. Not. R. Astron. Soc. **358**, 614 (2005)
243. R. Maoli et al., Astrophys. J. **457**, 1 (1996)
244. P. de Bernardis et al., Astron. Astrophys. **269**, 1 (1993)
245. B. Melchiorri, F. Melchiorri, Riv. Nuovo Cimento **17**, 1 (1994)
246. M. Signore et al., Astrophys. J. Suppl. **92**, 535 (1994)
247. D. Puy, M. Signore, New Astron. Rev. **51**, 411 (2007)
248. J.L. Puget, A. Abergel, J.P. Bernard, Astron. Astrophys. **308**, L5 (1996)
249. M.G. Hauser et al., Astrophys. J. **508**, 25 (1998)
250. D.J. Fixsen et al., Astrophys. J. **508**, 123 (1998)
251. G. Lagache et al., Astron. Astrophys. **344**, 322 (1999)
252. P. de Bernardis et al., Astrophys. J. **564**, 559 (2002)
253. P. de Bernardis et al., [astro-ph/0311396](#)
254. F. Piacentini et al., Astrophys. J. **647**, 833 (2006)
255. R. Hill et al., [astro-ph/08030570](#)
256. E. Komatsu et al., [astro-ph/08030547](#)
257. M. Limon et al., Astrophys. J. Suppl. (2008 submitted)
258. B. Gold et al., [astro-ph/08030715](#)
259. E. Wright et al., [astro-ph/08030577](#)
260. E. Komatsu et al., *Background Microwave Radiation and Intra Cluster Cosmology*, ed. by F. Melchiorri, Y. Rephaeli. Course CLIX, Varenna, SIF (2005), p. 37
261. A. Kogut et al., Astrophys. J. Suppl. **148**, 161 (2003)
262. The Scientific Programme of PLANCK, ESA-SCI I, 2005. [astro-ph/0604069](#),
263. J. Bock et al., [astro-ph/0604101](#)
264. R. Maoli et al., [astro-ph/0411641](#)
265. V.K. Dubrovich, *Exploring the Cosmic Frontier*. ESO Symposia (Springer, Berlin, 2007)